Indo-Pacific Sea Surface Temperature modes and their Impacts on East Asian Climate in the Climate Model Environment

LEE WAI KI

DOCTOR OF PHILOSOPHY

CITY UNIVERSITY OF HONG KONG

April 2017

CITY UNIVERSITY OF HONG KONG

香港城市大學

Indo-Pacific Sea Surface Temperature modes and their Impacts on East Asian Climate in the Climate Model Environment

印太海溫狀態與其對東亞氣候在氣候模式下的影響

Submitted to

School of Energy and Environment

能源及環境學院

In Partial Fulfillment of the Requirements

for the Degree of Doctor of Philosophy

哲學博士學位

By

Lee Wai Ki

李偉淇

April 2017

二零一七年四月

Contents

Abstract i

Qualifying Panel and Examination Panel iii

List of Acronyms iv

List of Figures vi

List of Table ix

Acknowledgments x

1. Introduction……...1
2. Description of Datasets…….....4
    2.1. Reanalysis data……..4
    2.2. Coupled model hindcast data……..……..5
    2.3. General data arrangement and some typical equations……..……...9
3. The Two Flavors of ENSO and their Seasonal Predictions' Skills in Coupled Models….....10
    3.1. Introduction…….....11
        3.1.1. A review of the two flavors of ENSO and their behaviors in GCMs.....11
        3.1.2. The focus of the present Chapter…….....12
    3.2. Basic climate state in the CGCMs…….……..13
    3.3. ENSO patterns, evolution and amplitude…….……...24
    3.4. ENSO skills in CGCMs……...42
    3.5. Mixings of El Niño in CGCMs……44
    3.6. Evolution and persistence of ENSO……48
    3.7. Summary of Chapter 3…….54
4. Impacts of the Two Flavors of ENSO on East Asian Climate and their Behaviors in CGCMs..56
    4.1. Introduction…….....57
        4.1.1. Observed and predicted impacts of ENSO on East Asian climate…….57
        4.1.2. Asian summer monsoon and the Philippines Sea Anticyclone……..57
        4.1.3. The focus of the present study……58

4.2. Impacts of ENSO on EA climate and their characteristic in coupled model environment……...59
4.3. The relationship between ENSO and East Asian monsoon state……....66
4.4. Summary of Chapter 4……....70
5. Indian Ocean SST Modes, Associated Climate Impacts and their Relationship to ENSO…....72
5.1. Introduction…….....73
5.1.1. A review of the modes of Indian Ocean SST…….....73
5.1.2. Modeling studies on IO SST modes and the their relationship to ENSO..73
5.1.3. The focus of the present chapter……74
5.2. Different modes of Indian Ocean SST and their behaviors in CGCMs……..75
6. Discussion and Summary…….....80

Bibliography……...83

Abstract

This study investigates the predictability of the two flavors of El Niño Southern Oscillation (ENSO) and their impacts on the East Asian (EA) Climate during the decaying phase (boreal spring and summer) using the Asia-Pacific Climate Center (APCC) Coupled Global Circulation Models (CGCMs).

For the predictability of ENSO, it is found that the models generally predict the persistence and spatial pattern of the canonical ENSO better than ENSO Modoki. The models always decay ENSO quicker than the observations, and the decay is more rapid for ENSO Modoki. Also, the projection coefficient and the degree of mixings method are carried out to access the ability of the models to differentiate the two ENSO flavors. The results show that the models with low degree of mixings tend to give good differentiation between the two ENSO flavors.

For the impacts of ENSO on the East Asian climate, it is found that, for the canonical ENSO, the location of the low level anti-cyclone plays an important role of the anomalous rainfall over the East Asia. The models generally give good predictions to the East Asian rainfall during the decaying boreal spring. It is also found that both predictions of canonical ENSO SST and the mean circulation over the East Asia affect the predictions of the El Niño precipitation over EA during the decaying summer of El Niño. However, for the decaying summer of ENSO Modoki, the predictions of ENSO Modoki SST seem not important, while the predictions of the mean circulation over EA are still crucial to the predictions of the Modoki rainfall over the EA.

For the Indian Ocean Empirical Orthogonal Function (EOF) analysis, it is found that the Indian Ocean Basin Mode (IOBM) has great lag relationship to the canonical ENSO, while the new discovered EOF4 of the Indian Ocean SSTA has some degree of relationship to the ENSO Modoki. The Subtropical Indian Ocean Dipole (SIOD) seems not to have too much relationship with the two flavors of ENSO.

CITY UNIVERSITY OF HONG KONG

Qualifying Panel and Examination Panel

Surname: LEE

First Name: Wai Ki

Degree: PhD

College/Department: School of Energy and Environment

The Qualifying Panel of the above student is composed of:

Supervisor(s)

Dr. NGAN Keith	School of Energy and Environment City University of Hong Kong

Qualifying Panel Member(s)

Dr. ZHOU Wen	School of Energy and Environment City University of Hong Kong
Prof. CHAN Chung Leung Johnny	School of Energy and Environment City University of Hong Kong

This thesis has been examined and approved by the following examiners:

Dr. ZHOU Wen	School of Energy and Environment City University of Hong Kong
Dr. NGAN Keith	School of Energy and Environment City University of Hong Kong
Prof. STRAUB	Department of Atmospheric and Oceanic Sciences McGill University
David Prof. WU Zhiwei	College of Atmospheric Science Nanjing University of Information Science & Tech

List of Acronyms

AGCM	Atmospheric Global Circulation Model
APCC	Asia-Pacific Climate Center
CGCM	Coupled Global Circulation Model
CP El Niño	Central Pacific Type El Niño/El Niño Modoki
DMI	Dipole Mode Index
EA	East Asia/ East Asian
EASM	East Asian Summer Monsoon
EMI	El Niño Modoki Index
ENSO	El Niño Southern Oscillation
EOF	Empirical Orthogonal Function
EP El Niño	Eastern Pacific Type El Niño/Canonical El Niño
GCM	Global Circulation Model
IO	Indian Ocean
IOB	Indian Ocean Basin
IOD	Indian Ocean Dipole
ISM	Indian Summer Monsoon

MME	Multi-Model Ensemble
MME-EW	Multi-Model Ensemble (Equally Weighting)
MME-SVD	Multi-Model Ensemble (Weighted by Singular Variable Decomposition)
NCEP	National Centers for Environmental Prediction
NOA	North Atlantic Oscillation
OGCM	Oceanic Global Circulation Model
PC	Principle Component
PjC	Projection Coefficient
PSA	Philippines Sea Anti-cyclone
SC	South China
SCS	South China Sea
SIOD	Subtropical Indian Ocean Dipole
SST	Sea Surface Temperature
SSTA	Sea Surface Temperature Anomaly
TIO	Tropical Indian Ocean

List of Figures

Fig. 2.1 Schematic representation of forecast dates of APCC models ..... - 7 -
Fig. 3.1 Seasonal mean SST over Tropical Pacific region [20°S-20°N; 120°E-70°W] during SON season ..... - 16 -
Fig. 3.2 The same as Fig3.1, except for DJF season ..... - 18 -
Fig. 3.3 The same as Fig3.1, except for MAM season ..... - 19 -
Fig. 3.4 The same as Fig3.1, except for JJA season ..... - 20 -
Fig. 3.5 SST standard deviation over Tropical Pacific region [20°S-20°N; 120°E-70°W] during SON season ..... - 22 -
Fig. 3.6 The same as Fig3.1, except for JJA season ..... - 23 -
Fig. 3.7 The same as Fig3.1, except for MAM season ..... - 24 -
Fig. 3.8 The same as Fig3.1, except for JJA season ..... - 25 -
Fig. 3.9 The 1st EOF patterns of SSTA over the Tropical Pacific region [20°S-20°N; 120°E-70°W]. Fractional variance explained by each EOF pattern is given at top right of each panel ..... - 27 -
Fig. 3.10 Normalized Nino3 index (solid) and the PC1 of Tropical Pacific [20S-20N; 120E-70W] SSTA (dotted) ..... - 28 -
Fig. 3.11 The same as Fig.3.1, except for the 2nd EOF of the tropical Pacific SSTA. ..... - 30 -
Fig. 3.12 Normalized EMI (solid) and the PC2 of Tropical Pacific [20S-20N; 120E-70W] SSTA (dotted) ..... - 31 -
Fig. 3.13 The canonical ENSO cycle calculated from Nino3 Index (red dots) and PC1 of the tropical Pacific SSTA (blue dots). Large dots indicate the four seasons (i.e. SON, DJF, MAM and JJA). ..... - 33 -
Fig. 3.14 The canonical ENSO cycle calculated from Nino3 Index (red dots) and the first Projection Coefficients (PjC1) of the tropical Pacific SSTA (blue dots). Large dots indicate the four seasons (i.e. SON, DJF, MAM and JJA). ..... - 34 -
Fig. 3.15 Peak month count for the canonical ENSO for 1st-3rd leadtime (left column), 4th-6th leadtime (center column) and the total count (right column) and the count using Nino3 Index (top row), PC1 of the tropical Pacific SSTA (middle row) and the Projection Coefficients (PjC1; bottom row) ..... - 36 -
Fig. 3.16 Peak season count for the canonical ENSO for 1st-3rd leadtime (left column), 4th-6th leadtime (center column) and the total count (right column) and the count using Nino3 Index (top row), PC1 of the tropical Pacific SSTA (middle row) and the Projection Coefficients (PjC1; bottom row) ..... - 37 -
Fig. 3.17 The ENSO Modoki cycle calculated from EMI (red dots) and PC2 of the tropical Pacific SSTA (blue dots). Large dots indicate the four seasons (i.e. SON, DJF, MAM and JJA). ..... - 39 -

Fig. 3.18 The ENSO Modoki cycle calculated from EMI (red dots) and the secnod Projection Coefficients (PjC2) of the tropical Pacific SSTA (blue dots). Large dots indicate the four seasons (i.e. SON, DJF, MAM and JJA). - 40 -
Fig. 3.19 Peak month count for the ENSO Modoki for 1st-3rd leadtime (left column), 4th-6th leadtime (center column) and the total count (right column) and the count using EMI (top row), PC2 of the tropical Pacific SSTA (middle row) and the Projection Coefficients (PjC2; bottom row) - 41 -
Fig. 3.20 Peak season count for the ENSO Modoki for 1st-3rd leadtime (left column), 4th-6th leadtime (center column) and the total count (right column) and the count using EMI (top row), PC2 of the tropical Pacific SSTA (middle row) and the Projection Coefficients (PjC2; bottom row) - 42 -
Fig. 3.21 Correlation coefficients between observed and model-predicted monthly mean (a, b) Nino3 index and (c, d) EMI, for (a, c) DJFMAM and (b, d) MAMJJA prediction cycles. - 45 -
Fig. 3.22 Taylor Diagrams for simulated a) Nino3 Index and b) EMI with the observations as reference point - 47 -
Fig. 3.23 Scatter plots for (b-h) monthly SSTA projections onto the observed 1st and 2nd EOF (denoted by PjC1 and PjC2, respectively) for 1-to-3 (red) and 4-to-6 (blue) month-lead predictions from individual models as well as their MME average. (a) Same projections but using observed SSTA. See text for details. - 50 -
Fig. 3.24 Auto-correlation function for monthly mean (a, b) Nino3 index and (c, d) EMI from (a, c) 1-to-3-month and (b, d) 4-to-6-month lead SST predictions from individual models as well as their MME average. Also shown are the values computed from observed SST... - 53 -
Fig. 3.25 Composite SSTA after the peak of canonical El Niño events in the MAMJJA season of 1983, 1988 and 1998, from (a) observations, (b) Model A, (c) Model B, (d) Model C, (e) Model D, (f) Model E, (g) Model F, (h) MME mean, averaged over 10°S-10°N. See scale bar at bottom (units: °C). - 56 -
Fig. 3.26 Same as Fig.3.24, but after the peak of El Niño Modoki events in 1987, 1991, 1992, 1995, 2003 and 2005. See scale bar at bottom (units: °C). - 58 -
Fig. 4.1 Composite for (a, c, e, g) anomalous rainfall (shading; see scale bar at bottom left, units: mm/day), 850hPa wind (vectors; see scale arrow at top right of each panel, units: ms^{-1}) and stream function (contours; in intervals of $10^6 m^2 s^{-1}$), and (b, d, f, h) the corresponding SSTA (shading; see scale bar at bottom right, units: °C), 200hPa divergent wind (vectors; see scale arrow at top right of each panel, units: ms^{-1}) and velocity potential (contours; in intervals of $10^6 m^2 s^{-1}$) in MAM after the peak of El Niño events in 1983, 1988 and 1998. The letter "A" indicates the position of the low-level anticyclone in western north Pacific. See text for details. Dotted regions over the ocean indicate SSTA significant to the 90% confidence level. - 66 -
Fig. 4.2 Same as Fig.4.1, but for the JJA season. - 69 -

Fig. 4.3 Same as Fig.4.1, except for the MAM season after the peak of El Niño Modoki events in 1987, 1991, 1992, 1995, 2003 and 2005 ..... - 73 -
Fig. 4.4 Same as Fig.4.3, but for the JJA season. ..... - 77 -
Fig. 4.5 Pattern correlation between observed and model-predicted anomalous rainfall in JJA over East Asia [10°S-40°N; 90°E-150°E] vs. pattern correlation for (a, c) SSTA in JJA over the equatorial Pacific [20°S-20°N; 120°E-70°W] and (b, d) the 850hPa mean stream function over the same East Asian region computed based on observations and model outputs. East Asian rainfall was predicted with leadtime of 1 to 3 (red markers) and 4 to 6 (blue markers) months, after the peak of (a, b) canonical El Niño events in 1983, 1988 and 1998, and (c, d) El Niño Modoki events in 1987, 1991, 1992, 1995, 2003 and 2005, for the JJA season. See legend at bottom. ..... - 81 -
Fig. 4.6 Taylor diagrams of pattern correlation coefficients of a) mean streamfunction over EA, b) canonical *El Niño* SST, c) Modoki SST, d) *El Niño* precipitation over EA and e) Modoki precipitation over EA with observed standard deviations as referenece point. .. - 82 -
Fig. 4.7 Climatological mean 850hPa stream function (contour; in intervals of $2.5\times10^6 m^2s^{-1}$) and 850hPa wind (vector; see scale arrow at top right of each panel, units: ms^{-1}) during the JJA season from (a) observations, (b) MME average, (c) Model C, (d) Model D and (e) Model E. ..... - 84 -
Fig. 5.1 1st EOF of the Indian Ocean SSTA [40S-20N; 30E-120E] ..... - 92 -
Fig. 5.2 2nd EOF of the Indian Ocean SSTA [40S-20N; 30E-120E] ..... - 94 -
Fig. 5.3 3rd EOF of the Indian Ocean SSTA [40S-20N; 30E-120E] ..... - 95 -
Fig. 5.4 4th EOF of the Indian Ocean SSTA [40S-20N; 30E-120E] ..... - 97 -
Fig. 5.5 Lead-lag correlation functions between the PjC1 of the tropical Pacific SSTA (canonical ENSO) vs IOBM (top left), IOD (top right), SIOD (bottom left) and the EOF4 (bottom right). Dash lines indicate 95% significance level using R-test. ..... - 99 -
Fig. 5.6 Lead-lag correlation functions between the PjC2 of the tropical Pacific SSTA (Modoki) vs IOBM (top left), IOD (top right), SIOD (bottom left) and the PjC of the EOF4 of the Indian Ocean SSTA (bottom right). Dash lines indicate 95% significance level using R-test. ..... - 100 -

List of Tables

Table.2.1 Summary of models used in this study……..6

Table.3.1 Correlation coefficients between PjC1 and PjC2……47

Table.5.1 Correlation Coefficients between the IO SST indices and IO SST Principle Component……..97

Acknowledgments

I would like to express my deep thanks to my supervisor Dr. Keith Ngan. He gave me a large degree of freedom for my thesis showing great trust to me. He tried to teach me all he knows about the present study from the technical knowledge to writing skills. Many suggestions from him make this thesis a completed work. I also appreciate his patience to me.

I would also like to express my deep gratitude to my thesis adviser Dr. Francis Tam. He leads me to explore the world of meteorology with his knowledge and patience. He does not only teach me academic knowledge, but also the attitude in dealing with affairs furthering my vision. I also appreciate him to give me so much encouragement, although I encounter problems or make mistakes when doing the research. This study cannot be completed without his help.

I appreciate Dr Doo Young Lee and Dr Joong-Bae Ahn from Pusan National University and the institutes participating in prediction of the APCC multi-model ensemble operating system for providing the Tier-1 hindcast experimental data. The data enriches the content of the present study making the analysis more comprehensive.

I also thank Prof. Johnny Chan and Dr. Wen Zhou who gave me a lot of useful advices. They pointed out some insufficiency of the approach and groundwork which make me understand more about the theory and direction of the study.

I appreciate Mr. Hoffman Cheng and Mr Szeto Koon Chuen's help for the technical assistance. They taught me so much about the mathematics and computer techniques. Although those stuffs are complicated and tedious, they are always welcome to answer.

Finally, I should thank my parents who support my study and life. Hope that this little piece of work could make them proud.

Chapter 1

Introduction

Billions of people are living in East Asia (EA). In fact, accounting only for China and India, almost 40% of the world's population can be found in those regions. In recent years, China also acts as a host connecting economy of East Asian countries via the 21st Century Maritime Silk Road. Therefore, no one can deny that the East Asia regions are not only growing in population but also their roles in the world's economy. In this regard, understanding EA climate becomes a vital subject, as it affects agriculture, aviation, construction, transportation and so on. The first question here is: what are the main factors affecting East Asian climate? When looking at the world map, one can easily find that the East Asian region is actually surrounded by the Pacific Ocean and Indian Ocean (IO). This further encourages us to investigate what and how the variability of the two oceans affects the East Asia.

El Niño Southern Oscillation (ENSO/canonical ENSO) is no doubt the most variable climate phenomenon over the tropical Pacific [Rasmusson and Carpenter (1982); Philander (1990)]. With its huge impacts on tropical and extra-tropical regions, ENSO has long aroused many researchers' concern producing numerous studies on it. ENSO which refers to the anomalous warming of the sea surface temperature over the tropical eastern Pacific has profound influence on the global climate [Ross (2000)]. However, in the recent decade, many studies suggested a different type of ENSO over the Pacific oceans known as El Niño Modoki referring to the anomalous warming of sea surface temperature over the central Pacific [Larkin and Harrison (2005), Kumur *et al*. (2006), Ashok *et al*. (2007), Wang and Hendon (2007), Yu and Kao (2007), Kao and Yu (2009); Kug *et al*. (2009)]. It is also found that ENSO Modoki could affect the global climate in a large extent [Ashok *et al*. (2007)]. In fact, the canonical ENSO and ENSO Modoki are the first and second most variable phenomenon respectively over the Pacific oceans. As Lau *et al*. (2000) and Wang *et al*. (2001) pointed out the response of the canonical ENSO to different regional components of the Asian monsoon, increasing number of studies are done against the relationship between ENSO and Asian monsoon concerning not only the mature phase of ENSO but also the developing and decaying phase [Chan and Zhou (2005), Chang *et al*. (2000), Feng *et al* (2010), Huang *et al*. (2004), Zhou and Chan (2007); Zhou *et al*. (2009)]. Xie *et al*. 2009 suggest that the main factor of the response of the canonical ENSO to the Asian monsoon is the activity of the low level anti-cyclone over the Philippines seas affected by the delayed impact of the Indian Ocean. For ENSO Modoki, Weng *et al*. (2007) and Weng *et al*. (2009) observed that the western North Pacific (East Asia) summer monsoon is strengthened (weakened) when El Niño Modoki develops. Asian regions like Bay of Bengal, the Philippines and the southern China are more likely to be wet; at the same time Japan and the Yangtze River valley will suffer from drought. On the other hand Feng *et al*. (2010) pointed out that an anomalous low-level anticyclone is centered over the South China Sea during

the mature phase of ENSO Modoki. This implies suppressed rainfall over southeastern China, Taiwan and southern Japan. Also, the summertime rainfall is enhanced (suppressed) in the Huaihe River (southern China) during the decaying phase of ENSO Modoki. All of the above studies show that the canonical ENSO and ENSO Modoki have completely different impacts on the Asian monsoon during the evolution of the two types of ENSO. Therefore, distinguishing these two types of ENSO flavors should help understand a lot about the tropical climate.

Although the canonical ENSO contributes the largest variability (about 40%) of SSTA over the Pacific than ENSO Modoki (about 15%), Yu and Kim indicates that most CMIP3 models are able to reproduce realistically strong Central-Pacific ENSO, while lesser models reproduce the conventional ENSO. Based on IPCC climate model projections, Yeh *et al*. (2009) also reported that the ratio of ENSO Modoki to canonical ENSO tends to increase under global warming, which is relevant to the present state of the real world [Ashok *et al*. (2007)]. A number of studies have been carried out for the simulations of the canonical ENSO (e.g. Guilyardi *et al*. (2009)). However, a study focusing on the impact of Modoki events using coupled GCMs is not yet to be seen.

Another possible factor affecting East Asian climate is the Indian Ocean SST. Indian Ocean SST modes draw meteorologists' attention after Saji *et al*. (1999) suggest the Indian Ocean Dipole (IOD) mode by analyzing 40-year SST data over the tropical Indian Ocean. IOD describes the East-West SST gradient over the tropical Indian Ocean which can be indicated by the Dipole Mode Index (DMI). However, it is worthy noted that Saji *et al*. (1999) find that the IOD only accounts for 12% variability in the Indian Ocean. After the work, numerous studies are made against the IO SST modes. Thank for the previous studies two new IO SST modes are recognized. The first one is the Indian Ocean Basin (IOB) mode, which describes the anomalous warming over the whole tropical Indian Ocean (without negative SSTA over the eastern IO) [Deser *et al*. (2010), Du *et al*. (2009), Saji *et al*. (2006); Yang *et al*. (2007)]. The second one is the Subtropical Indian Ocean Dipole

(SIOD) [Behera SK and Yamagata T (2001)], which is referred to the warm (cold) SST over the south western IO and cold (warm) SST south eastern IO as positive (negative) phase. Xie *et al* (2009) find that the IOB mode can affect the EA climate about 3-6 months after the peak of the canonical ENSO, while Feng and Chen (2013) suggest that the IOD may have influence on *El Niño* Modoki and the East Asian summer monsoon. However, no report is found about the relationship of ENSO and SIOD. The relationship of the IOB mode and canonical ENSO seems to be clearly defined. Nevertheless, it should be emphasized that the variability of IOD is small compared to the IOB mode, especially for the period after 1980s (will be shown in Chapter 5). Therefore, differentiating the IO SST modes and their impacts on ENSO and EA climate are definitely an important work to do.

After viewing some characteristics of the two flavors of ENSO and the Indian Ocean warming, it is no doubt that more studies should be carried out against the characteristics and impacts of the phenomenon. Although the study of the canonical ENSO is mature for some aspect, researchers are only touching the beginning of El Niño Modoki. One of the reasons is that El Niño Modoki is still relatively new compared with the canonical ENSO. Another reason is the limitation of data. A huge number of observations are required to produce convincing results for this type of research. The same situation happens when analyzing the Indian Ocean SST. For this reason, accessing GCM data and performing GCM experiments with the help of statistical tools are the crucial methods to study the phenomenon and this is the focus of the present study. Moreover, a good statistical analysis to models allows us to summarize the behavior of climate models because there are always a large set of models to deal with when doing analyzing hindcast model data. The analysis of the present study can be divided into two aspects. The first part focuses on how the two types of ENSO behave in spatial and time evolution and the different impacts of the two ENSO flavors. The second part is to access the Indian Ocean SST modes and try to relate them to the two types of ENSO.

The outline of the rest of the study is organized as follows. Dataset being used in this study will be described in Chapter 2. In Chapter 3, the general behaviors of the two flavors of ENSO and their predictability by coupled models will be studied. How well the coupled models can capture the impacts of El Niño and El Niño Modoki on the East Asian climate and the impacts reveal in CGCM are examined in Chapter 4. Chapter 5 gives the analysis of the behaviors of Indian Ocean warming and its relationship with the two flavors of ENSO. More detailed introduction can be found in each chapter. Finally, the discussion and summary of the study are given in Chapter 6.

Chapter 2

Description of Datasets

2.1 Reanalysis Data

Observational data used in this study include the Hadley Center Global SST (HadSST) dataset with 1°×1° resolution [Rayner *et al.* (2006)], Climate Prediction Center Merged Analysis of Precipitation (CMAP) [Xie and Arkin (1997)] in 2.5°×2.5° resolution, as well as upper-air reanalysis data from the National Centers for Environmental Prediction–National Center for Atmospheric Research (NCEP/NCAR) [Kalnay *et al.* (1996)], again in 2.5°×2.5° resolution.

2.2 Coupled Model hindcast data

For coupled global circulation model (CGCM) data, multi-model ensemble (MME) hindcast experiments from the Asia Pacific Economic Cooperation Climate Center (APCC) were used. The MME comprises the APCC CGCM [Jeong *et al*. (2008)], NCEP Climate Forecast System (CFS) [Saha *et al*. (2006)], the Pusan National University (PNU) CGCM [Joong and Hwang (2005)], the Predictive Ocean-Atmosphere Model for Australia (POAMA) of the Bureau of Meteorology Research Center (BCC) [Alves *et al*. (2003)], the Seoul National University (SNU) [Kug *et al*. (2007)] and the University of Hawaii (UHT1) CGCM [Fu and Wang (2004)]. Table.2.1 summarizes the configurations and resolutions of the six models.

Historical forecasts for the duration of 6 months were conducted four times per year, with initial times in March, June, September and December, from 1983 to 2005. Fig.2.1 gives a schematic representation of the initializing scheme of the APCC models. Finally, all model data were interpolated on the same 2.5°×2.5° regular grid before carrying out any analyses.

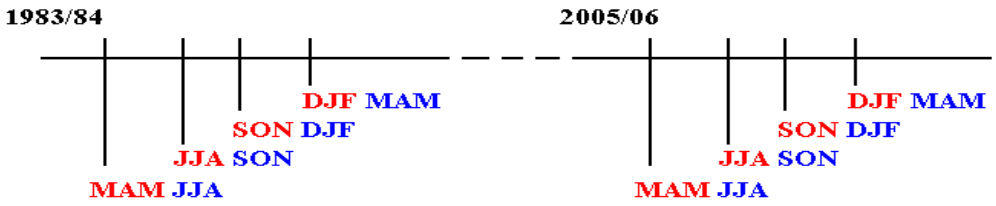

Fig. 2.1 Schematic representation of forecast dates of APCC models

Table.2.1 Summary of models used in this study

Model	Institute	Abbreviation	AGCM resolution	OGCM resolution	Ensemble number	References
A	Asia-Pacific Economic Cooperation Climate Center	APCC	CAM3 (T85L26)	POP1.3 (G×1v3 L40)	5	Jeong *et al.* (2008)
B	National Center for Environmental Prediction	NCEP	GFS (T62L19)	MOM3 (1/3° lat × 1°lon L40)	15	Saha *et al.* (2006)
C	Pusan National University	PNU	CCM3 (T42L18)	MOM3 (1/3° lat × 1°lon L40)	5	Joong and Hwang (2005)
D	Predictive Ocean–Atmosphere Model for Australia	POAMA	BAMv3.0d (T47L17)	ACOM2 (0.5°-1.5°lat × 2°lon L25)	10	Alves *et al.* (2003)
E	Seoul	SNU	SNU	MOM2.2	6	Kug *et al.*

	National University		(T42L21)	(1/3° lat × 1°lon L32)		(2007)
F	University of Hawaii	UH	ECHAM4	1°lat × 2°lon	10	Fu and Wang (2004)

2.3 General data processing and some typical equations

This section is intended to explain some general arrangement of the datasets and the forms of some typical equations used in this thesis. For some specific equations, details of them will be given in the individual sections. The general period in this study mainly covers 1983-2005/06. Since the number of *El Niño* events during this period is not large, the Student's t test will be applied to ensure the significance of the results.

As Fig.2.1 shown, hindcast experimental data are stratified into two sets, namely those with 1 to 3 months (red) and those 4 to 6 months (blue) of forecast leadtime. They construct two individual continuous time series respectively. Comparison between the results based on these two datasets should shed light on how forecast leadtime can affect predictions of ENSO and ENSO Modoki in models.

Three-month running mean are applied to most climate variables in this study to obtain the seasonal signal of those variables (smoothing the data). The method is simply taking the mean value for a certain month data with the previous and next month data. The variable like SST, wind field

and SLP are fit to be processed with three-month running mean. It is noticed that, to apply the three-month running mean method to a certain time series, the end points of the series are extended identically. For example, a time series like 1, 2, 4, 5, 3 should be extended as 1, 1, 2, 4, 5, 3, 3 in order to produce a smoothed time series with the same dimension before applying the filter.

1-2-1 filter is applied on the precipitation. This method is similar to the three-month running mean method. However, the data of the target month have been multiplied by 2 so that the seasonal signal of the precipitation can be revealed. The following equation shows how the 1-2-1filter exactly works for certain variable T:

$$T_{1-2-1} = \frac{T_{j-1} + 2T_j + T_{j+1}}{4}$$

j is the month index.

The Niño3 index which is defined as the SSTA averaged over the tropical eastern Pacific region of 5°S – 5°N, 150°W – 90°W is used to identify canonical ENSO events:

$$\text{Nino3} = [\text{SSTA}]_{5°\text{S}-5°\text{N};150°\text{W}-90°\text{W}}$$

To capture SSTA typical of ENSO Modoki events, the El Niño Modoki index (EMI) is given by the weighted area averaged SSTA:

$$EMI = [SSTA]_A - 0.5\times[SSTA]_B - 0.5\times[SSTA]_C$$

with regions A, B and C found over the central, eastern and western Pacific locations of 10°S–10°N; 165°E–140°W, 15°S–5°N; 110°W–70°W and 10°S–20°N; 125°E–145°E respectively [Ashok *et al.* (2007)]. A canonical El Niño event is identified by Niño3 index during DJF whenever exceeds 1 standard deviation of the time series; analogously, an El Niño Modoki event is identified if EMI in

DJF exceeds 0.7 of its standard deviation [Ashok *et al*. (2007)]. During the period of 1983 to 2005, 1982-83, 1987-88 and 1997-98 are found to be canonical El Niño events, whereas El Niño Modoki episodes are identified during 1986-87, 1990-91, 1991-92, 1994-95, 2002-03 and 2004-05. Composite maps will be examined in order to study the characteristic of ENSO related SSTA and the atmospheric circulation given by observations and model hindcast.

There are also some indices to define the Indian Ocean Warming modes. For Indian Ocean Basin Mode:

$$\text{IOBM index} = [\text{SSTA}]_{40\text{E-}100\text{E};\ 10\text{S-}10\text{N}}$$

The Indian Ocean Dipole (IOD) can be represented by Dipole Mode Index (DMI):

$$\text{DMI} = [\text{SSTA}]_{50\text{E-}70\text{E};\ 10\text{S-}10\text{N}} - [\text{SSTA}]_{90\text{E-}110\text{E};10\text{S-}0\text{N}}$$

Finally, the Subtropical Indian Ocean Dipole (SIOD) can be represented by SIOD index:

$$\text{SIOD index} = [\text{SSTA}]_{55\text{E-}65\text{E};\ 37\text{S-}27\text{S}} - [\text{SSTA}]_{90\text{E-}100\text{E};28\text{S-}18\text{S}}$$

Chapter 3

The Two Flavors of ENSO and their Seasonal Predictions' Skill in Coupled Models

In this chapter, the characteristics of the two flavors of ENSO are examined. The hindcast data from CGCMs are also studied to manifest the behavior of the two flavors ENSO in the model environment. To achieve this objective, some statistical methods are used. That is, correlation coefficient, SST variance plot, lag-correlation, time-longitude composite plots and power spectra to indicate the characteristics of ENSO skill, amplitude, persistence, evolution and time scales. Moreover, the mixings between the two flavors of ENSO in the CGCMs are also studied. In this case, the projection coefficient scatter plots are employed to reveal the degree of mixings of the two ENSO (the detailed explanation of projection coefficient will be brought out later in this chapter).

3.1 Introduction

3.1.1 A review of the two flavors of ENSO and their behaviors in GCMs

The evolution of the canonical ENSO has already been studied by researchers for decades. Wang *et al*. (2016) give a review on the whole evolution of the two types of ENSO. They introduce the unified oscillator model [Wang (2001)] to explain the evolution of canonical *El Niño*. For the decaying mechanism of canonical ENSO, there is a widely accepted conceptual model suggested by Jin (1997): Recharge Oscillator Model. The theory purposed that the energy of eastern Pacific warming during the canonical ENSO events will be discharged to the higher latitudes through the coastal Kelvin wave. Then, upwelling can be found over the equatorial eastern Pacific inducing cold SSTA, which is named La Nina events. This finding gives a good representation on how to access the decaying phase of canonical *El Niño* in models.

Yu and Kim (2010) tried to classify the different evolution patterns of ENSO Modoki using the observational data for 1958-2007. They drew out three types of evolution for ENSO Modoki. The first one is a symmetric-decaying pattern. That means the ENSO Modoki developing and decaying time scales are similar with respect to the peak phase. The second one is a prolonged-decaying pattern which decays slowly and is followed by an EP type ENSO event. The final one is an abrupt-decaying pattern whose SSTA decays rapidly and is followed by a cold event over the eastern Pacific. It should be pointed out that only about three events for each type of evolution patterns can be found during the studied period. On the hand, one can still find that the evolution patterns are quite different even for the same type of evolution patterns. However, this study successfully pointed out that the different evolution nature between the canonical ENSO and ENSO Modoki.

Kug and Ham (2011) argued that if there are two types of La Nina (i.e. La Nina and La Nina Modoki) in the Pacific. The findings were that when assuming the two types of La Nina as the same definition as the two types of El Niño events respectively. The two types of La Nina show similar SST and precipitation patterns in the observations. The researchers compared this result with the output of the CMIP3 models that supports their findings.

3.1.2 The Focus of the present Chapter

After reviewing the past studies of ENSO, one can find that the two types of *El Niño* are apparently two different phenomena in the observations. However, it should be admitted that limited number of observations is a large obstacle to investigate the phenomena. There are two ways to get rid of this limitation. The first one is to apply statistical analysis that indicates the associated significant level with the results. Another way is that using the data from Global Circulation Models (GCMs) that reproduce our climate system in the digital world. The idea here is to access *El Niño* events in a dynamical view (numerical models). Although the GCMs are not perfect representation of the real world, overall behaviors of the events can still be found in those models to help understand our real climate. In addition to this, there are some questions followed. How do CGCMs display the two flavors of ENSO? What states of Pacific warming could appear in the modeled environment? And would they also appear in the observations? What can the results tell us? Those questions are going to be addressed in this chapter.

3.2 Basic Climate State in CGCMs

Before accessing the behavior of the two flavors of ENSO in CGCMs, it is prior to investigate the basic state of the CGCMs. Fig.3.1-Fig.3.4 show the mean SST and 850hPa winds over the tropical Pacific for the observations and models during the SON, DJF, MAM and JJA seasons respectively. Fig.3.1 shows the mean SST during the SON season. For the observations, it is found that the warm pool is located on the western Pacific extending to the central Pacific (about 180˚E). The formation of the warm pool is due to the easterly trade winds over the tropical Pacific which forces the surface warm sea water accumulating on the western boundary of the Pacific rims. The warm pool extends evenly from the equator due to even insolation for this season.

For the 1^{st}-3^{rd} month lead predictions of the MME, it is observed that the overall models could give similar results to the observations except that the warm pool over the equatorial Pacific cannot extend to the central Pacific. The situation becomes worse for 4^{th}-6^{th} month lead predictions of the MME. This denotes that the double ITCZ problem [Lin (2007)] gets more severe for the models if the predicting lead time increases which means that the models predict too strong zonal background easterly. The enhanced easterly induces the Ekman transport along the equatorial Pacific resulting in the anomalous upwelling. This problem appears in some models such as Model B, Model C and Model E. The ocean model of Model F is a two-and-a-half-layer model; therefore, it can capture a stable mean SST as the leadtime grows. These models generally have too strong easterlies over the western Pacific (see the wind field). The observed equatorial winds maximize at 130˚W and reduce westwards. The winds then reach $5ms^{-1}$ at 170˚W, while the winds in those models generally reach $5ms^{-1}$ at 175˚E-180˚E.

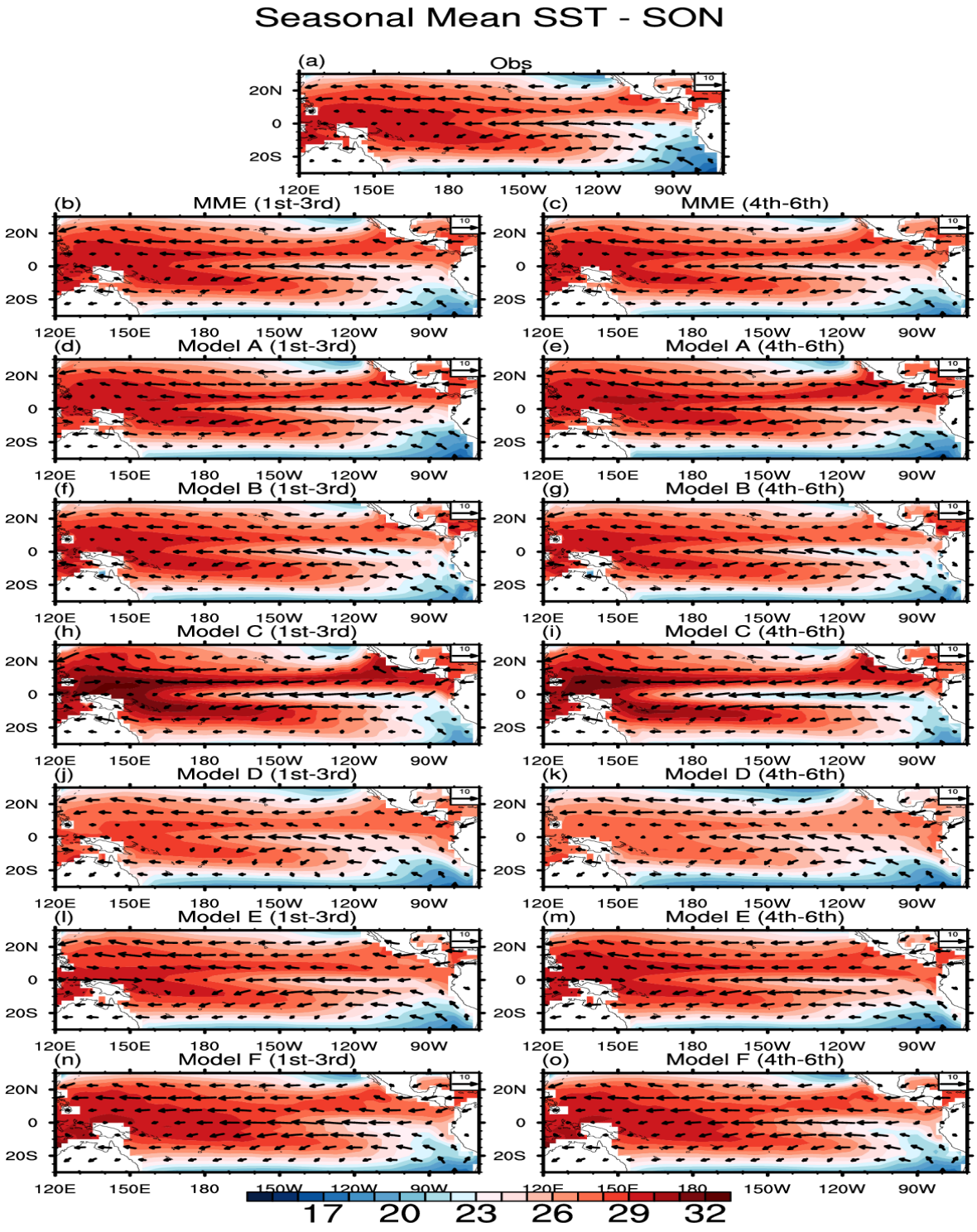

Fig. 3.1 Seasonal mean SST over Tropical Pacific region [20°S-20°N; 120°E-70°W] during SON season

For the mean SST during the DJF season (Fig.3.2), it is observed that the western Pacific warm pool is shifted to the south of the equator. It is because the insolation reduces on the Northern Hemisphere and increases on the Sothern Hemisphere in the boreal winter. It is seen that the models generally give good predictions for the mean SST during this season (Fig.3.2b and 3.2c). However, the models tend to overestimate the SST over the northern ocean of Indonesia except Model D and Model E. The possible reason is that the too strong easterly transports too much warm seawater to the western boundary of the Pacific.

Fig.3.3 shows the mean SST for the MAM season, the observations show that the North Sea of Indonesia becomes warm again because of the increase of insolation. Most of the models are able to simulate this feature. Nevertheless, some models get too warm in the central Pacific off the equator. They are Model C and Model E.

For the JJA season (Fig.3.4), the western boundary (e.g. the eastern sea of the Philippines) becomes fully heated. The MME shows that the models could give reasonable predictions to the western Pacific SST during this season.

It is concluded that the models generally could reproduce good mean Pacific SST. However, some of the models show insufficiency in predicting the equatorial SST signal because of the double ITCZ problem. The most severe model for this case is Model C. One the other hand, the MME and Model D give good predictions to the mean SST.

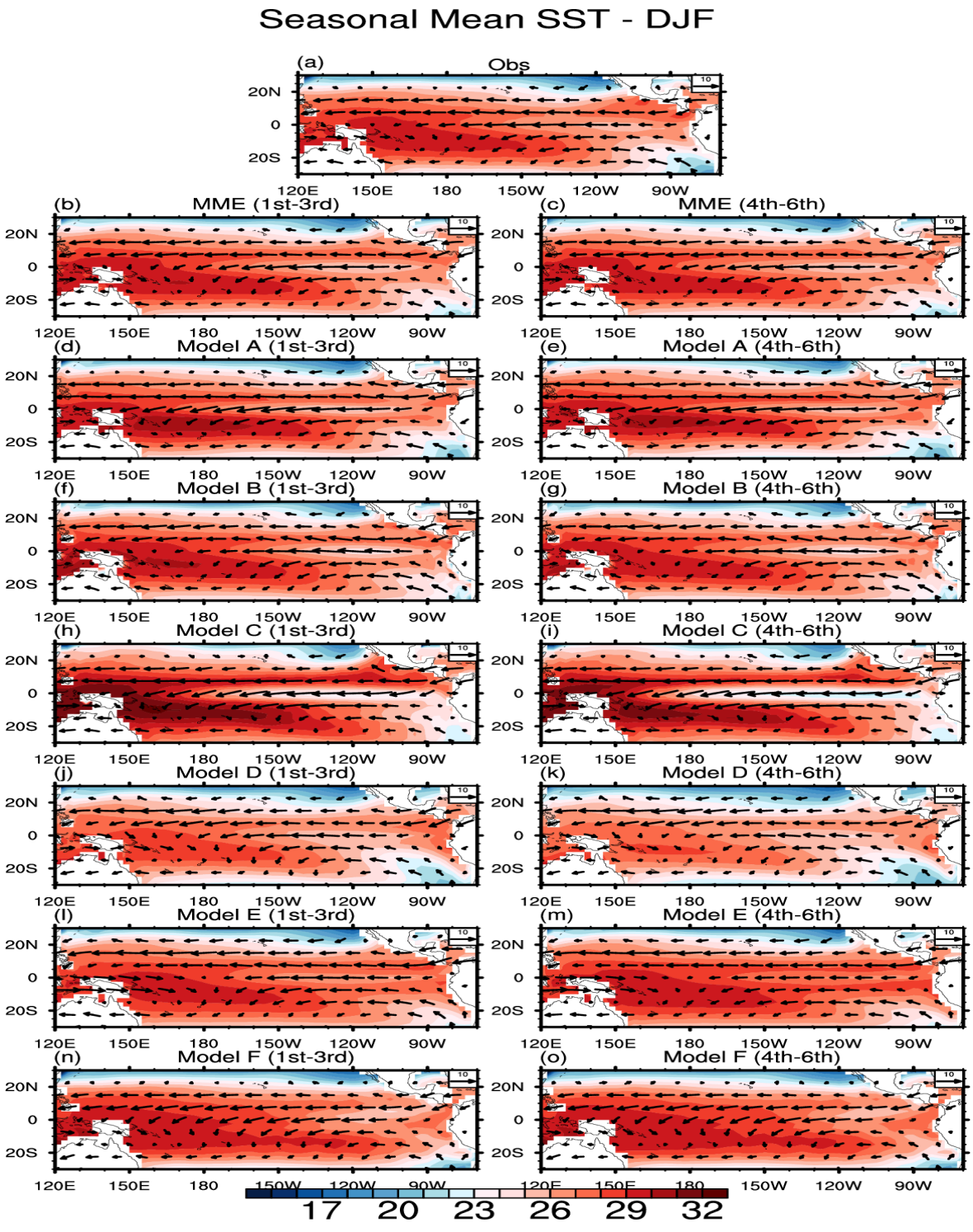

Fig. 3.2 The same as Fig3.1, except for DJF season

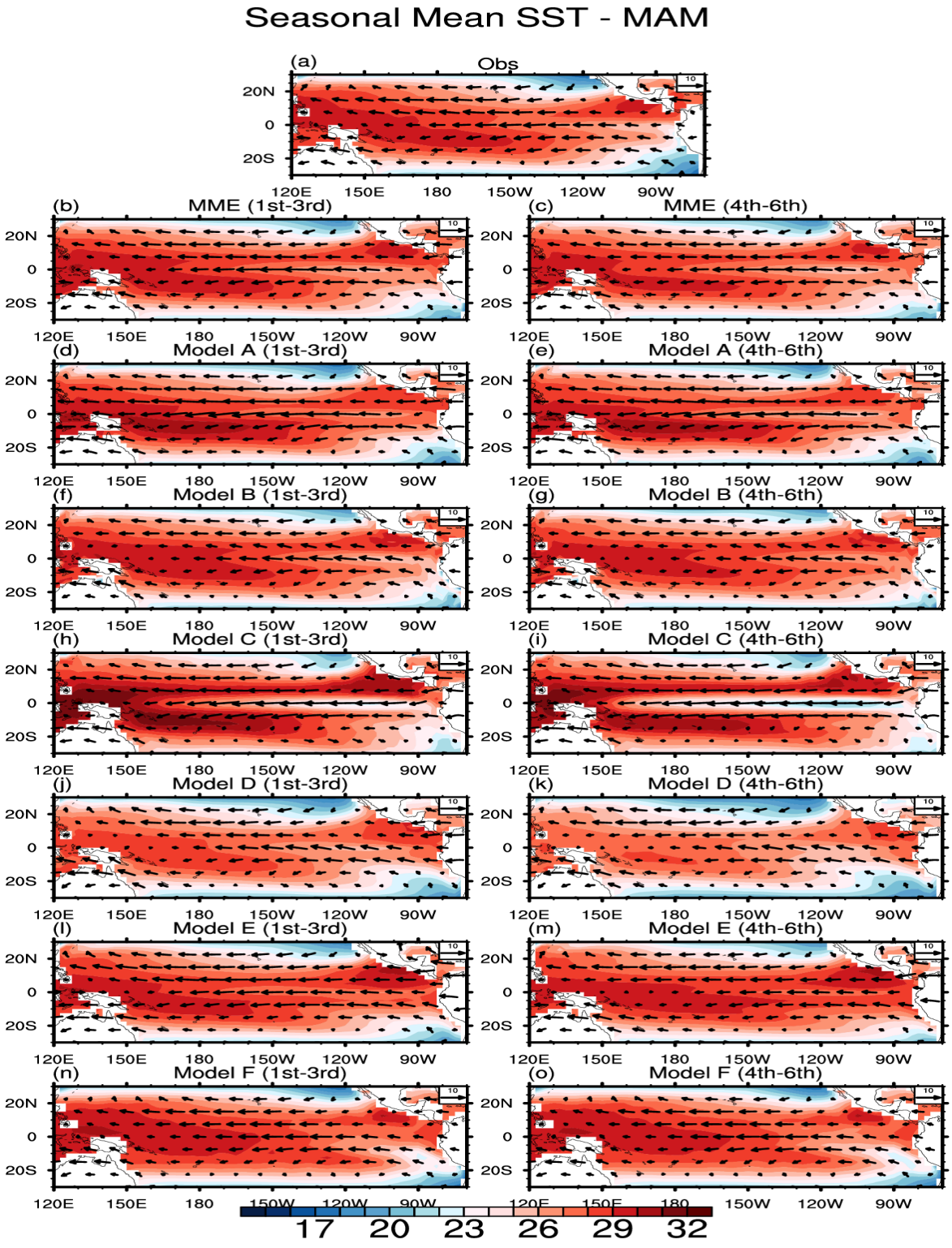

Fig. 3.3 The same as Fig3.1, except for MAM season

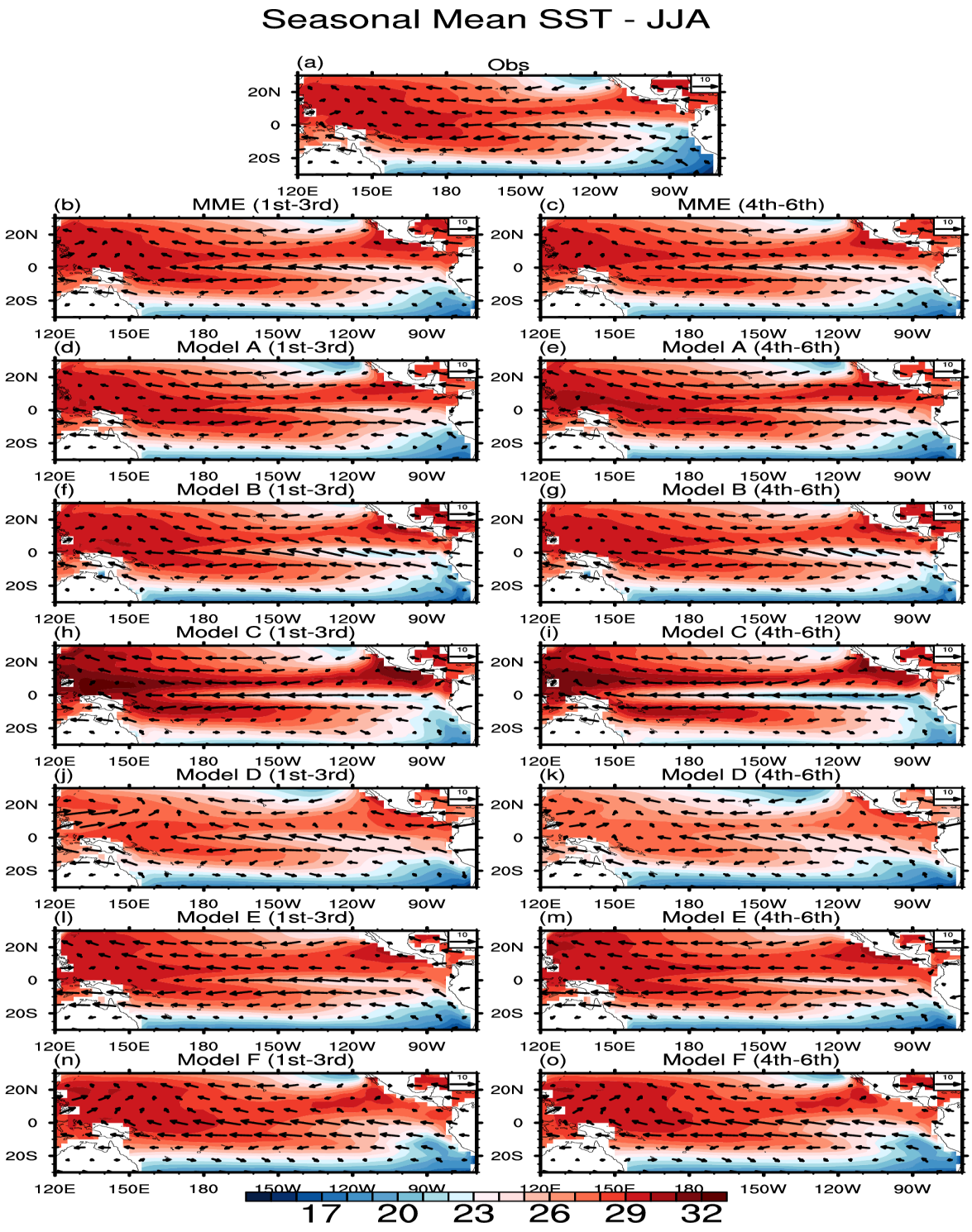

Fig. 3.4 The same as Fig3.1, except for JJA season

The SST variability is also one of the major characteristics of the performance for the models. Fig.3.5-Fig.3.8 shows the SST standard deviation of the models over the tropical Pacific during the SON season.

For the SON season, it is observed that the variability over the eastern Pacific is very high. The reason is that the two seasons are the peak season of ENSO. However, the models tend to shift the variable region to the central Pacific. The most severe model is Model C.

For the DJF season, it is observed that the variability over the central eastern Pacific is very high. The reason is similar to that of the SON season. The models further shift the variable region to west. Model C even displays the most variable region over the western Pacific.

For the MAM and JJA seasons, the variability is weaker compared with the SON and DJF season and the strongest region is located on the eastern Pacific. However, the behavior of the models diverges. It is concluded that the predictions of the SST variability is relatively poor because the models have different variation patterns.

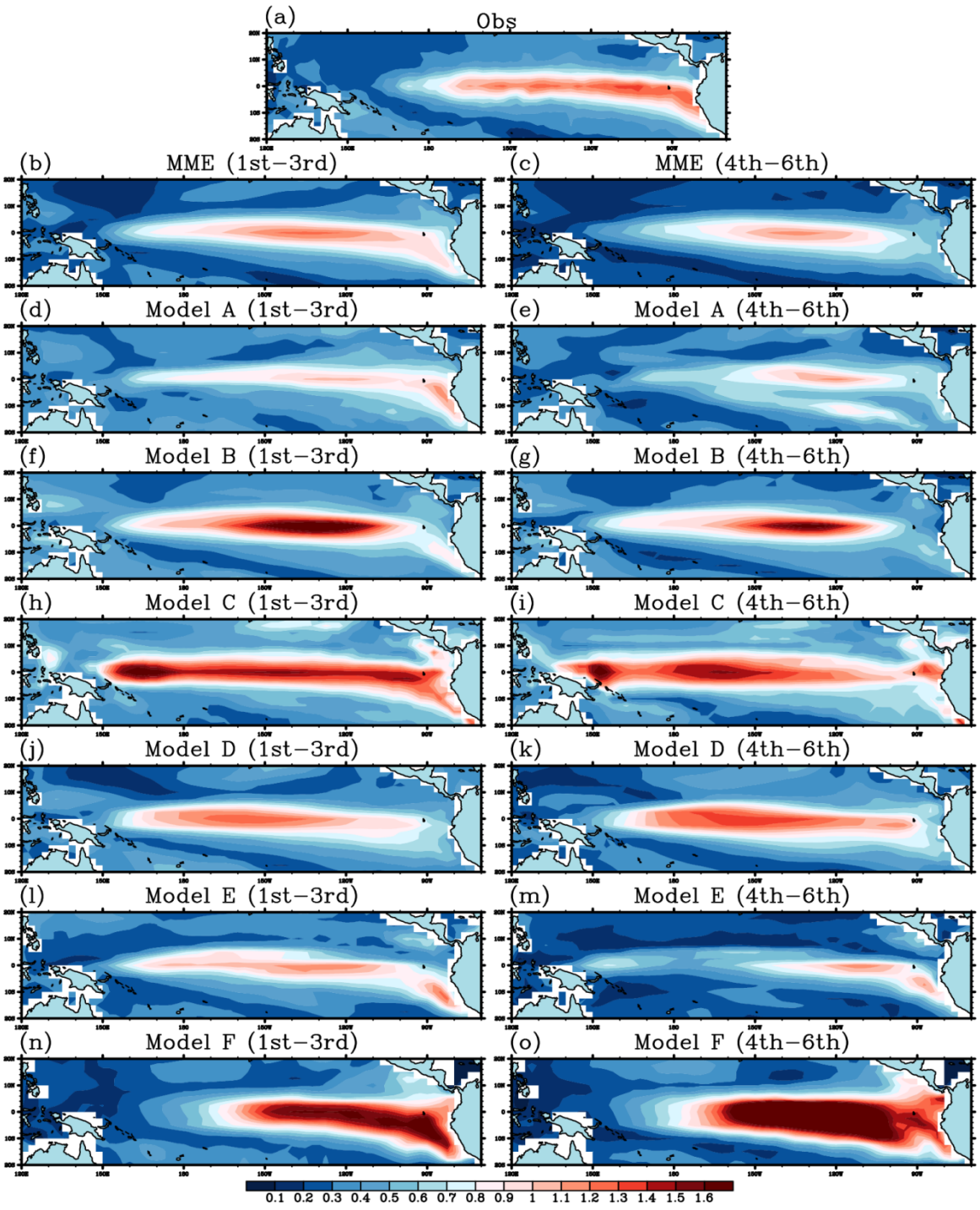

Fig. 3.5 SST standard deviation over Tropical Pacific region [20°S-20°N; 120°E-70°W] during SON season

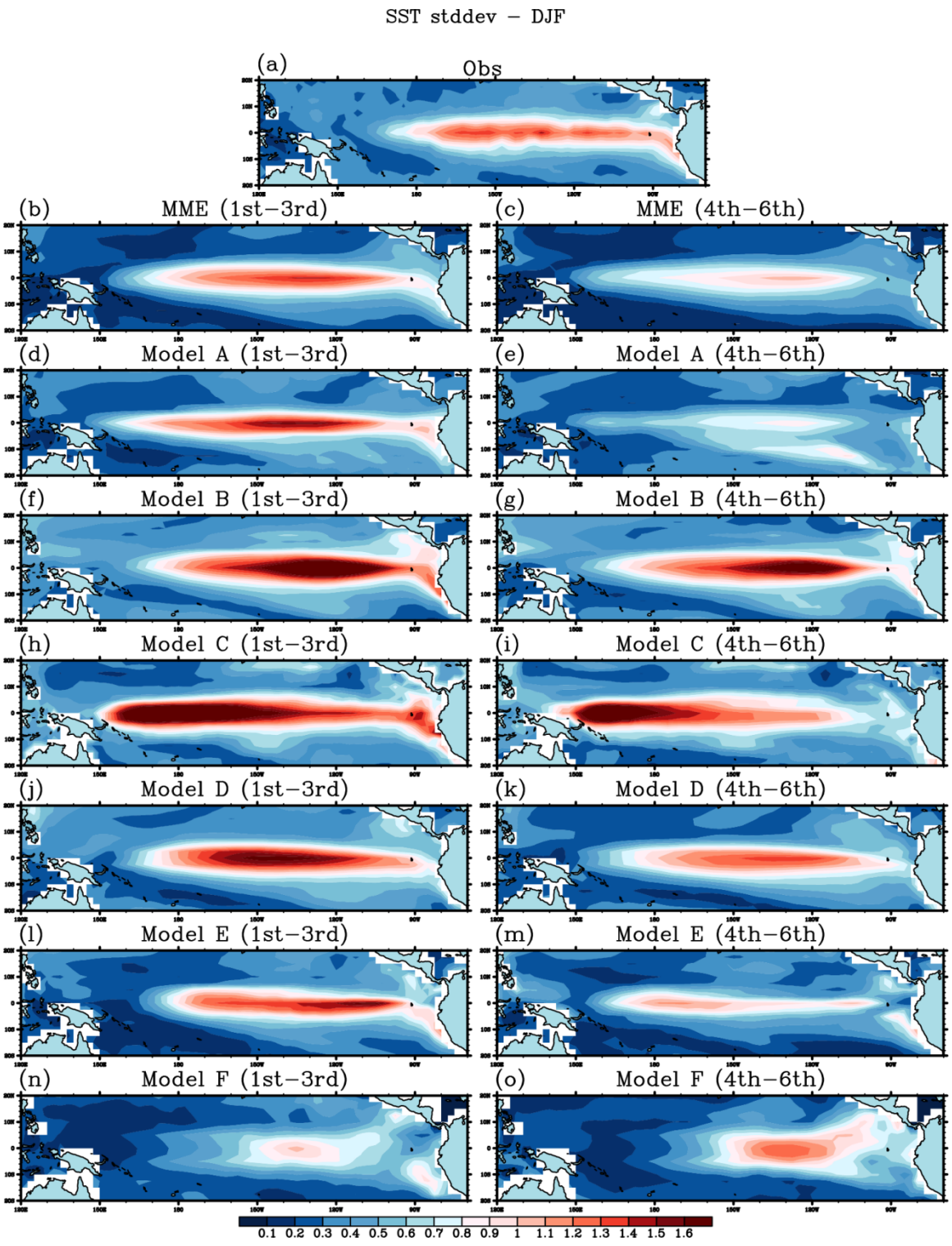

Fig. 3.6 The same as Fig3.1, except for JJA season

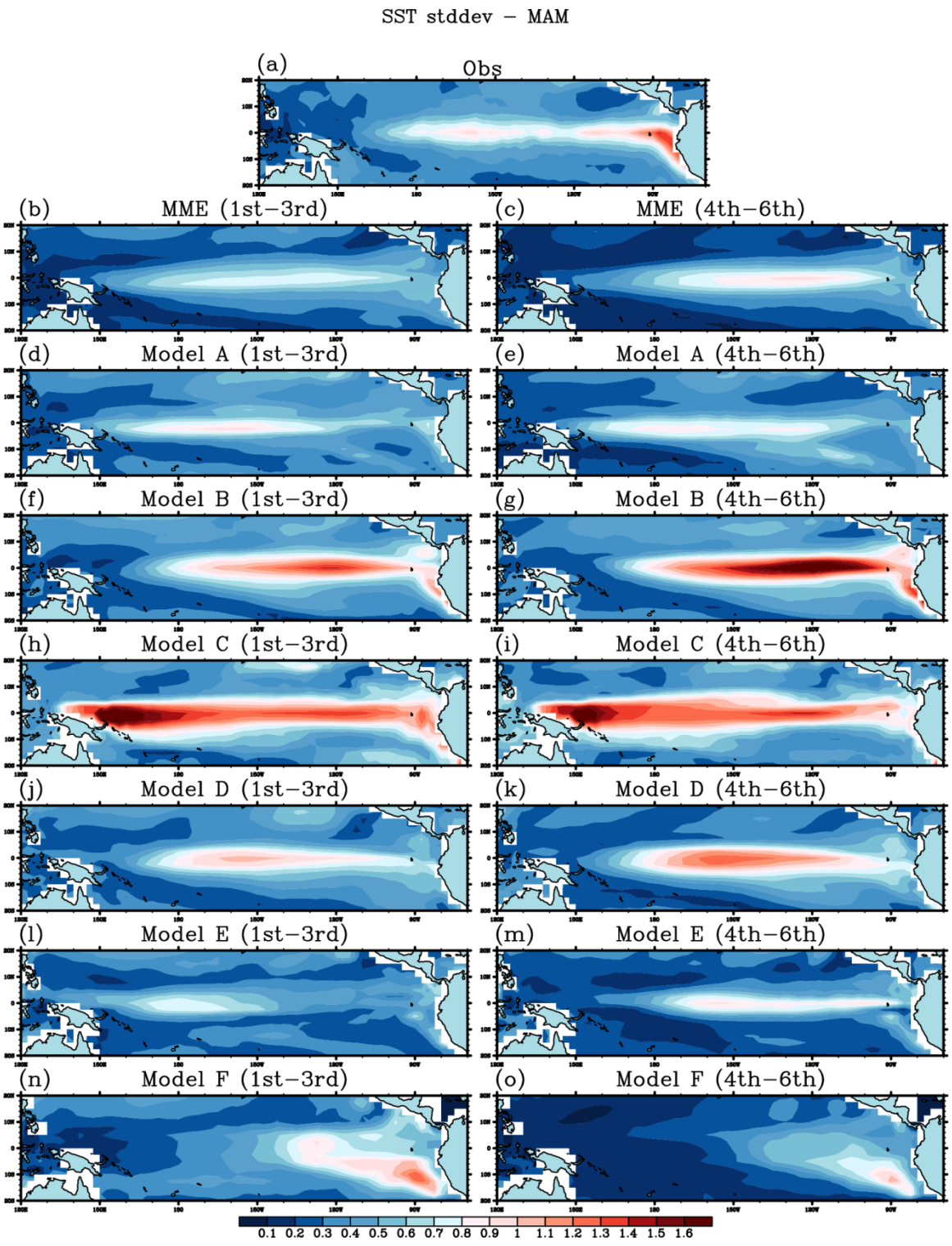

Fig. 3.7 The same as Fig3.1, except for MAM season

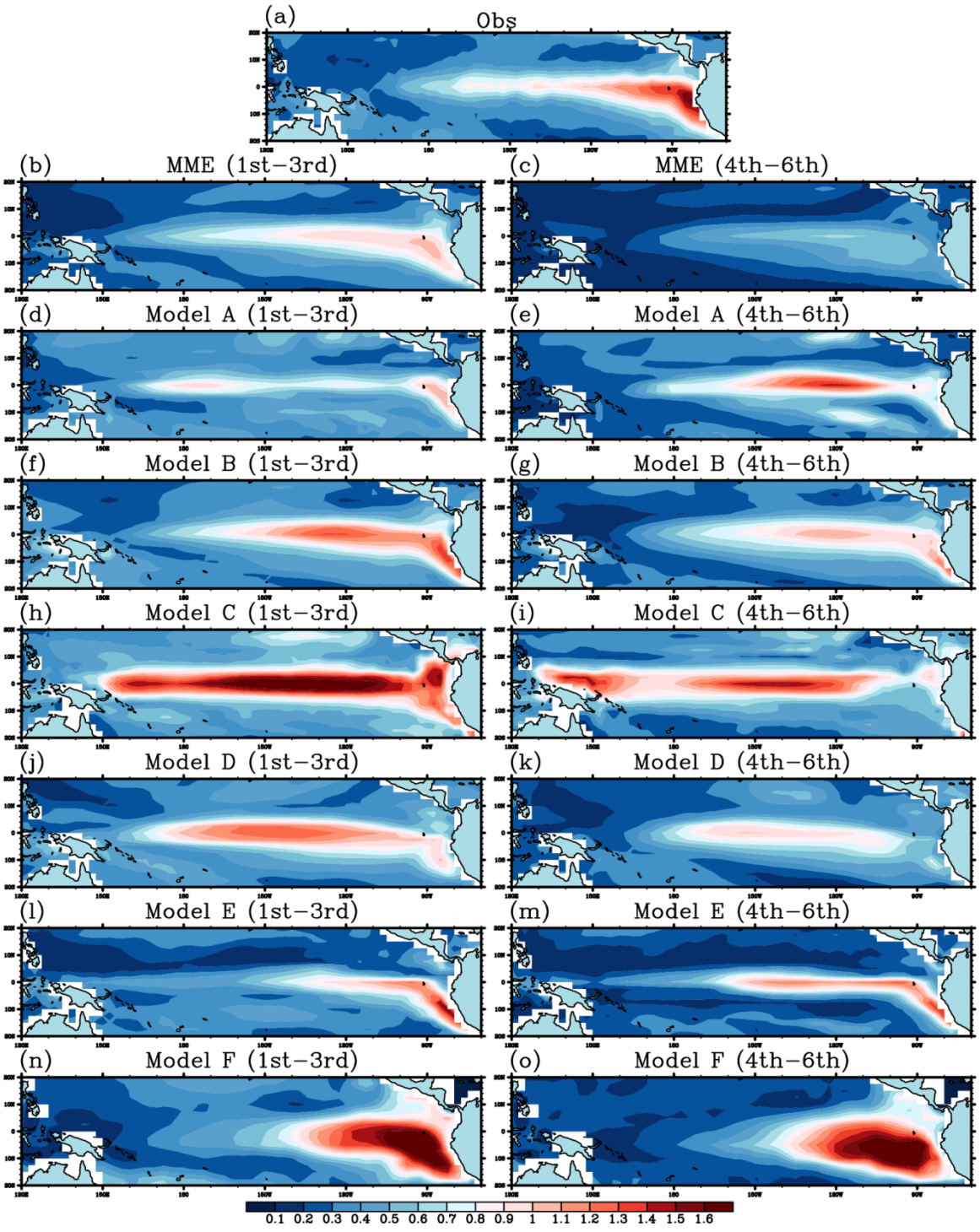

Fig. 3.8 The same as Fig3.1, except for JJA season

3.3 ENSO Patterns, Evolution and Amplitude

First of all, the two types of ENSO events should be identified before analyzing them. In this regard, the Empirical Orthogonal Function (EOF) analysis is employed. Fig.3.9 displays the first EOFs of the SSTA over the tropical Pacific region for the observations and APCC models. For the observed EOF (Fig.3.9a), the warming region is located over the eastern tropical Pacific. It is widely accepted that this first EOF pattern corresponds to the canonical ENSO. Although the variance contained for the first EOF for the models differs from each other, they can also show large number (even larger) like the observations. This denotes that the canonical ENSO is quite robust in the APCC CGCMs.

When looking at the MME average (Fig.3.9b & c), they show similar patterns compared with the observations. It denotes that the models generally could reproduce good predictions to the canonical ENSO. However, there are still some insufficiencies for the model average. For example, the eastern Pacific warming region is not stuck to the western coast of South America like that in the observations. This case becomes more obvious for the longer lead time predictions. The possible reason is that the models predict too strong zonal background easterlies along the equator. This weakens the westerly over the eastern Pacific during the canonical ENSO events inducing an anomalous upwelling over the eastern Pacific. In fact, this case appears in the different models like Model A, Model B and Model C. Nevertheless, there are models behaving well such as Model D and Model E.

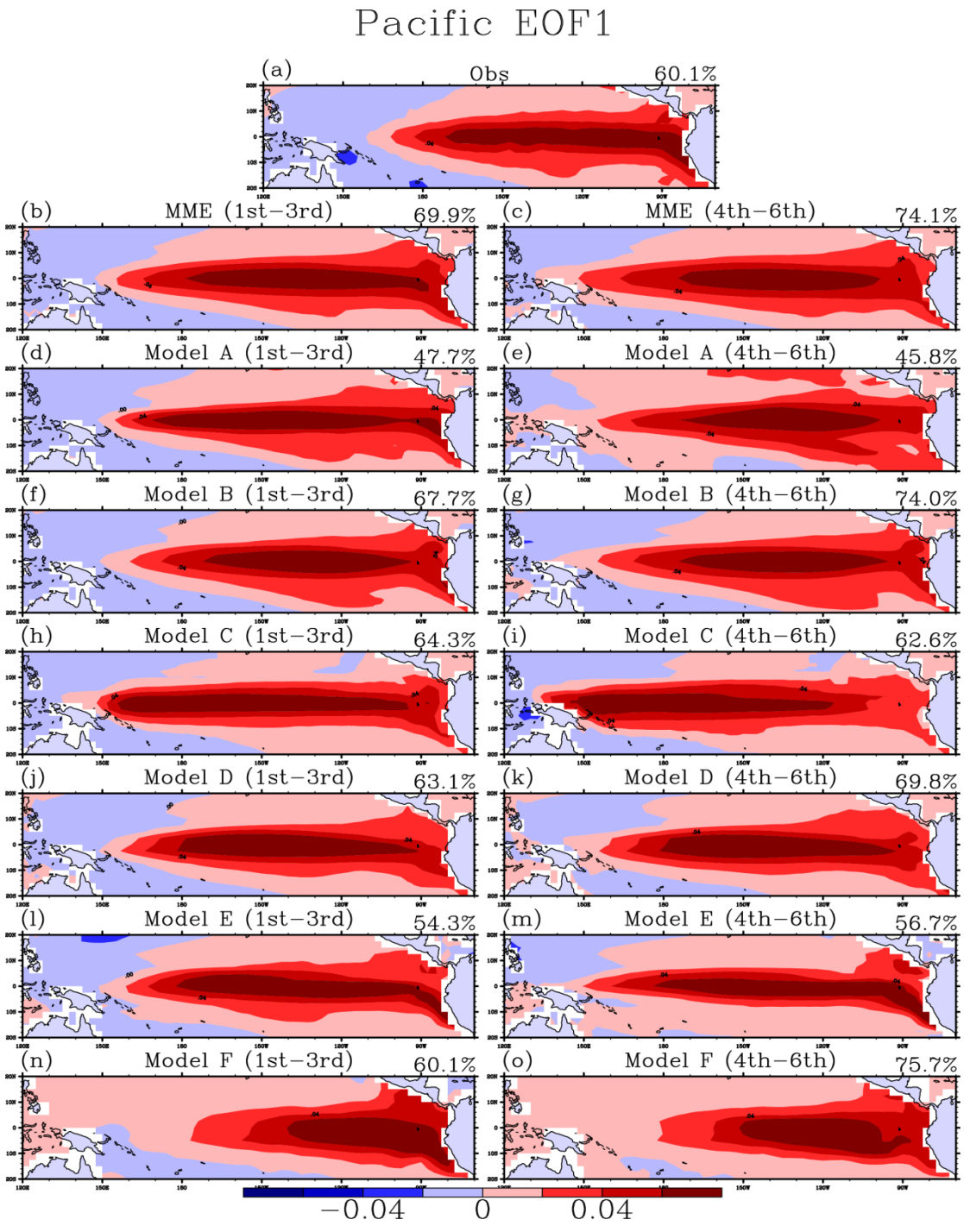

Fig. 3.9 The 1st EOF patterns of SSTA over the Tropical Pacific region [20°S-20°N; 120°E-70°W]. Fractional variance explained by each EOF pattern is given at top right of each panel

Fig.3.10 shows the normalized time series of the Nino3 index (solid) and the principle component of the first EOF for the tropical Pacific [20°S-20°N; 120°E-70°W] SSTA (dotted). It is observed that the two time series are coherent with each other. In fact, the correlation coefficient between the Nino3 Index and the PC1 of Pacific SSTA is 0.988. It denotes that the Nino3 Index is a good indicator to represent the first PCs of the SSTA respectively.

It is also observed some peaks appear during the boreal winter season for certain years in Fig.3.10 for the both time series. Using the standard purposed by Ashok *et al*. (2007), if the normalized Nino3 index excess 1 standard deviation for about 6 months then it can be called a canonical ENSO event. With this standard, 1983, 1987 and 1997 are considered as the canonical ENSO years.

One could observe that the negative phases of the Nino3 Index. Those signals are considered as the La Nina events in 1984, 1988 and 1998. The variability of La Nina is lower than the canonical ENSO and they appear immediately after the disappearance of the canonical ENSO, which is consistent with some previous literature [Jin (1997)].

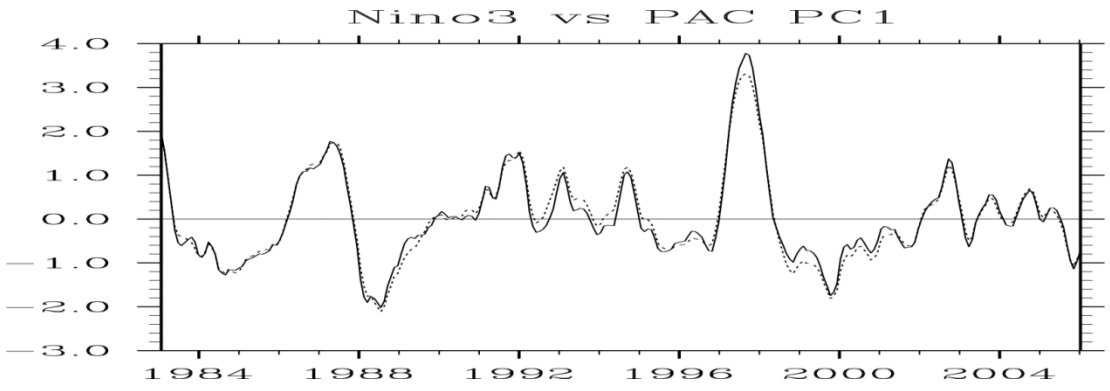

Fig. 3.10 Normalized Nino3 index (solid) and the PC1 of Tropical Pacific [20S-20N; 120E-70W] SSTA (dotted)

For the ENSO Modoki, Fig.3.11 displays the second EOFs of the tropical Pacific SSTA for the observations and APCC models. It is observed that, from the observed EOF2, the warming region is located over the Central Pacific (or the dateline) associated with cooling over the western and eastern Pacific respectively. Indeed, this pattern is referred to the ENSO Modoki [Ashok *et al*. (2007)]. However, the variance contained for the EOF2 is lesser than that of the canonical ENSO. Unlike the case of the canonical ENSO, the modeled variance for the ENSO Modoki are generally lesser than the observed one. This tells us that the models are "less willing" to reproduce the ENSO Modoki than the canonical ENSO.

Another point found in Fig.3.11 is that the models could generally capture the central Pacific warming for 1^{st}-3^{rd} leadtime predictions. However, the upwelling over the eastern Pacific is strengthened and the central Pacific warming is shifted to the west for 4^{th}-6^{th} leadtime predictions. The upwelling is due to the similar cause for the canonical ENSO case which is the too strong zonal easterly background winds in the models. This case is obvious for Model A, Model C and Model E. Remember that the Model A and Model E are with the same atmospheric but different oceanic model component. It denotes that the atmospheric dynamics plays an important role in predicting the position of the central Pacific warming.

It can be concluded that the central Pacific warming patterns for models are more variable than that of the canonical ENSO. As a result, the modeled EOF2 seems tricky to be applied for further analysis.

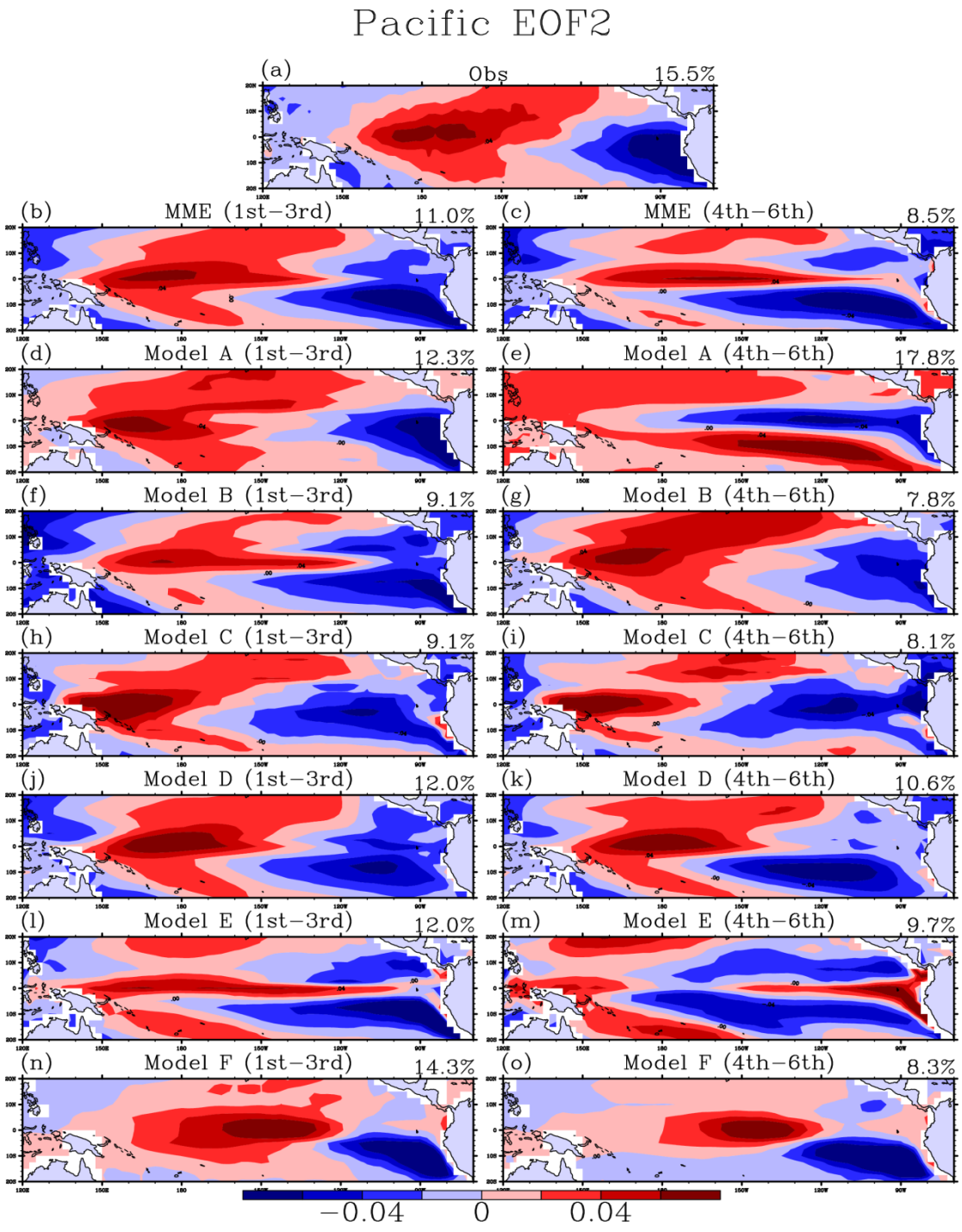

Fig. 3.11 The same as Fig.3.1, except for the 2nd EOF of the tropical Pacific SSTA.

Fig.3.12 displays the normalized time series of the EMI (solid) and the principle component of the second EOF for the tropical Pacific [20°S-20°N; 120°E-70°W] SSTA (dotted). The correlation coefficient between the EMI and PC2 is 0.950. This number is lesser than that between the Nino3 index and PC1, but the EMI and PC2 are still good indicators to each other. Fig.3.It is also observed some peaks appear during the boreal winter season for certain years in Fig.3.10 for the both time series. Using the standard purposed by Ashok *et al*. (2007), if the normalized EMI excess 0.7 standard deviations for about 6 months then it can be called an ENSO Modoki event. With this standard, 1986, 1990, 1991, 1994, 2002 and 2004 are the considered as Modoki years. Similar to the canonical ENSO, there are also negative signals for the ENSO Modoki. It is observed that negative signal for Modoki is even larger than that of the canonical ENSO. However, those events appear in 1983, 1988/1989 and 1998 which are the same as the La Nina signal in Fig.3.10. This leads us to another question: does ENSO asymmetry exist in both canonical ENSO and ENSO Modoki respectively? This question will be assessed in the next section.

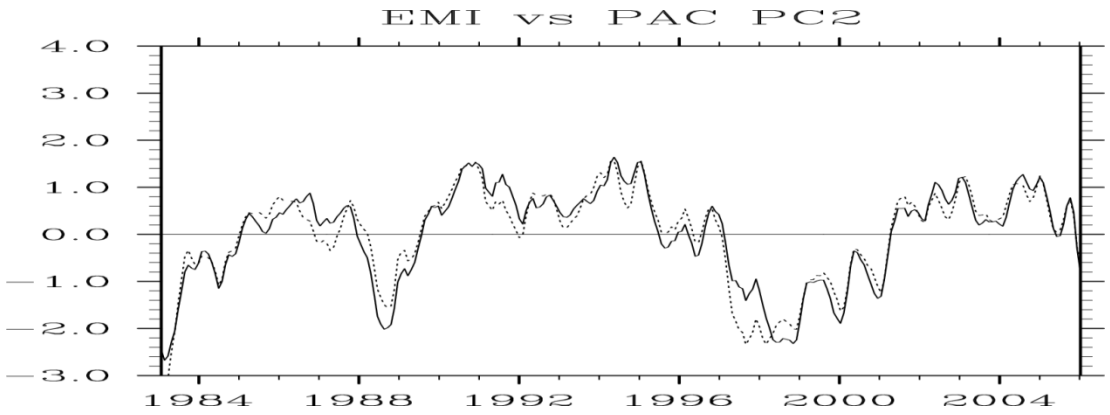

Fig. 3.12 Normalized EMI (solid) and the PC2 of Tropical Pacific [20S-20N; 120E-70W] SSTA (dotted)

Accessing the EOF analysis for the GCMs above, one should find that the behaviors of the modeled EOFs are quite different from each other. Using those EOFs to do analysis could be confusing and the results are hard to be compared. Therefore, unifying the use of EOFs is a must before doing the further work. Besides accessing their skill in predicting the ENSO SST indices and the Principle Components (PCs), here we introduce a statistical method to test whether the two ENSO flavors are "well-resolved" in models. This can be done by first projecting model monthly SSTA onto the first and second empirical orthogonal functions (EOF) of the observed SSTA. These two EOF patterns, computed based on observations over the Pacific within 20°S to 20°N, are shown in Fig.3.9a and Fig.3.11a respectively. For each model dataset, this results in two monthly time series of projection coefficients (hereinafter called PjC1 and PjC2, for projections onto the first and second EOF, respectively).

After identifying the patterns of the two flavors of ENSO, we are now moving on to investigate the ENSO cycle by using the annual mean absolute ENSO indices, principle component of the two leading EOFs of the tropical Pacific SSTA (PC) and the projection coefficients (PjCs). The results are shown in Fig.3.13-Fig.3.14. For the Nino3 Index and PC1 in Fig.3.13, it shows that the canonical ENSO has an obvious cycle that peaks in December (or DJF season) and decays in the coming boreal spring and summer (Fig.3.13). One can observes that the 1st-3rd leadtime predictions of the models could capture the canonical ENSO cycle well like the MME, Model A, Model B, Model D and Model E, but it is not the case for the 4th-6th leadtime predictions.

Fig.3.14 is the same as Fig.3.13 except that the projection coefficients are used to replace the principle component. The cycle obtained from the PjC is similar to the PC.

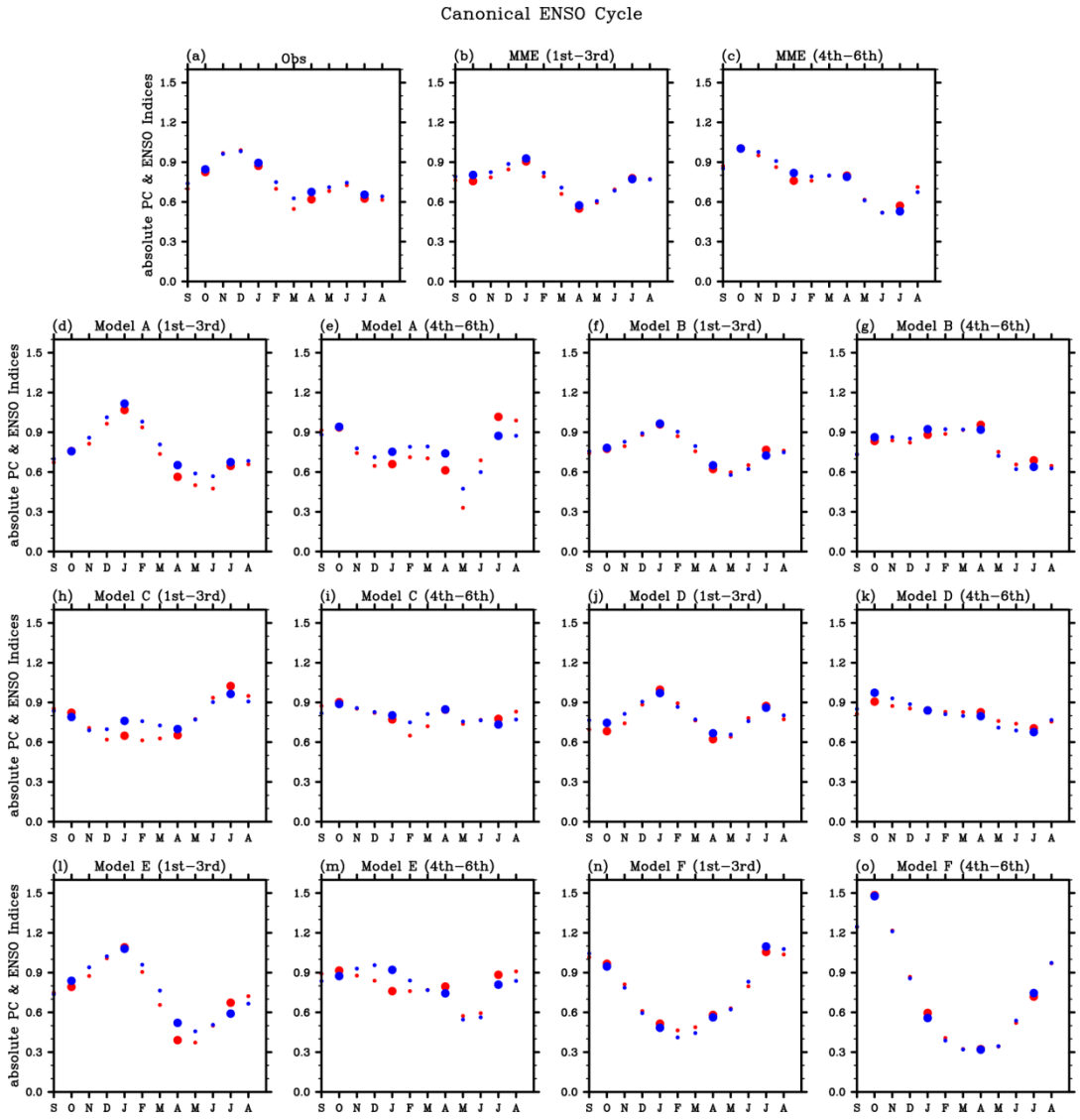

Fig. 3.13 The canonical ENSO cycle calculated from Nino3 Index (red dots) and PC1 of the tropical Pacific SSTA (blue dots). Large dots indicate the four seasons (i.e. SON, DJF, MAM and JJA).

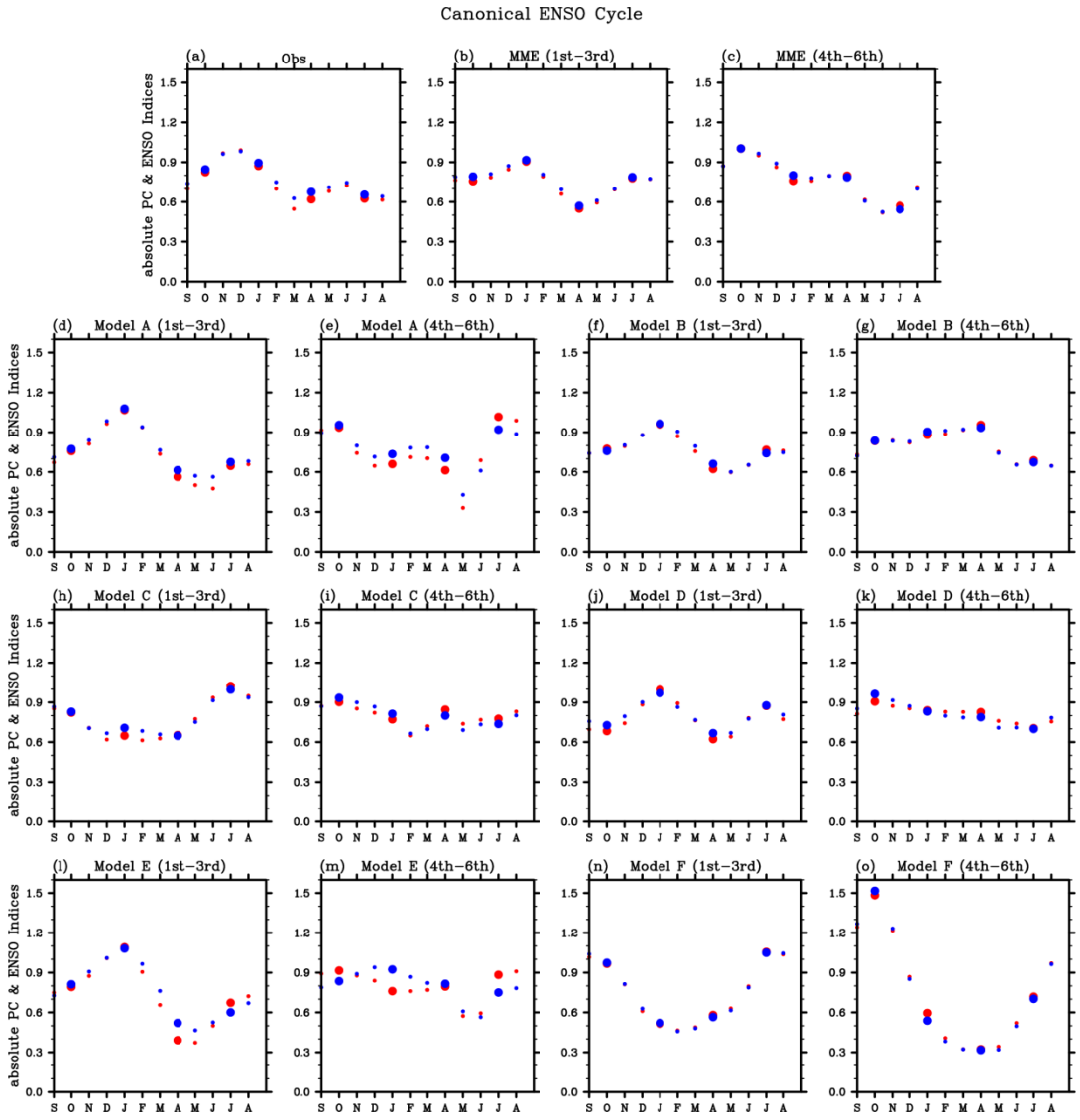

Fig. 3.14 The canonical ENSO cycle calculated from Nino3 Index (red dots) and the first Projection Coefficients (PjC1) of the tropical Pacific SSTA (blue dots). Large dots indicate the four seasons (i.e. SON, DJF, MAM and JJA).

Fig.3.15 summarizes the results from Fig.3.13 and Fig.3.14 by counting the number of canonical ENSO peak months captured by the models. For the observations, the peak month of the canonical ENSO is in December. However, it is found that there is a tendency for the canonical to peak in October and January in the models. The possible explanation is that the models tend to either develop or decay the canonical ENSO earlier for about one to two months. It is also noticed that both the PC and PjC methods could give similar predictions to the peak month of the canonical ENSO events. This indicates that the Nino3 Index and the PC1 are good representative to each other.

Fig.3.16 displays the count of the number of canonical ENSO peak seasons captured by the models. As seen in Fig.3.13 and Fig.3.14 the peak season of the canonical ENSO is in DJF. However, the dual peaks still exist for both SON and DJF season.

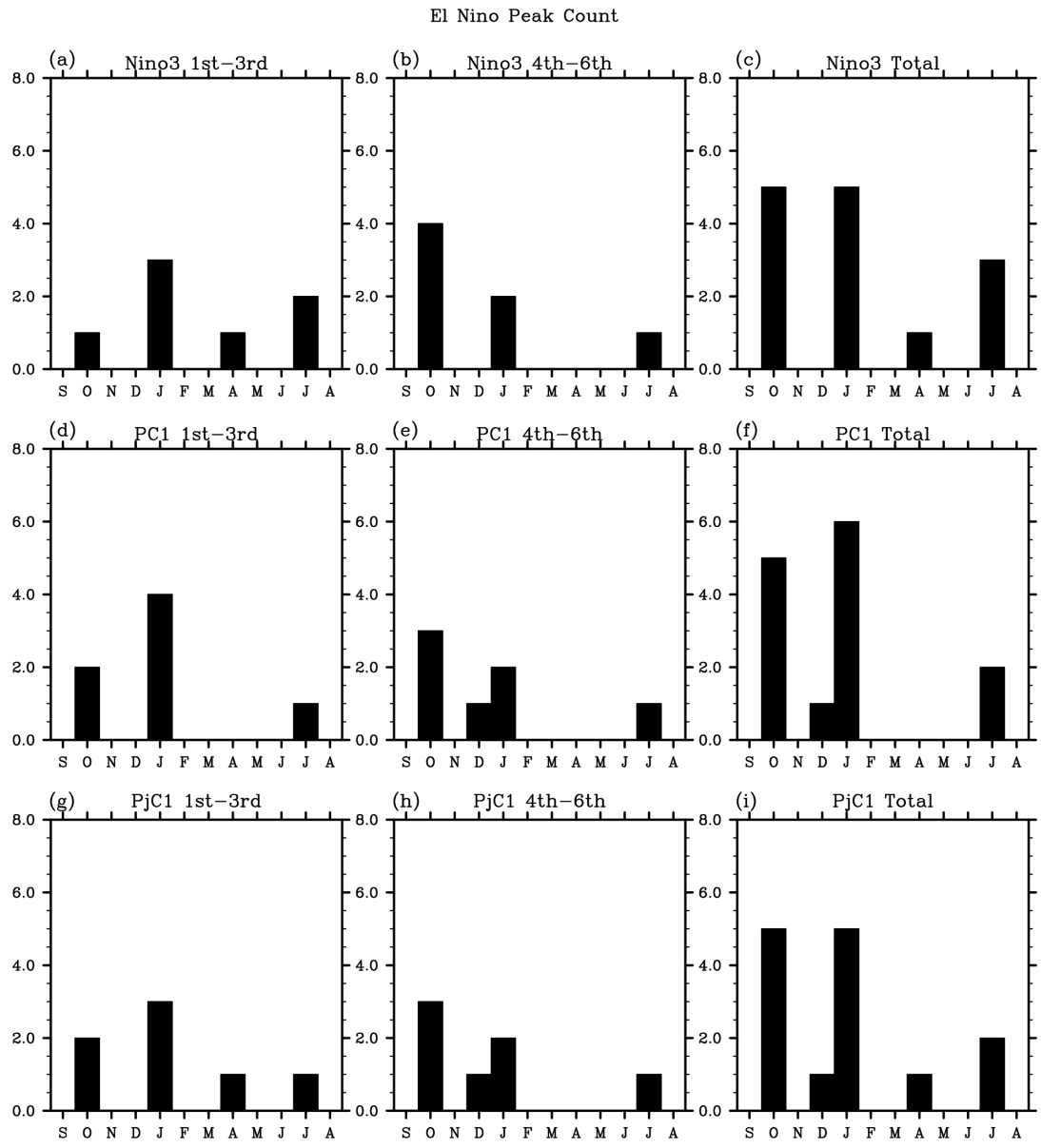

Fig. 3.15 Peak month count for the canonical ENSO for 1st-3rd leadtime (left column), 4th-6th leadtime (center column) and the total count (right column) and the count using Nino3 Index (top row), PC1 of the tropical Pacific SSTA (middle row) and the Projection Coefficients (PjC1; bottom row)

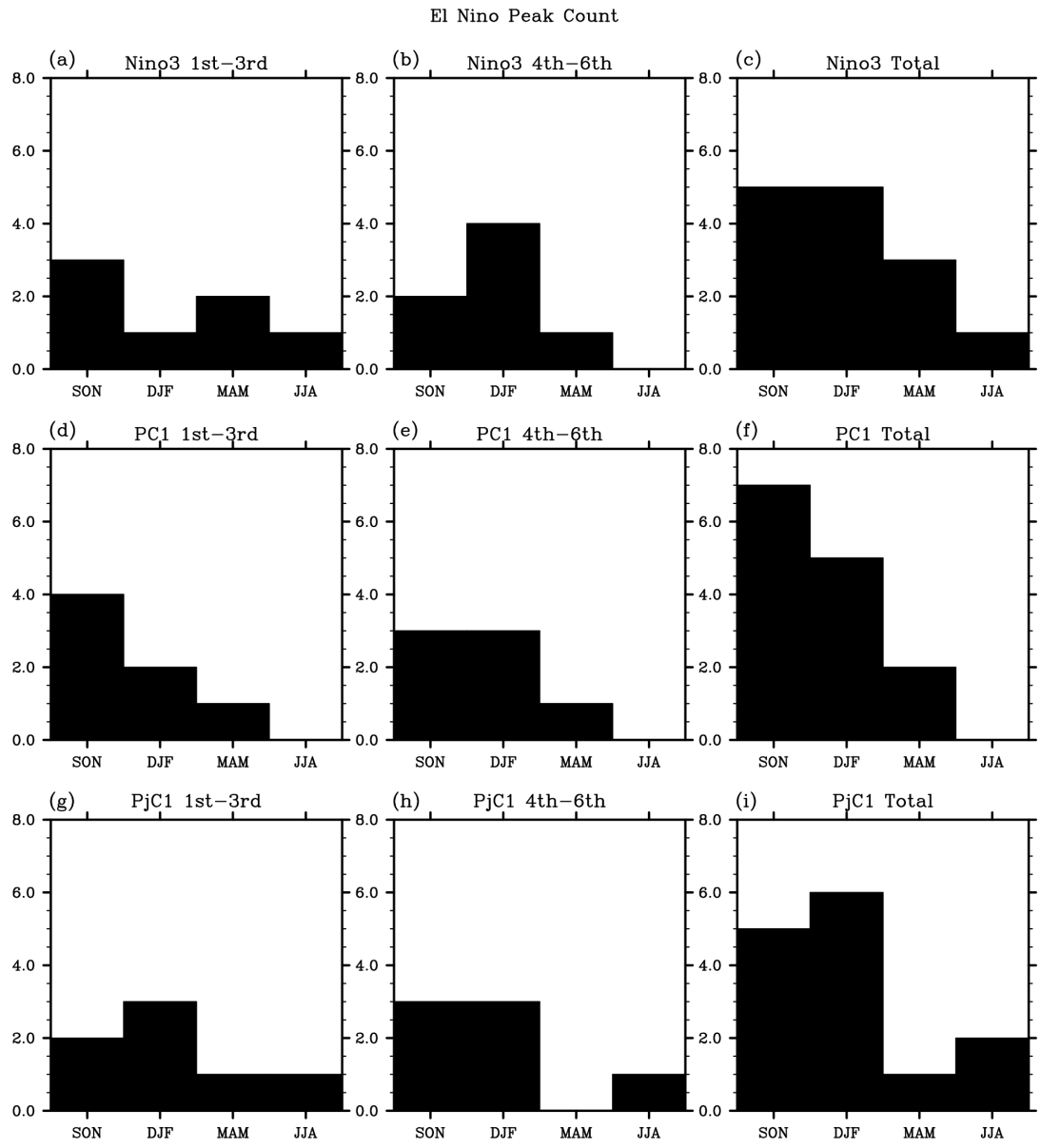

Fig. 3.16 Peak season count for the canonical ENSO for 1st-3rd leadtime (left column), 4th-6th leadtime (center column) and the total count (right column) and the count using Nino3 Index (top row), PC1 of the tropical Pacific SSTA (middle row) and the Projection Coefficients (PjC1; bottom row)

Fig.3.17 and Fig.3.18 display the ENSO Modoki cycle using the EMI, PC2 and PjC2 respectively. It is seen that the peak month of the Modoki is in January. The peak season is in DJF. However, the cycle of ENSO Modoki is not obvious compared with the canonical ENSO. It denotes that the ENSO Modoki tends to persist the warming signal during its cycle. It is also noticed that the Modoki cycle predicted by the PjC2 for the Pacific SSTA is more relevant to that predicted by the EMI than the PC2.

Fig.3.19 summarizes the results from Fig.3.17 and Fig.3.18 by counting the number of ENSO peak Modoki months captured by the models. For the observations, the peak month of the canonical ENSO is in January. However, another peak is also found in October using the EMI. It is also noticed that the PjC2 is the best to predict the ENSO Modoki cycle with a singal peak in October.

Fig.3.20 displays the count of the number of canonical ENSO peak seasons captured by the models. As seen in Fig.3.17 and Fig.3.18 the peak season of the canonical ENSO is in DJF. The PjC2 is a better indicator to express the ENSO Modoki cycle because the phase and amplitude of PjC2 are both relevant to the modeled EMI. For example, the PC2 and EMI of the MME, Model A, Model B, Model E and 1^{st}-3^{rd} leadtime predictions of Model C are all out of phase (see Fig.3.17). However, this situation cannot be found in PjC2 versus EMI plots (see Fig.3.18).

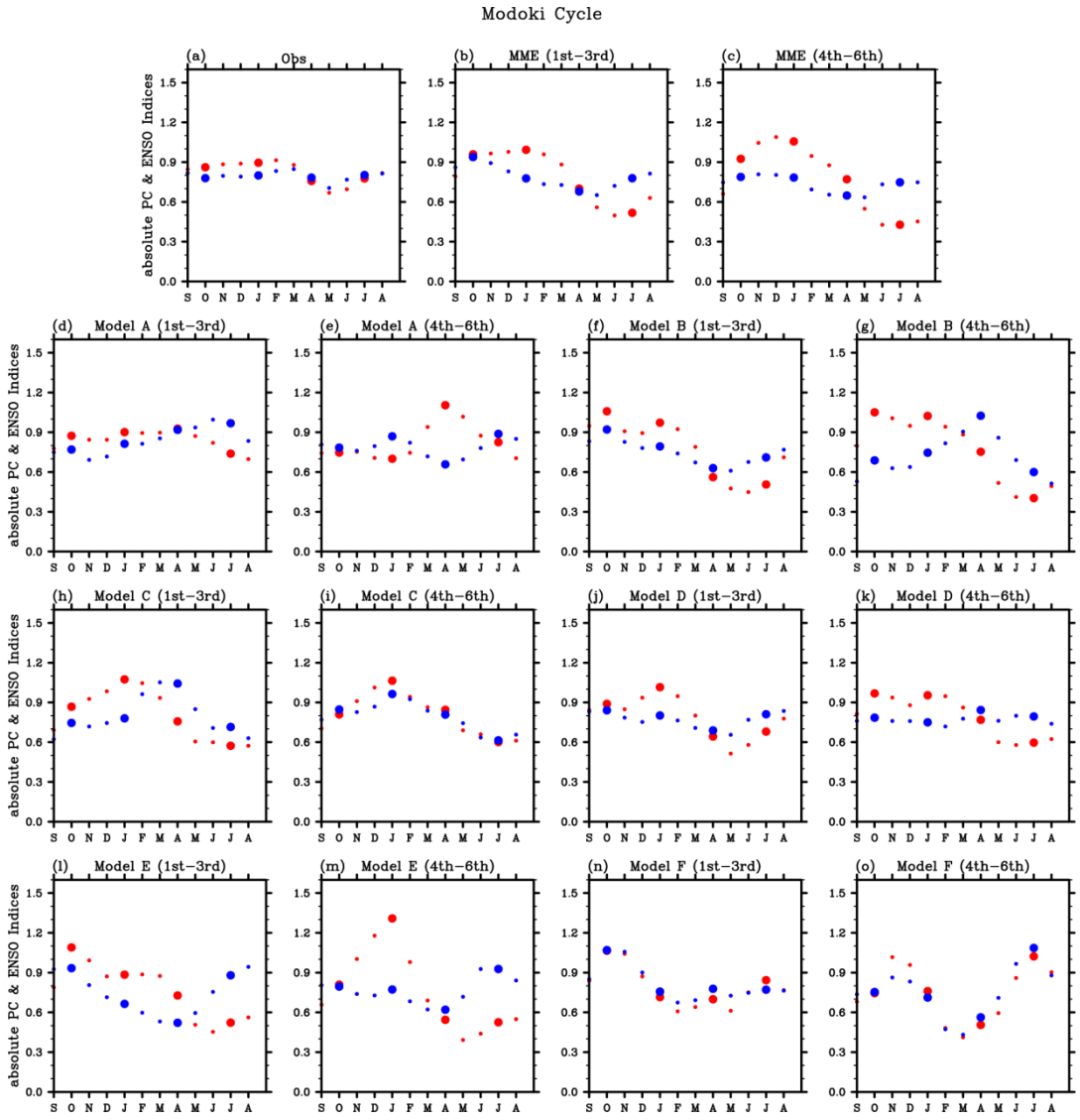

Fig. 3.17 The ENSO Modoki cycle calculated from EMI (red dots) and PC2 of the tropical Pacific SSTA (blue dots). Large dots indicate the four seasons (i.e. SON, DJF, MAM and JJA).

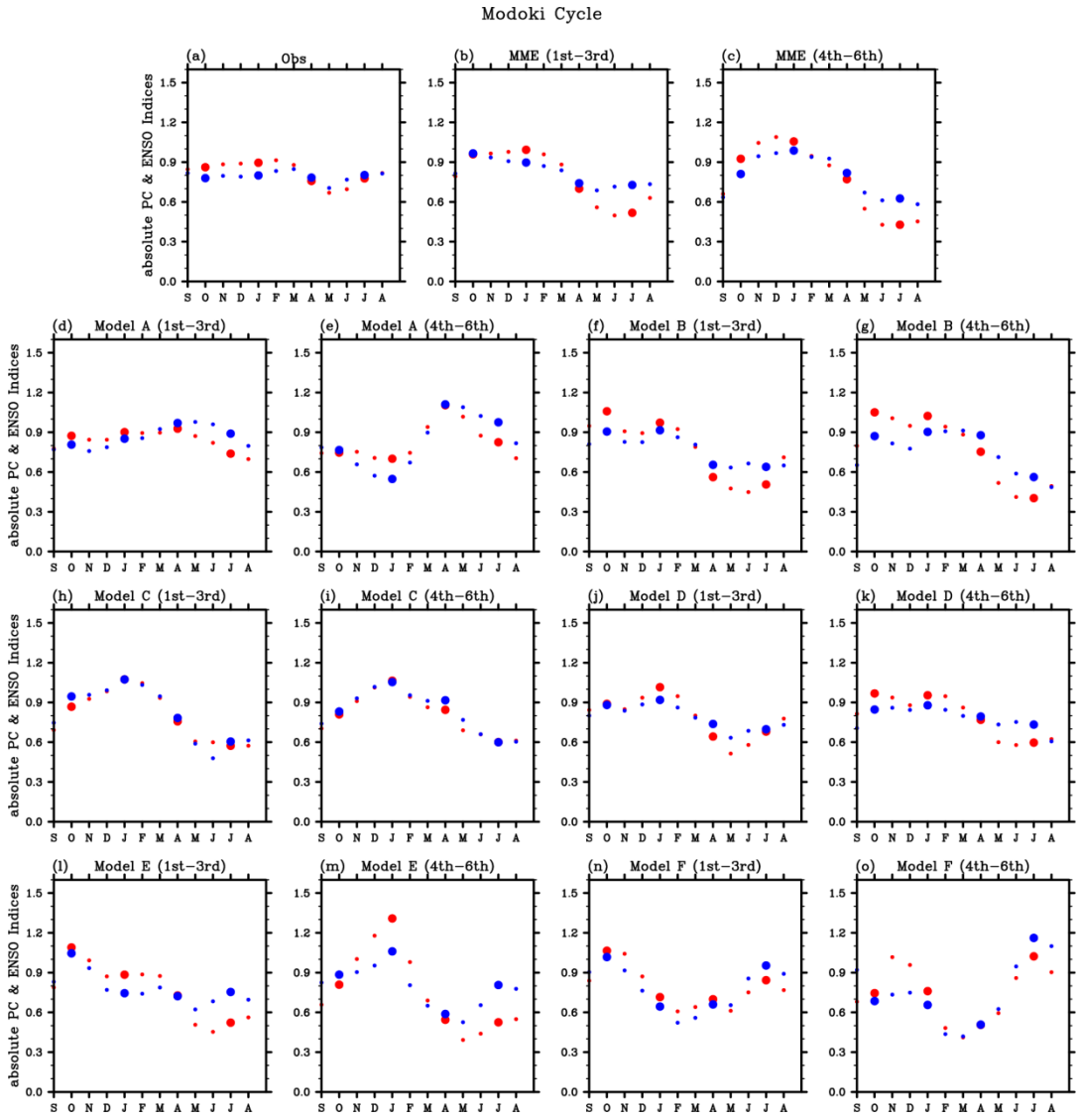

Fig. 3.18 The ENSO Modoki cycle calculated from EMI (red dots) and the secnod Projection Coefficients (PjC2) of the tropical Pacific SSTA (blue dots). Large dots indicate the four seasons (i.e. SON, DJF, MAM and JJA).

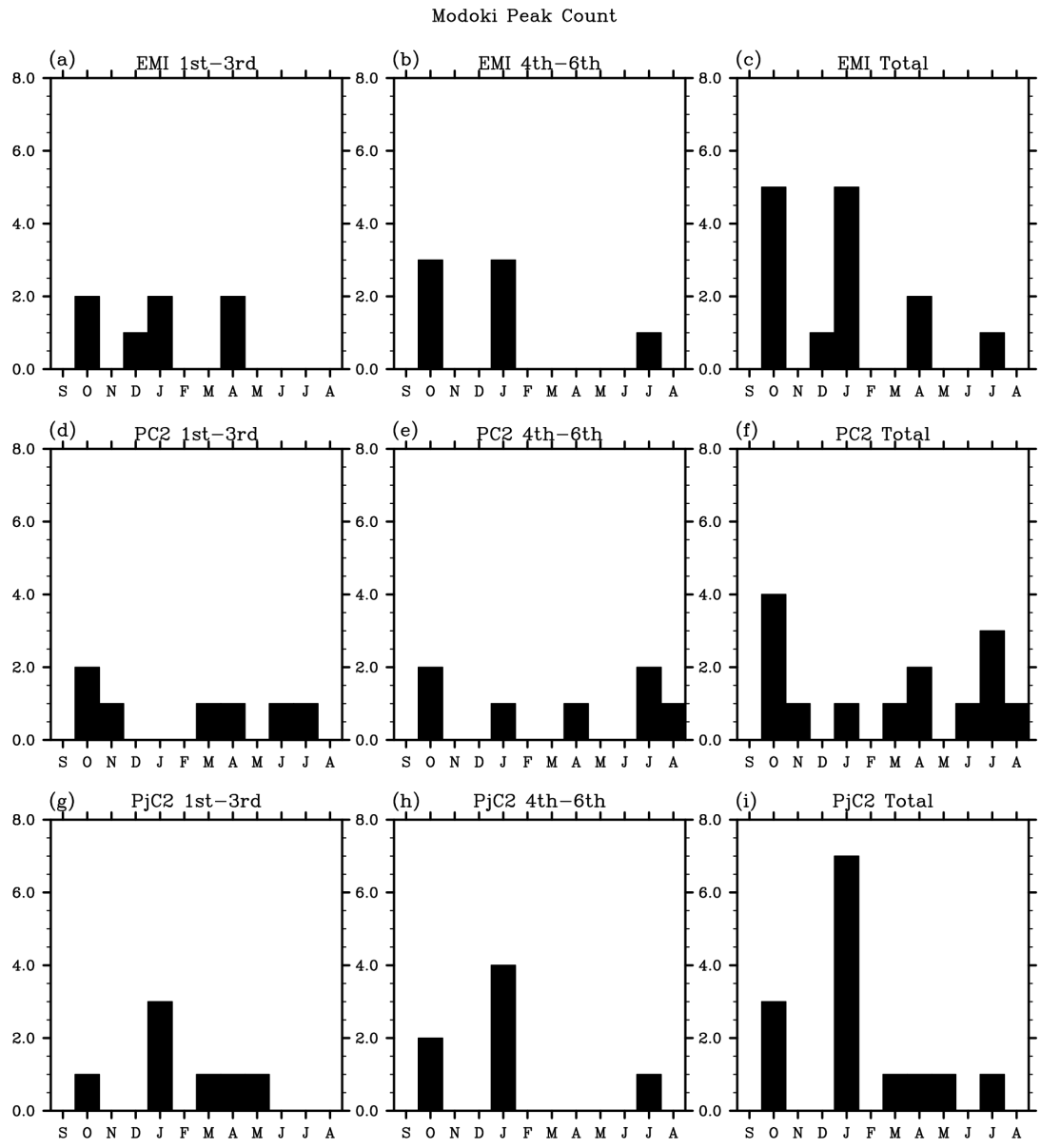

Fig. 3.19 Peak month count for the ENSO Modoki for 1st-3rd leadtime (left column), 4th-6th leadtime (center column) and the total count (right column) and the count using EMI (top row), PC2 of the tropical Pacific SSTA (middle row) and the Projection Coefficients (PjC2; bottom row)

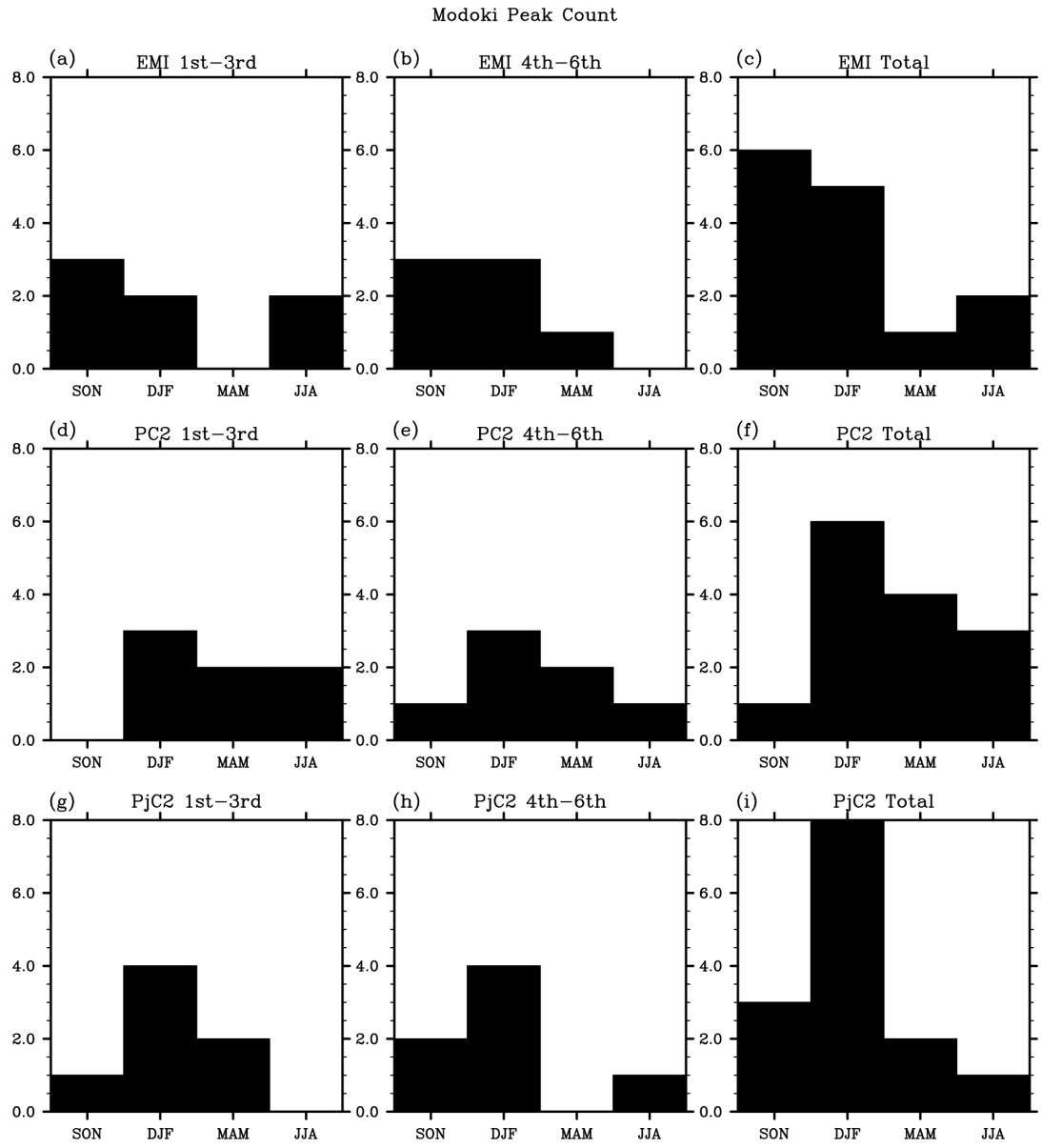

Fig. 3.20 Peak season count for the ENSO Modoki for 1st-3rd leadtime (left column), 4th-6th leadtime (center column) and the total count (right column) and the count using EMI (top row), PC2 of the tropical Pacific SSTA (middle row) and the Projection Coefficients (PjC2; bottom row)

It is concluded that the model mean could give satisfactory results in predicting the EOF patterns. However, the individual performance in predicting the SSTA EOF patterns is quite different. Therefore, when doing the principle component analysis with the SSTA EOFs, the projection coefficients will be adopted instead to make the EOF pattern used in the projection of PC coherent. This concept will be applied to analyze the mixing of the two flavors of ENSO in the later section in this chapter.

3.4 ENSO Skills in CGCMs

We now assess the skill of coupled models in predicting the SST indices associated with the two types of ENSO. In particular, correlation coefficients between observed and model predicted monthly SST indices were calculated, for the DJFMAM and MAMJJA prediction cycles. Results are given in Fig.3.21. Most models give relatively good predictions of the Nino3 index during the DJF season with correlation reaching 0.9 or even higher (see Fig.3.21a). However, there is an obvious decrease of models' skill starting from March. For the 6-month-lead predictions of the Nino3 index, their correlation with observations now ranges from 0.5 to about 0.7. For predictions covering the MAMJJA period, it can be seen that models' skill exhibits a more continuous decay in time. Overall, the MME mean and model D perform best in predicting the Nino3 index. For the forecast runs initiated in February (i.e. those covering the MAMJJA cycle), the skill of models A and E decays drastically (see Fig.3.21b). This can be related to the fact that canonical ENSO SSTA signals are relatively less persistent in these two models.

Models' skills in predicting EMI were also examined; they suggest that ENSO Modoki events are more difficult to predict than conventional ENSO, especially in boreal spring to summer. It can be seen that model C gives particularly poor EMI predictions, compared to other individual models. The MME mean gives the best forecast of EMI in the DJFMAM period. However, in the MAMJJA season, the MME average is less skillful than two other models. This is probably due to the poor skill of model C which dramatically degrades the performance of the MME. In fact, if model C is not included in the averaging process, then the MME mean still gives the best EMI predictions in this. Among all individual models, model D also performs well in capturing fluctuations in EMI. The skill drop through the boreal spring season can also be explained by the Spring Predictability Barrier [SPB; Kirtman *et al*. (2002), Lau and Yang (1996), McPhaden (2003), Webster and Yang

(1992); Wu *et al*. (2008)]. SPB describes the phenomenon of the skill drop of climate models makes predictions from or through the boreal spring season. One of the explanations of SPB is that the seasonal anomaly in spring is small; therefore, the noise of initial condition becomes large for the predictions.

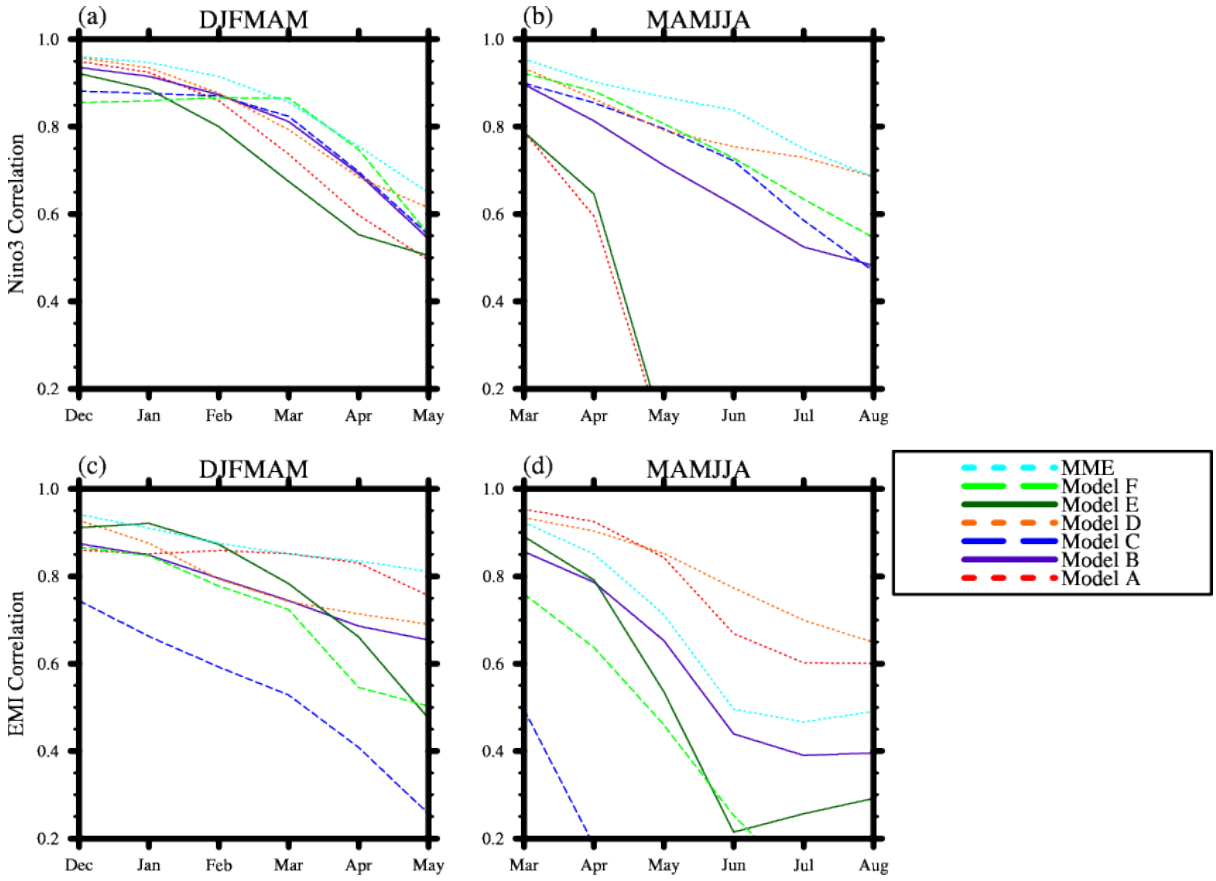

Fig. 3.21 Correlation coefficients between observed and model-predicted monthly mean (a, b) Nino3 index and (c, d) EMI, for (a, c) DJFMAM and (b, d) MAMJJA prediction cycles.

The Taylor diagrams of the *El Niño* Indices calculated from APCC model predictions with the observations as reference are shown in Fig.3.22 to reveal model performance of the APCC models. The temporal correlation coefficients are used in the diagrams. For predictions of Nino3 Index (see Fig.3.22a), it is found that the correlation coefficients of models tend to cluster at about 0.75. In fact, the averaged correlation is 0.71. The averaged correlation coefficients for 1^{st}-3^{rd} and 4^{th}-6^{th} month lead predictions are 0.81 and 0.62 respectively. One possible reason for the drop of Nino3 index skills from shorter to longer leadtime is that the models tend to decay canonical *El Niño* quicker than the observations. The MME average and Model D have the highest correlation coefficients and the lowest Root Mean Square Error (RMSE) of Nino3 Index predictions for 1^{st}-3^{rd} and 4^{th}-6^{th} month leadtime (0.89 and 0.86 respectively). Nevertheless, the MME average cannot simulate canonical *El Niño* amplitude well compared with Model D. Therefore, it is said that Model D can reproduce the best skills of phase and amplitude predictions of canonical *El Niño* with smallest error. Model A and Model E have the poorest correlation coefficients and amplitude skills among the APCC models. This situation holds for 1^{st}-3^{rd} and 4^{th}-6^{th} leadtime predictions at the same time.

For predictions of EMI (see Fig.3.22b), it is found that the correlation coefficients tend to cluster at about 0.7. The averaged correlation coefficient of the APCC models is 0.65. The averaged correlation coefficients for 1^{st}-3^{rd} and 4^{th}-6^{th} month lead predictions are 0.72 and 0.57 respectively. The skill is lesser than the Nino3 index. Nonetheless, Model C seems to have extremely low skill among the models. Indeed, if Model C is removed from the calculation, the averaged correlation coefficient of EMI is comparable to the Nino3 index. However, it is observed that APCC models tend to underestimate the amplitude of EMI. This can be attributed to the inability of models to persist *El Niño* Modoki in the decaying summer season. It is also seen that the MME average and Model D, again, have the highest skills of correlation coefficients for 1^{st}-3^{rd} and 4^{th}-6^{th} month

leadtime and the skill of predicted amplitude of EMI is still the highest. Therefore, Model D is the best model to predict the phase and amplitude of canonical *El Niño* and *El Niño* Modoki.

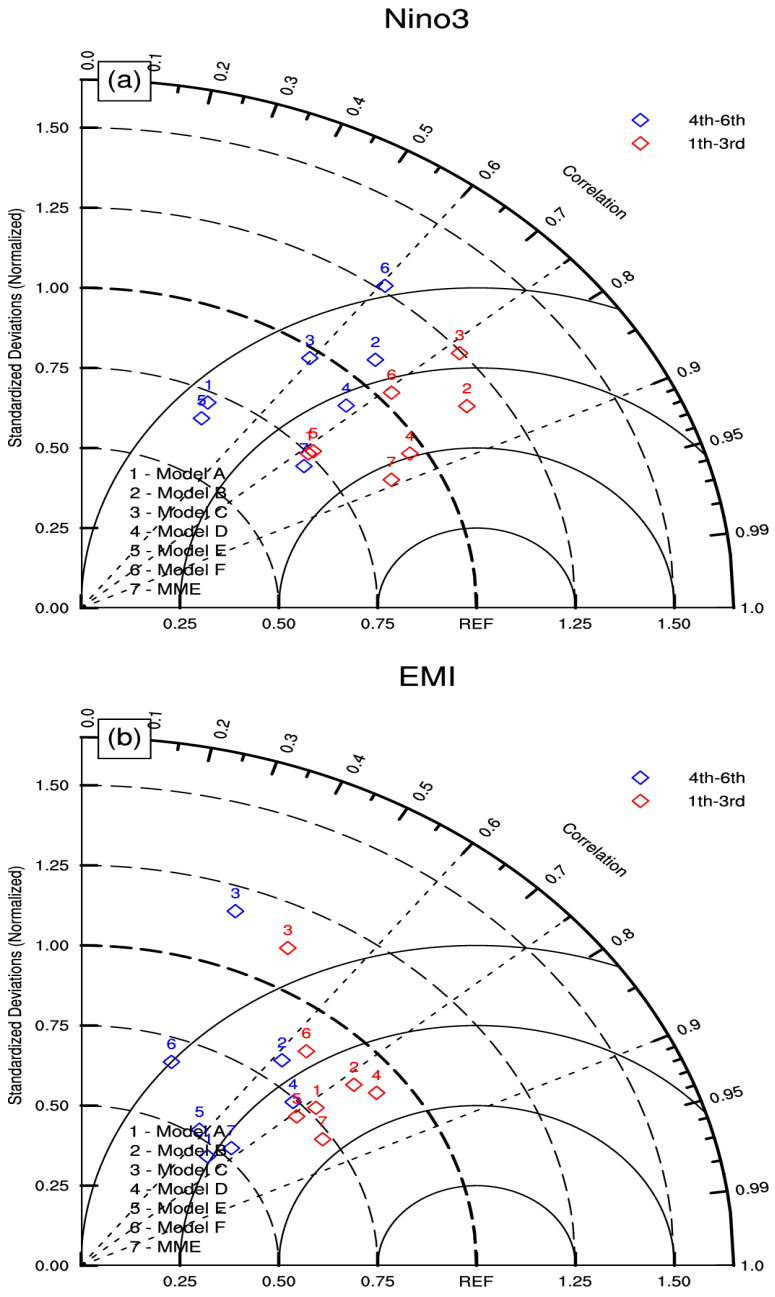

Fig. 3.22 Taylor Diagrams for simulated a) Nino3 Index and b) EMI with the observations as reference point

3.5 Mixings of El Niño in CGCMs

It is also instructive to see whether coupled models can differentiate well the two types of ENSO. Therefore, the projection coefficients (PjC) mentioned in section 3.3 is adopted to do the analysis. Note that if observational data are used instead of those from models, PjC1 and PjC2 equal the principal components (PC) corresponding to the observed EOFs (i.e. PC1 and PC2) respectively. By construction, PC1 and PC2 are uncorrelated. On the other hand, for any model dataset, in general the correlation between PjC1 and PjC2 is non-zero. Thus, their correlation can be used as a metric to measure the degree of mixing between ENSO and ENSO Modoki SST signals in models. For example, if canonical ENSO SST signals given by a particular model tend to have their peak amplitude shifted towards the central Pacific, then during conventional ENSO events, its predicted SSTA will also project strongly onto the observed EOF2, besides projecting onto EOF1. Thus, one expects positive correlation between PjC1 and PjC2 in this model. If, however, the ENSO and ENSO Modoki SSTA are well simulated, then the correlation between PjC1 and PjC2 is expected to be small, as in observations (with correlation identically equal to zero). To summarize, correlation between the projection coefficients can be used to quantify the degree of mixing between SSTA patterns associated with the two types of ENSO as seen in the coupled model hindcast simulations.

Figs.3.23b to 3.23h show the scatter plots of the two projection coefficients (PjC1 and PjC2) for the APCC models with the principal components (PC1 and PC2) for the observations (Fig.3.23a). For the observations (Fig.3.23a), it can be seen that when the value of PC1 is large positive, the value of PC2 tends to be large negative. It can be interpreted that there is a projection of canonical ENSO to the negative ENSO Modoki events. This is probably because SSTA over the eastern Pacific for canonical El Niño events is strong during its peak and decay period. This strong SSTA will in turn make the EMI value more negative. It is also found that events with small magnitudes

of PC1 and PC2 tend to cluster around the origin; this suggests that, for small magnitude events, PC1 and PC2 are positively correlated. It is also noteworthy that when PC1 is strong and negative, PC2 also tends to assume negative values. This result is relevant to some recent studies showing that La Nina and La Nina Modoki events could be mixed. Model D seems to be the best model in differentiating the two types of ENSO for 1-3 and 4-6 month-lead predictions. Its distribution of projection coefficients is very similar to that from observations. In other words, ENSO and ENSO Modoki events are well resolved in this model. Also, the mixing of negative PjC1 and PjC2 are captured. For the MME mean, its 1-to-3 month-lead predictions also gives a pattern similar to observations; however, it is not the case for 4-to-6 month-lead predictions. Models A and E give evenly distributed projection patterns, while model C gives obvious positive correlation between PjC1 and PjC2. This indicates that, during canonical ENSO, SSTA from model C would tend to exhibit ENSO-Modoki-like features, and vice versa. For model F, there is a negative correlation, implying that strong El Niño related SSTA also projects onto a La Nina Modoki-like pattern in the model environment (Fig.3.23h).

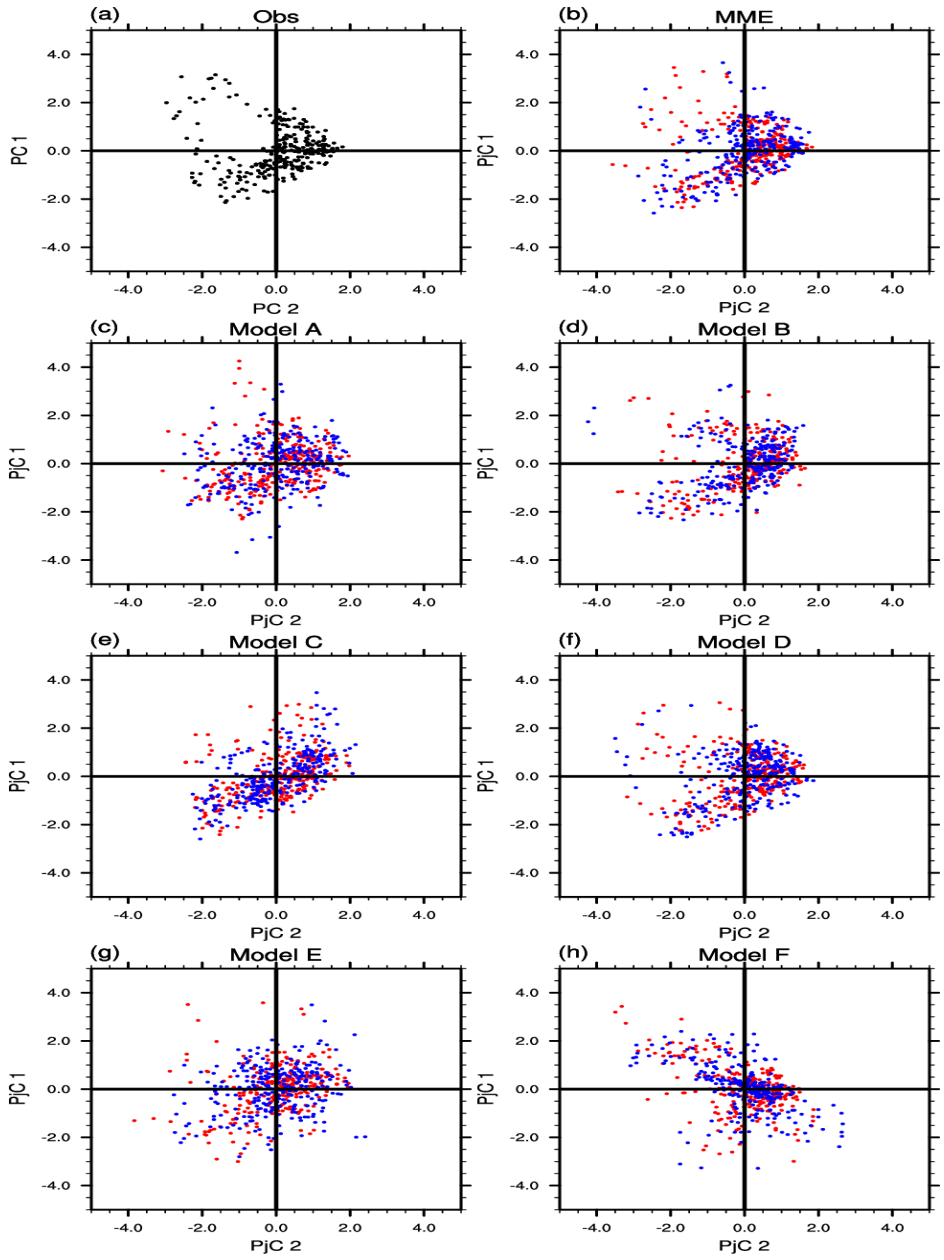

Fig. 3.23 Scatter plots for (b-h) monthly SSTA projections onto the observed 1st and 2nd EOF (denoted by PjC1 and PjC2, respectively) for 1-to-3 (red) and 4-to-6 (blue) month-lead predictions from individual models as well as their MME average. (a) Same projections but using observed SSTA. See text for details.

Table.3.1 gives the correlation coefficients between the projection coefficients PjC1 and PjC2 in Fig.4. It is found that model D has low degree of mixing for 1-3 and 4-6 month-lead. It denotes that model D could differentiate the two types of ENSO well. The degree of mixing for MME predictions is low for 1-3 month-lead. However, it increases significantly in 4-6 month-lead predictions. The possible reason is that the increase of strong La Nina events projection on the negative ENSO Modoki events. Model C has a large positive degree of mixing. One could expect that model C would give canonical-ENSO-like signal when predicting ENSO Modoki events.

Table.3.1 Correlation coefficients between PjC1 and PjC2

	Model A	Model B	Model C	Model D	Model E	Model F	MME
1-to-3 month lead	0.147	0.156	0.312	0.135	0.218	-0.568	0.090
4-to-6 month lead	0.135	0.191	0.593	0.132	0.165	-0.629	0.268

3.6 Evolution and persistence of ENSO

For the decaying phase of ENSO, persistence of equatorial Pacific SST signals was first assessed before examining their skill in ENSO prediction. Fig.3.24 shows the auto-correlation function of ENSO and ENSO Modoki indices computed based on observations and model simulations covering the whole data period. Notice that model hindcast data were stratified into those with 1 to 3 months, and those with 4 to 6 months of forecast leadtime (see Chapter 2). It is noteworthy that, from observations (black line), the auto-correlation for the monthly Nino3 index decays more rapidly than its counterpart for EMI. In fact, the auto-correlation function drops by a value of 0.6 for the Nino3 index, while the decrease for EMI is only about 0.35 during the same 6-month period (see Fig.3.24). The fact that ENSO Modoki appears to be more persistent than canonical ENSO is consistent with a number of observational studies. Examining the persistence of the two types of ENSO in models (Fig.3.24), it is found that different models can give rather different persistence behavior. For instance in the 1-to-3 month lead predictions, canonical ENSO signals in model C tend to over persist, while those from models A, E and F decay too quickly. The drop of persistence can also be attributed to spring persistence barrier [Wu *et al*. (2008)] stating that the persistence of *El Niño* of climate models (basically all kinds of climate models) experiences a skill drop if the prediction is made from or through the boreal spring season. This finding is also relevant to the finding in the present study. That is, the models actually tend to decay the two types of *El Niño* too quickly in the decaying spring and summer.

Overall, there seems to be no common bias in models' representation of the persistence characteristics of conventional ENSO. However, for ENSO Modoki, it is obvious that models tend to underestimate its persistence (compare Figs.3.24a and 3.24b with Figs.3.24c and 3.24d). It can also be seen that the unrealistic drop of persistence in EMI in even more severe in 4-to-6 month-

lead predictions than those with 1 to 3 months of leadtime. It is clear that coupled models have difficulties in retaining the identities of Modoki signals in the simulated environment.

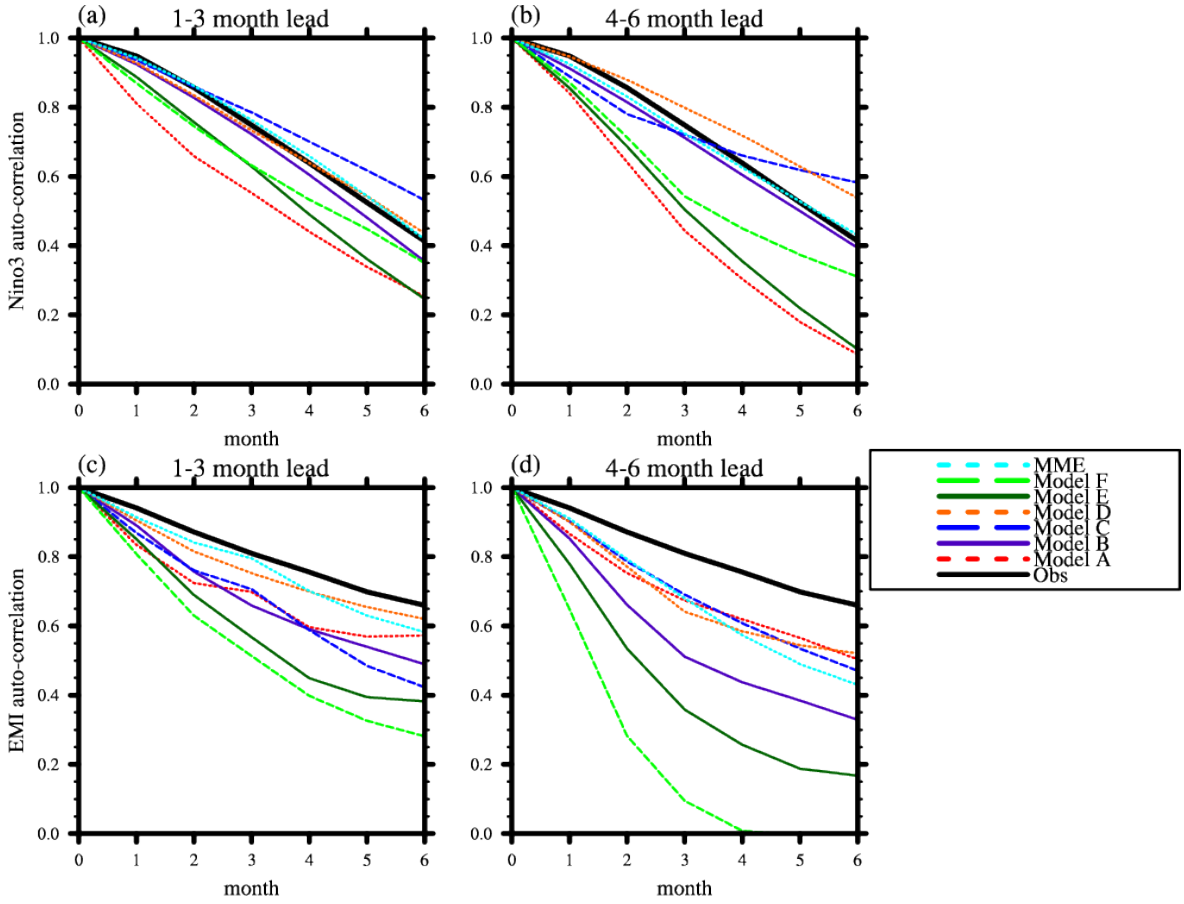

Fig. 3.24 Auto-correlation function for monthly mean (a, b) Nino3 index and (c, d) EMI from (a, c) 1-to-3-month and (b, d) 4-to-6-month lead SST predictions from individual models as well as their MME average. Also shown are the values computed from observed SST.

Inspection of individual model outputs shows that models B and D are the best in capturing the persistence of the Nino3 index. They generally give good performance in their 1-to-3 and 4-to-6 month-lead forecasts. On the other hand, models A, E and F give canonical ENSO signals that decay too rapidly, and this is especially the case in their predictions with long leadtime (see Figs.3.24a and 3.24b).

Model D and the MME are found to be the best model in capturing the persistence of EMI for 1st to 3rd month leadtime (Fig.3.24c). However, as mentioned above, the rest of the models fail to reproduce the strong persistence of ENSO Modoki-like SSTA. For longer leadtime predictions, the skill of is even worst. Even Model D and the MME do not capture the persistence of the EMI (see Fig.3.24d). For one particular model, the auto-correlation of EMI even becomes negative after 4 months. The interesting thing is that the models also tend to underestimate the amplitude of the EMI, especially for longer leadtime (shown in Fig.3.22b). Combining the above two effects, it is interpreted that the underestimation of EMI amplitude can be attributed to the poor prediction of the persistence of the EMI.

After accessing the behaviors of the two types of ENSO statistically, El Niño and El Niño Modoki composites of SSTA evolution over the equatorial Pacific from both observations and model predictions are compared. Fig.3.25 shows the SSTA composites of canonical ENSO events averaged over the equatorial band of 10˚S-10˚N. Observations show a clear decaying pattern in the decay period [MAMJJA(1)] whose SSTA suddenly become negative over the central Pacific in the decaying summer. Model D can predict well the evolution of cold SSTA over the central-western Pacific. The above two points are relevant to the results of the auto-correlation of Nino3 index.

Models A and E show positive SSTA signals which decay too quickly and become negative in eastern Pacific. This is consistent with their rapid decay of auto-correlation of the Nino3 index as lag time increases (Fig.3.25).

It is observed that the SSTA warming of model C shifts from the eastern Pacific to the central Pacific in 4 to 6 month predictions for the canonical ENSO predictions (Fig.3.25). It is the reason that model C gives high degree of mixings of the projection coefficients for 4-6 month-lead predictions. That is, model C gives central Pacific warming signal when predicting the canonical ENSO.

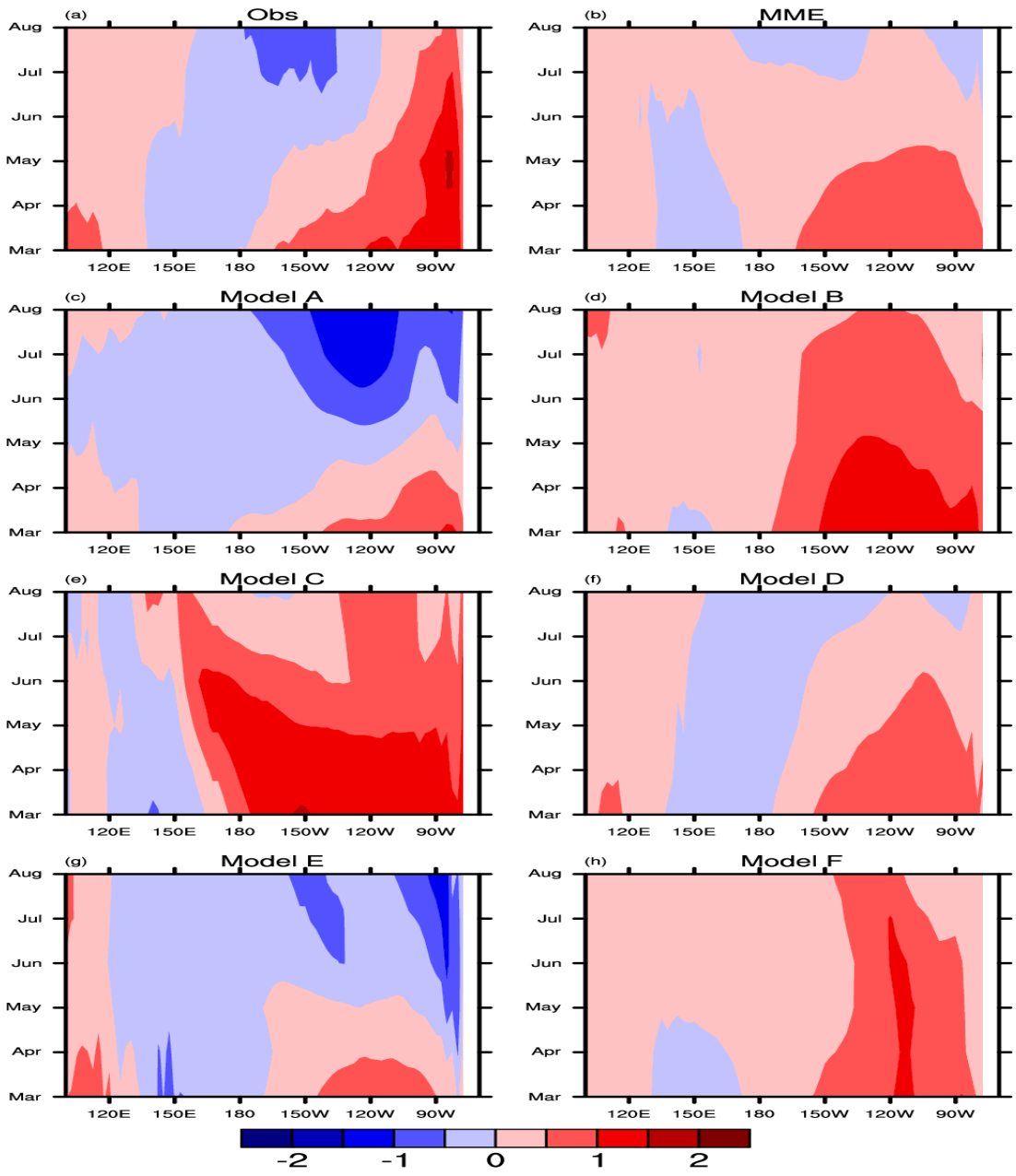

Fig. 3.25 Composite SSTA after the peak of canonical El Niño events in the MAMJJA season of 1983, 1988 and 1998, from (a) observations, (b) Model A, (c) Model B, (d) Model C, (e) Model D, (f) Model E, (g) Model F, (h) MME mean, averaged over 10°S-10°N. See scale bar at bottom (units: °C).

For El Niño Modoki SSTA composites during its decaying phase (Fig.3.26), observations shows anomalously warm signals located in the central Pacific which tends to persist from boreal spring to summer. Model D could capture well this persistent SST feature; this is consistent with the fact that the auto-correlation for EMI is also high in this model. The rest of the models perform poorly compared to model D; they generally give El Niño Modoki which decays too fast in their 4-to-6 month-lead predictions. This is probably the reason why these models have less persistent ENSO Modoki in the simulated environment. Model F exhibits warm SSTA signals that are confined over the far eastern Pacific during typical El Niño Modoki episodes. Overly strong warming over the far eastern equatorial Pacific should lead to positive projection onto the first EOF from observations, but also negative projection onto the second EOF (see Fig.3.23). This results in positive PjC1 and negative PjC2 whenever El Niño Modoki occurs. Therefore, the two ENSO flavors are negatively correlated in model F (Fig.3.23h).

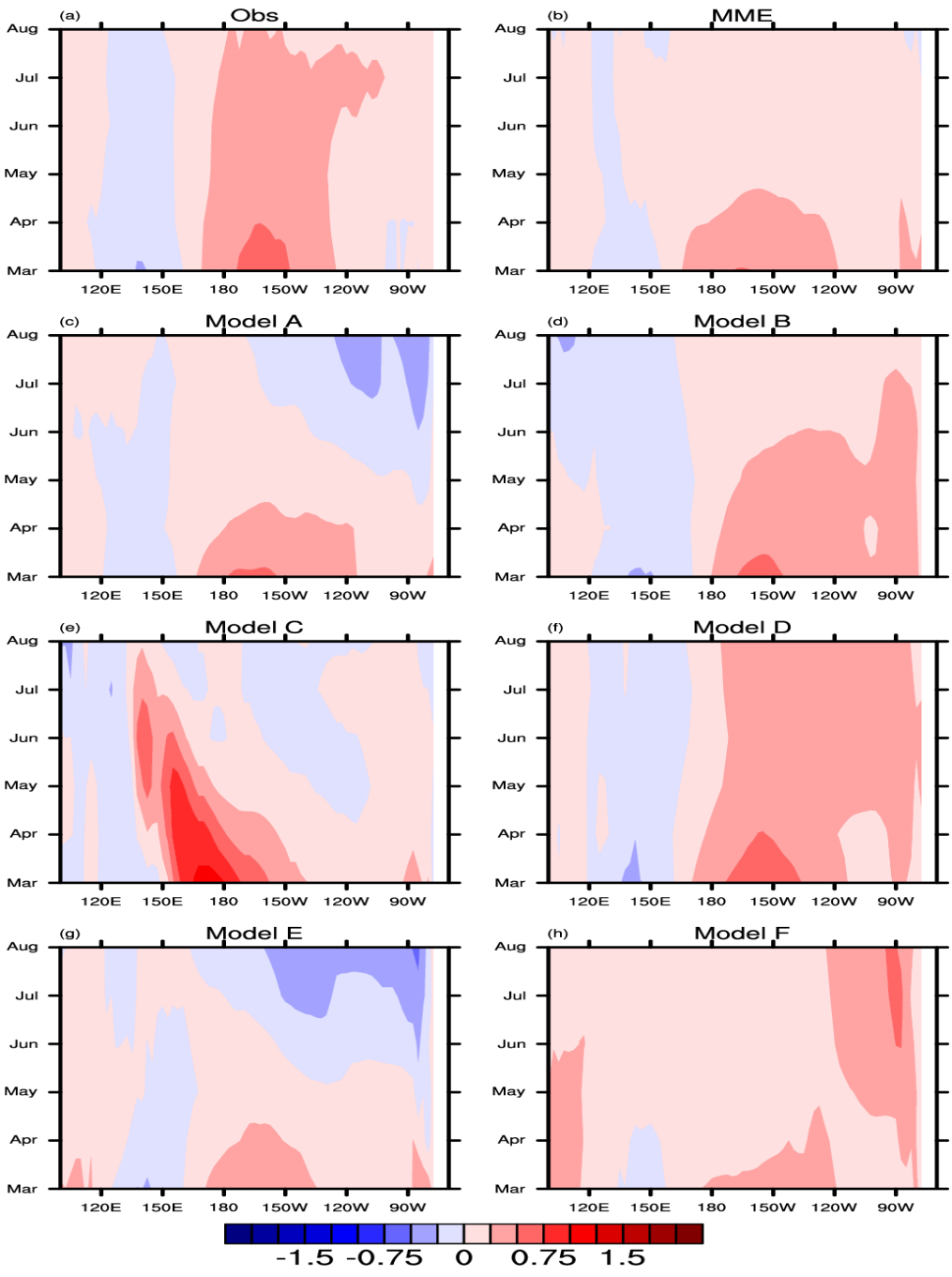

Fig. 3.26 Same as Fig.3.24, but after the peak of El Niño Modoki events in 1987, 1991, 1992, 1995, 2003 and 2005. See scale bar at bottom (units: °C).

3.7 Discussion and Summary of chapter 3

Generally, the CGCMs could reproduce the canonical ENSO patterns well. However, the predicted canonical ENSO patterns still have different features to each other. The similar case happens for the ENSO Modoki case. Therefore, using the projection coefficients to replace the principle component to do further analysis is a good way to unify the ENSO patterns.

It is found that the peak month of the canonical ENSO is in December. An obvious cycle can be observed for the canonical ENSO. Most of the models can capture the canonical ENSO cycle. However, there is a tendency that the CGCMs would develop or decay the canonical ENSO earlier for 1 to 2 months. For the ENSO Modoki, the peak month is in January. It is also suggested that the projection coefficient is a better representative to the ENSO Modoki.

The main idea behind the projection coefficients is to project both observational and model simulated SSTA on the two leading observed SSTA EOFs. The reason to do so is that the EOF patterns are quite different among the models. If the simulated EOFs of SSTA are used instead, the comparison among the principle components will become meaningless. Therefore, the observed EOF patterns are used for all SSTA projection in order to unify the analysis by accessing how well the models can reproduce the observed El Niño/El Niño Modoki SSTA and how well the models can differentiate the two types of El Niño.

The method of the degree of mixings helps access the ability of the models to differentiate the two ENSO types. It is seen that the model who has low value of degree of mixings tends to give good differentiation of the pattern of ENSO.

For the predictions of the persistence of the two ENSO flavors, it is found that the overall predictions of the APCC models for the canonical ENSO are better than that of the ENSO Modoki.

The reason is that the models generally decay ENSO Modoki too quickly like the canonical ENSO, while the Modoki in observations tends to persist.

Chapter 4

Impacts of the two flavors of ENSO on East Asia Climate and their behaviors in CGCMs

This chapter accesses the observed impacts of the two ENSO flavors mainly on the East Asia climate. The behaviors of the impacts in the APCC models are also studied. The patterns of the two flavors of ENSO associated with the circulation structure are assessed through composite analysis. The velocity potential and divergent winds are used as the indication of the Walker circulation. Moreover, the stream function is adopted to indicate the well-known Philippine Sea Anticyclone (PSA), which has great influence to the East Asian climate. Also, the relationship between the predictability of rainfall over East Asian region and the SSTA during ENSO are studied by scatter plots of pattern correlation, which will be shown in section 4.3 of this chapter. By accessing the performance of the models in predicting the different variables of the East Asian climate, the curial factor affecting the predictions of EA climate during ENSO events are pointed out.

4.1. Introduction

4.1.1. Observed and predicted impacts of ENSO on East Asian climate

As the two largest contributors to the tropical Pacific SSTA, the two flavors of ENSO can also affect the global climate during the whole cycle of the ENSO events. The climate impacts of the two flavors of ENSO are not only restricted in the in situ ocean regions. Actually, ENSO could affect different regions over the tropical Pacific rims and even the globe such as China [Weng *et al*. (2007), Weng *et al*. (2009); Feng and Li (2011)], Australia [Nicholls *et al*. (1996), Power *et al*. (1999), Suppiah (2004), Wang and Hendon (2007); Taschetto and England (2009)] and North America [Larkin and Harrsion (2005); Mo (2010)].

4.1.2. East Asian summer monsoon and the Philippines Sea Anticyclone

The East Asian summer monsoon (EASM) is one of the most significant components over the East Asian climate variables. With the profound influence of climate states, the East Asia and the adjacent regions are greatly affected by the EASM [Lau and Li (1984), Yasunari (1991) and Lau (1992)]. Moreover, the behavior of the EASM is totally different during different seasons and thus it brings great and different impacts interacting with the existence of ENSO [Zhang *et al*. (1996), Tomita and Yasunari (1996) and Ji *et al*. (1997)]. For example, during the peak season of the canonical ENSO (boreal winter), the cold SSTA is setup over the western tropical Pacific which suppresses the winter monsoon. As a result, the southeastern Asia such as southeast China and Korea become warmer and wetter [Wang *et al* (1999a), Tao and Zhang (1998); Kang and Jeong

(1996)]. Therefore, including the EASM in the consideration of how ENSO affects the East Asian climate is a must.

Many previous studies pointed out that the behavior of the Philippine Sea Anticyclone is the major factor affecting the East Asian monsoon during the decaying summer of the canonical ENSO [Wang *et al* (2000), Wu *et al*. (2003), Lau and Nath (2006) and Chou *et al*. (2009)]. In fact, Wang *et al*. (1999b) has already suggested the possible mechanism between the precipitation patterns and the location of the Philippine Sea Anticyclone. That is, the anomalous PSA is enhanced over the western Pacific is first generated by the response of the descending Rossby-wave by the eastern-central warming of the canonical ENSO and the local SST cooling. As the background northeasterly exist, the weaker (stronger) wind speed setups to the west (east) of the anticyclone making the anticyclone system slow travel eastward. The associated dry (wet) condition is induced overt the west (east) of the anticyclone. At this point, the canonical ENSO warming plays a crucial role to the precipitation over the East Asia.

4.1.3. The focus of the present chapter

In the previous chapter, behaviors of the two flavors of ENSO in observed and modeled environment are examined. There are two main things we could find in different sections in chapter 3. The first one is that the great and different natures between the two flavors of ENSO. The second is the different predictions of ENSO from models compared with the observations. With no doubt, the canonical ENSO and ENSO Modoki are actually two different phenomena according to the results in the previous chapter. In addition to this, there are some questions being asked next. ow these two phenomena affect our climate. In addition to this, the other question will be can the models reproduce those impacts and what can these results help us understand the nature of the climate impacts during ENSO events.

4.2. Impacts of ENSO on EA Climate and their Characteristics in Coupled Model Environment

Composite circulation anomalies over East Asia are calculated, in order to examine how the two El Niño flavors affect the regional climate during their decaying phases. Left panels of Fig.4.1 show the anomalous rainfall, wind vector and stream function at 850hPa for canonical El Niño in spring. Based on observations (see Fig.4.1a), an anomalous low-level anti-cyclone is found over the east of the Philippines Sea. Such an anti-cyclonic feature is seen to induce a large dry zone over a large area of the western Pacific from the equator to about 20ºN and, at the same time, wetter-than-normal conditions are found over the south China coast, sea to the south of Japan and south Japan, consistent with the moisture transport by the anomalous southerlies. The aforementioned circulation features, including the concomitant SST signals in the western north Pacific (see Fig.4.1b), are reminiscent of the Philippines Sea anti-cyclone (PSA) and its associated SST pattern described by Wang *et al*. (2000). The MME average indicates that coupled models can generally produce these features during decaying canonical El Niño in spring (see Fig.4.1c). Like the observations, the PSA is found and accompanied by a large dry zone on the western Pacific. Again, the PSA corresponds to the sinking motion induced by the negative SSTA in situ (see Fig.4.1d). The southerlies and the associated wet condition at 120ºE in models can also be captured. However, a wrong wet condition is found from 140ºE to 160ºE in the subtropical region. A possible reason is that the southwesterlies at about 20ºN is over-estimated in models. Moisture from the equator at 120ºE is further transported northeastwards by the southwesterlies. Besides MME average, we have also examined two model components of the APCC models - Model D and E. Model D, which can reproduce the persistence of El Niño, can capture the location of the anti-cyclone well (see Fig.4.1e). The associated southerlies and precipitation pattern in tropical East Asian region and western Pacific are relevant to

the observations. Those features are consistent with the upper-level circulation in Fig.4.1f. Nevertheless, Model D experiences similar failure to the MME average. That is, the wet condition in the subtropics extends too far from 120ºE to the western Pacific. Another selected component of the APCC models is Model E, which does not predict El Niño persistence well during the decaying phase. Like the MME average and Model D, Model E predicts wrong precipitation condition in the subtropical western Pacific (see Fig.4.1g), but other circulation features such as location of the Philippines Sea anti-cyclone, dry band over the equatorial western Pacific and the wet condition over the south China coast are well captured. Therefore, it is stated that the location of the PSA is highly related to the upper-level sinking motion during the decaying spring of canonical El Niño. In addition to this, the precipitation over East Asian region is controlled by the location of the PSA. The overall models can well captured the features mentioned above, except they trend to have too strong southwesterlies over the subtropical region inducing wrong wet condition over western Pacific. This failure may be attributed by the insufficiency of model predictions outsides the tropics.

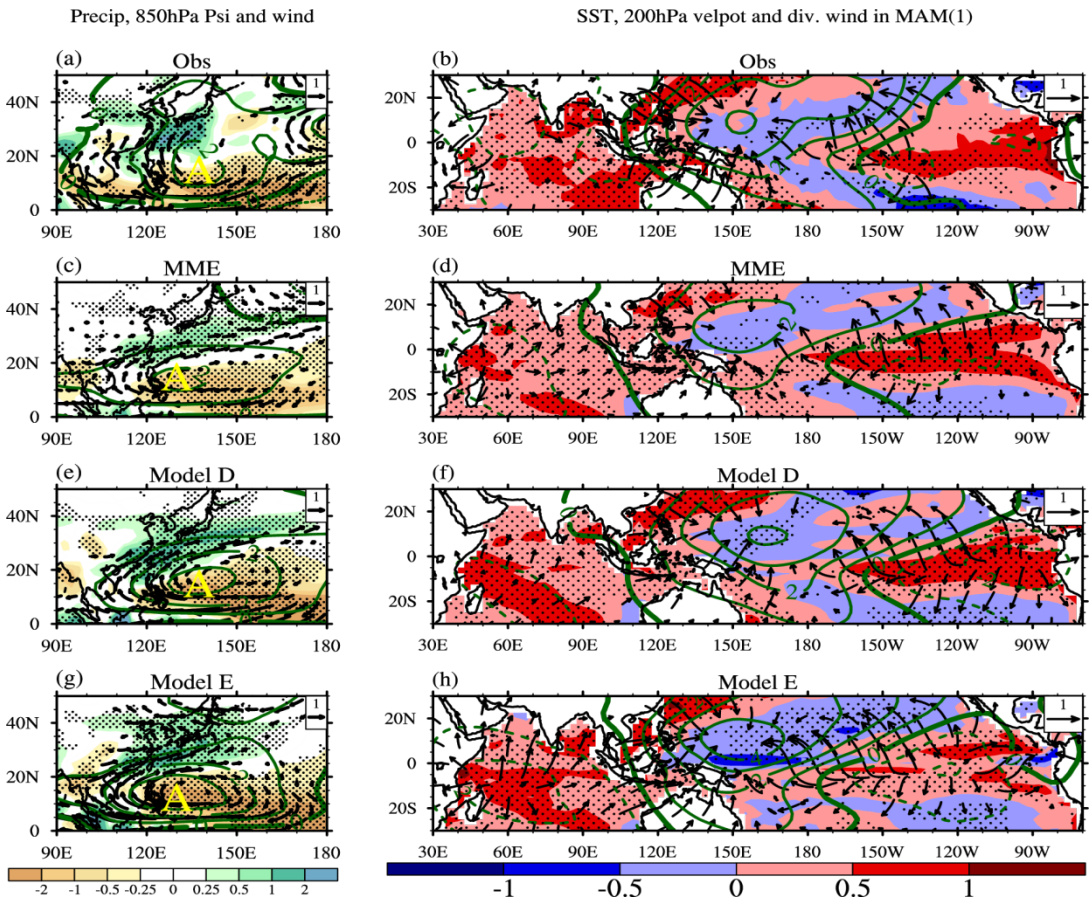

Fig. 4.1 Composite for (a, c, e, g) anomalous rainfall (shading; see scale bar at bottom left, units: mm/day), 850hPa wind (vectors; see scale arrow at top right of each panel, units: ms^{-1}) and stream function (contours; in intervals of $10^6 m^2 s^{-1}$), and (b, d, f, h) the corresponding SSTA (shading; see scale bar at bottom right, units: °C), 200hPa divergent wind (vectors; see scale arrow at top right of each panel, units: ms^{-1}) and velocity potential (contours; in intervals of $10^6 m^2 s^{-1}$) in MAM after the peak of El Niño events in 1983, 1988 and 1998. The letter "A" indicates the position of the low-level anticyclone in western north Pacific. See text for details. Dotted regions over the ocean indicate SSTA significant to the 90% confidence level.

Also shown in the right panels of Fig.4.1 are the SSTA, anomalous wind vector and velocity potential at 200hPa during canonical El Niño in the same boreal spring season. It shows the anomalous Walker circulation with its sinking branch located over the central-western Pacific; such placement is consistent with the low-level anti-cyclone in the same region. Also, significant warming is found over the whole Indian Ocean, as well as the eastern Pacific cold tongue region. Over these two equatorial regions, anomalous upper-level divergence (and hence rising motion) can be discerned. For the observations in Fig.4.1b, it is found that the sinking branch can actually be considered as two split cells to the left and right of the international dateline respectively. For the cell centered at 150ºE, the divergent flow induced by the Indian Ocean warming acts as the main source of this overturning circulation. The divergent flow by canonical El Niño also contributes a little part to the circulation. However, for the cell centered at 170ºW, the sinking motion is almost completely driven by canonical El Niño. This feature is curial to the location of the Philippines Sea anti-cyclone and hence the East Asian climate impacts. It is seen that coupled models can broadly reproduce these features. The position of the cell of sinking is closely related to the position of the Philippines Sea anti-cyclone in the observations and model predictions. Although the amplitude of the divergent flow for the MME average is weaker than that of the observations, it still displays the position of sinking motion at 150ºE very well. The sinking motion is induced mainly by the Indian Ocean divergent flow and partly by the divergent flow from eastern Pacific. Most of the flows from east Pacific go to the sinking branch at about 160ºW. Those predictions are similar to the observations. Similar case is found in the predictions of Model D and E.

Left panels of Fig.4.2 show composite same as those in left panels of Fig.4.1 but for the decaying summer of canonical El Niño. Observations show that the low level anti-cyclone has now shifted northwestward to the South China Sea (see Fig.4.2a). Dry condition is found along the south China coast this time because of the shift of the anti-cyclone. Unlike the decaying spring of canonical El Niño, the wet zone is outsides the tropics and to the northeast of the Philippines Sea anti-cyclone instead of being insides the tropics and to the north of the anti-cyclone. However, the models could not show this shift well (see the MME average in Fig.4.2c). The models generally could predict the existence of the anti-cyclone, but they fail to show the northwestward shift. For predictions of Model D (a model predicts the persistence of canonical El Niño very well) in Fig.4.2e, location of the anti-cyclone is over the central western Pacific, which is located farther east compared to observations. Nevertheless, Model E, which is not good at predicting persistence of canonical El Niño, can well predict the northwestward shift of the anti-cyclone and so the dry condition over the south China coast is well captured. When accessing high-level circulation during the decaying summer of the canonical El Niño, the eastern Pacific warming is replaced by a cold SSTA over the central Pacific along with the decay of the canonical El Niño. The Indian becomes the main source of air to the sinking branch and, hence, the anti-cyclone is shifted westwards. The question followed is that how the above circulation features are affected by the upper-level sinking motion.

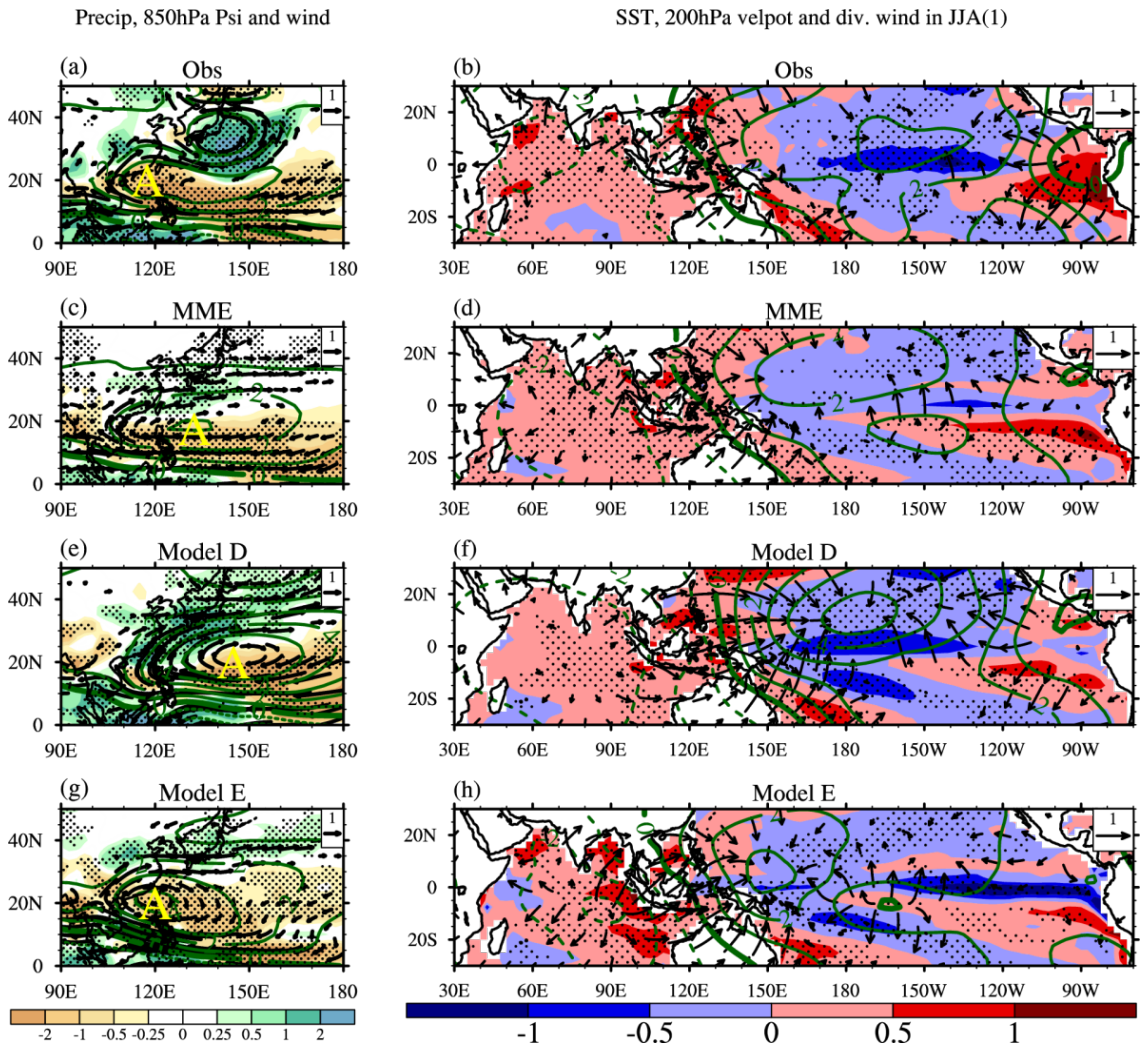

Fig. 4.2 Same as Fig.4.1, but for the JJA season.

Right panels of Fig.4.2 show composite same as the right panels of Fig.4.1 but for the decaying summer of canonical El Niño. It is seen that the anomalous warming of canonical El Niño begins to be weakened, and La Niña ensues to appear in the central Pacific in observations (see Fig.4.2b). The Indian Ocean warming is also significant during the decaying summer of canonical El Niño. The IO warming comes from the charging process during the decaying phase of canonical El Niño named the Indian Ocean Capacitor Effect suggested by Xie *et al*. (2009). The IO warming then induces sinking motion over the central western Pacific via equatorial atmospheric Kelvin wave response acting as a main source to affect East Asian climate in summer. It can be found that canonical El Niño and the Indian Ocean warming both have contribution to a large sinking branch located in the tropical Pacific with the maxima at 150ºW locating from 180ºE to 120ºW, which is consistent with the in situ negative SSTA (see Fig.4.2b). However, if we look closer to the plot, another sinking branch is found from 140ºE to 180ºE acting like a sub-cell (centered at about 150ºE). Moreover, the existence of this sub-cell can mainly be attributed to the equatorial atmospheric Kelvin wave response of the Indian Ocean warming. Although the sinking caused by La Niña SSTA is strong, the position of sinking is far from the western Pacific. Therefore, it can be said that the sub-cell of sinking controls the location of the Philippines Sea anti-cyclone with a dominant role. This also explains why the Philippines Sea anti-cyclone shifts westwards from the decaying spring to summer of canonical El Niño, while the maximum sinking branch shifts eastwards concomitantly. For the MME average (Fig.4.2d), a large cold region is found in the central Pacific, but the cooling is not as obvious as the observations. A large sinking cell is centered at 180ºE. Nevertheless, it can be argued that the sinking cell predicted by the MME average is actually combined by two individual cells (an ellipse with two focuses). The two cells are centered at about 160ºE and 160ºW respectively. The failure to predict strong SSTA cooling in the central Pacific results in two comparable cells rather than a large cell with a sub-cell. It is seen that the

location of the PSA is related to the cell centered at 160ºE. However, the northwestward shift of the PSA is not enough to show dry condition along the south China coast (compare Fig.4.2a with Fig.4.2c). For Model D (a good model to reproduce canonical El Niño persistence) in Fig.4.2f, it is found that the central Pacific cooling and the Indian Ocean warming are well captured (despite the cooling region is far west compared with observations). However, the strong SST cooling dominates the sinking motion over the central western Pacific, which changes the expected two-cell structure. A single strong sinking cell is located at 175ºW instead. In addition to this, the position of the PSA is shifted to the east. This also changes the moisture transport over the East Asian region making the south China coast wet (see Fig.4.2e). For Model E (a poor model to reproduce canonical El Niño persistence) in Fig.4.2g, it is seen that the predicted Indian Ocean warming is well captured. Anomalous SST cooling is found over the eastern Pacific instead of central Pacific. However, since the SST cooling is over eastern Pacific, it does not affect the sinking induced by the IO warming like what happens in Model D (see Fig.4.2f). The IO warming response determines Western Pacific circulation. The Philippines Sea anti-cyclone shifts northwestwards like observations making predictions of precipitation over the Mayu rainfall region correct.

For climate impacts of El Niño Modoki events, left panels of Fig.4.3 shows the composites same as left panels of Fig.4.1 but for the decaying spring of El Niño Modoki. One can observe a large dry band extending form Indo-China region to the South China coast, South China Sea, the Philippines and western Pacific associated with the low level anti-cyclone for the observations (see Fig.4.3a). However, anti-cyclonic flow is not obvious, except the flow along the south China coast extending to southern Japan. One can also observed the enhanced rainfall over the equatorial western Pacific near 150°W-180°W. This is a result of the local positive SSTA of El Niño Modoki. All of the above features are different from canonical El Niño. Anomalous precipitation condition during the same period of canonical El Niño is located to the west of the Philippines Sea anti-

cyclone (see Fig.4.1a). Also, the anti-cyclone is found over northwestern Pacific with obvious anti-cyclonic flow. SSTA over equatorial western Pacific is also opposite for the two types of El Niño. Different positions of the anti-cyclone for the two types of El Niño can be attributed to their different SST spatial patterns (see Fig.4.3b). That is, warming region of El Niño Modoki is in central Pacific, while the warming region of canonical El Niño is over eastern Pacific. Hence, the dry band induced by atmospheric bridge effect during El Niño Modoki trends to shift to the west compared with canonical El Niño. Another observable feature is the enhanced rainfall over the Yangtze River Basin at about 30ºN. This enhanced rainfall can be attributed to the atmospheric response to the large dry zone over the south China. When accessing simulation from models, it can be found that the models could generally reproduce the anomalous dry condition over East Asia (see Fig.4.3c). The wet condition over equatorial western Pacific is also well captured. However, it can be seen that the anti-cyclone and the driest region are located on tropical western Pacific. At the same time, the dry region over Indo-China region is weaker than that of the observations. The wet region near Yangtze River region is well predicted but a wrong wet region is found over East China Sea. Model C is a poor model to predict the persistence of El Niño Modoki. Nonetheless, Model C correctly predicts the position of the anti-cyclone in South China Sea (see the stream function in Fig.4.3e) and so the dry band. The possible reason to this will be given later. Wet condition can also be found over equatorial western Pacific, although the amplitude is overestimated. It is also found that Model C is able to reproduce the wet condition near Yangtze River. However, the wet region again extends too much to East China Sea like the MME average (see Fig.4.3e). Model D is a good model to predict the persistence of El Niño Modoki. It is, however, found that Model D fails to give precise predictions to East Asian climate impacts (see Fig.4.3g). The position of the low-level anti-cyclone is located at western north Pacific rather than South China Sea. This makes that the driest region shifts to the western north Pacific instead of Indo-China region. The area of wet condition

over equatorial western Pacific is also smaller compared with the observations and the other models. Lastly, Model D can capture the wet condition near Yangtze River. However, the wet region shifts to the south compared with the observations; also, it extends to East China Sea like the other models (compared with Fig.4.3a).

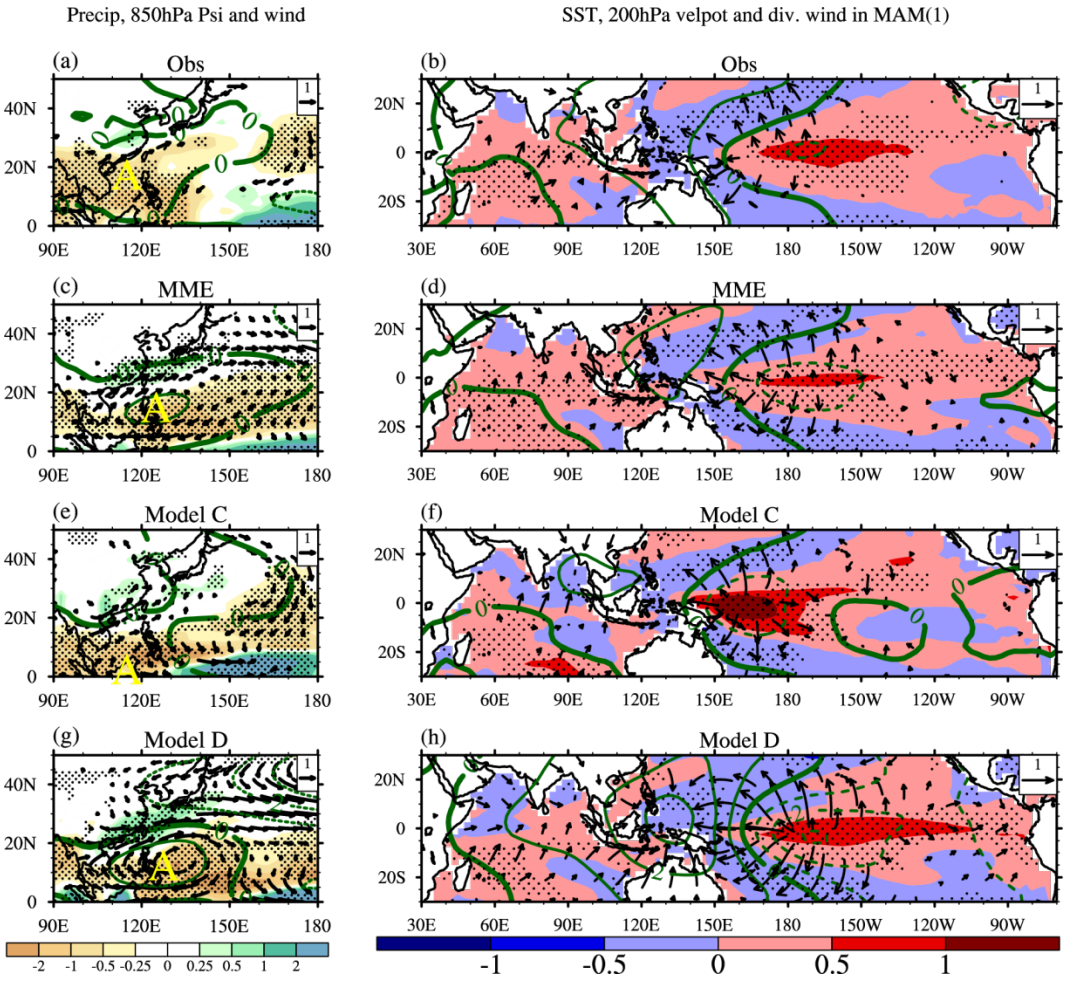

Fig. 4.3 Same as Fig.4.1, except for the MAM season after the peak of El Niño Modoki events in 1987, 1991, 1992, 1995, 2003 and 2005.

Right panels of Fig.4.3 help investigate East Asian climate impacts by displaying composites same as right panels of Fig.4.1 but for the decaying spring of El Niño Modoki. For the observed SSTA (Fig.4.3b), it is found that warming region is located over central Pacific unlike canonical El Niño. Another notable signal is the warming over Indian Ocean. The significant warming is located from equatorial to southern Indian Ocean, while warming during the same period of canonical El Niño is over the whole Indian Ocean basin. It is observed that a sinking branch is located over the Indo-China region and tropical western Pacific for the observations. From Fig.4.3b, there are three visible potential factors to the Indo-China dry band (low-level anti-cyclone). They are 1) high-level divergence near the equator induced by El Niño Modoki, 2) high-level divergence induced by Indian Ocean warming over northeastern sea of Madagascar and 3) high-level divergence from north Indian and Tibetan Plateau. It is seen that enhanced rainfall over equatorial Pacific and suppressed rainfall over tropical western Pacific (from 130°E to 180°E) are consistent with local overturning circulation induced by significant anomalous cooling and warming of El Niño Modoki respectively. However, anomalous precipitation condition is not consistent with local SSTA over seen that the local SSTA over Indo-China region and South China Sea. Therefore, it can be said that El Niño Modoki mainly affects the circulation over tropical western Pacific. The second possible factor is the high-level divergence induced by Indian Ocean warming over northeastern sea of Madagascar. It is seen that the Indian Ocean warming extends to South China Sea. The precipitation condition is not consistent with the in situ SSTA but the warming over South China Sea is not significant. On the other hand, significant high-level winds from southern Indian Ocean are found over South China Sea. Therefore, it can be said that sinking motion over Indo-China region is mainly driven by the remote forcing of southern Indian Ocean warming. The last possible factor is the high-level divergence from north India and Tibetan Plateau. Significant high-level winds from north India and Tibetan Plateau contribute to the sinking motion over Indo-China

region. The possible cause of the high-level divergence from north India and Tibetan Plateau is negative SSTA around the Indian Peninsula. In boreal spring season, insolation is getting strong over Tibetan Plateau, which enhances the upward motion there; in addition to this, the negative SSTA during El Niño Modoki increases the sinking motion around Tibetan Plateau inducing a stronger-than-normal upward motion. Although the negative SSTA signal is not significant, it can enhance the sinking motion near the Indian Peninsula in a certain extent. Fig.4.3d shows us the overall skills of the APCC models (MME average). The sinking branch locates on tropical western Pacific and significant winds from southeast China contribute to the sinking motion this time. The sinking branch can be attributed to the strong El Niño Modoki in the MME average. However, when accessing circulation over Indo-China region, the sinking motion there is not significant. This makes the dry condition there weaker than the observations (compare Fig.4.3c with 4.3a). The SSTA distribution for Model C (a poor model to prediction El Niño Modoki persistence) over South China Sea is actually different from the observed. However, erroneous prediction of the central Pacific warming of Model C makes the sinking branch shift to the west compared to other models, and accidentally gives good predictions to the dry band over tropical western Pacific (Fig.4.3e). This suggests that both the SST response and SST predictions are important for the large-scale predictions over tropical western Pacific. Nevertheless, the large Indo-China dry band, unlike the other APCC models, is well captured by Model C. It can be seen that the high-level divergence from north India, Tibetan Plateau and southern Indian Ocean are significant and contribute to the sinking motion over Indo-China region like the observations. It is also noteworthy that the negative SSTA around Indian Peninsula is significant in Model C. Model D is a good model to predict the persistence of El Niño Modoki; however, it also cannot predict the correct position of the anti-cyclone like the MME (see Fig.4.3h). One can observe that the SSTA is positive over the South China Sea, so it is expected that there is an upward motion. However, it is not the

case according to the results in Fig.4.3g. Therefore, it is interpreted that the sinking branch is mainly driven by the atmospheric forcing called atmospheric bridge effect [Klein and Lau (1999)]. In fact, the SSTA distribution of Model D is similar to that of the observations, but they cannot show correct position of the sinking branch. The possible reason is that the models have too strong response to the SSTA.

Left panels of Fig.4.4 show composites same as Fig.4.3 but for the decaying summer of El Niño Modoki. For the observations in Fig.4.4a, the low-level anti-cyclone and dry region shift to the northwestern subtropical Pacific from 20ºN to 30ºN. The atmospheric response makes the East Asia region over 30ºN wet. Moreover, it is seen that rainfall distribution over China becomes regional. For example, rainfall condition near Yangtze River is dry, while the condition near Yellow River is wet. Nonetheless, the APCC models can only capture the rainfall condition over the tropical western Pacific under 20ºN. They generally reproduce the low-level anti-cyclone over South China Sea instead of the sea of southern Japan.

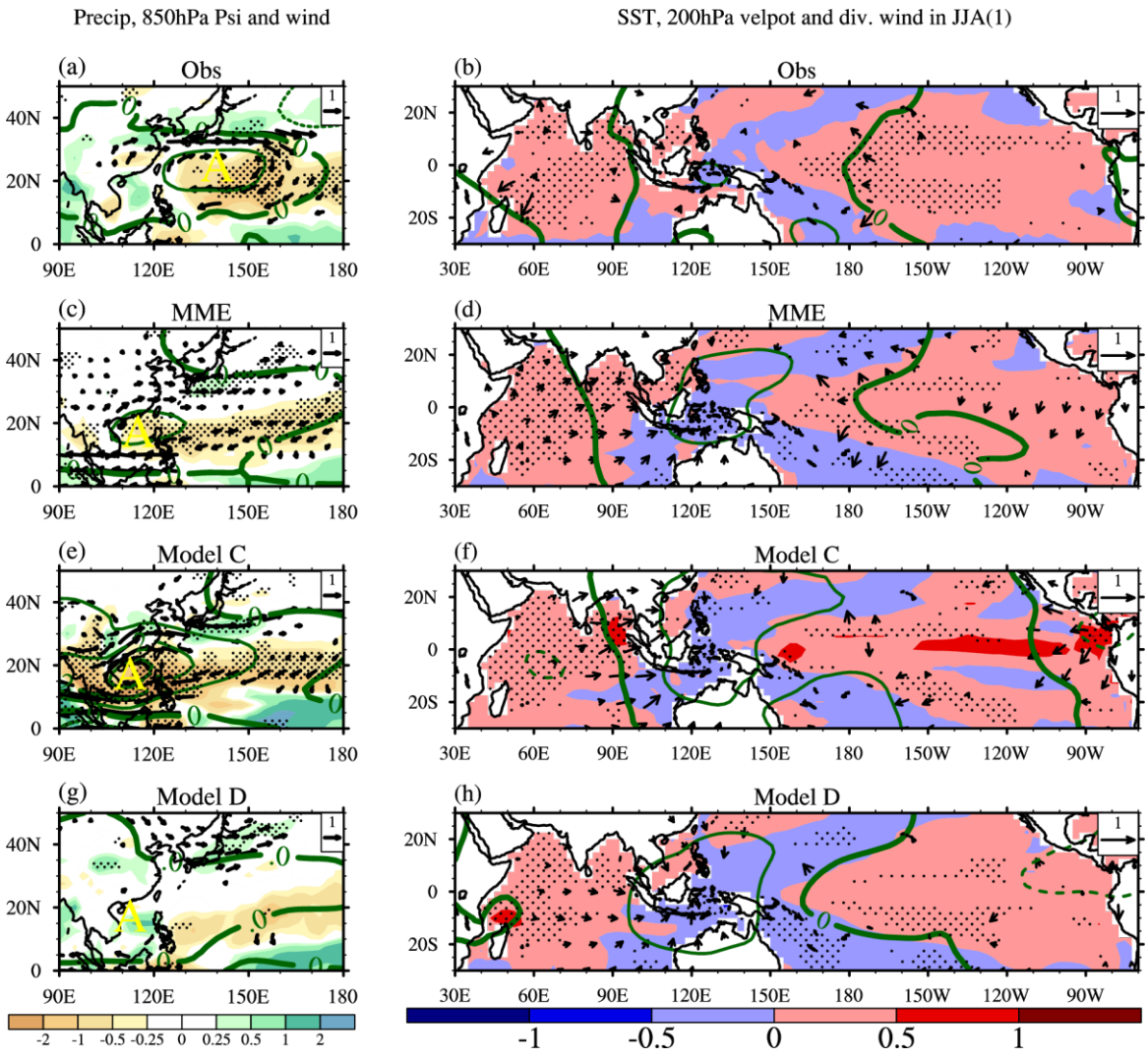

Fig. 4.4 Same as Fig.4.3, but for the JJA season.

Right panels of Fig.4.4 show composites same as Fig.4.2 but for the decaying summer of El Niño Modoki. For the observed high-level circulation (see Fig.4.4b), it is shown that El Niño Modoki SSTA is weakened during the decaying summer (but still significant) compared with spring season, while canonical El Niño trends to decay rapidly and become La Niña events. The southern Indian Ocean warming is also found significant. It is seen that the SSTA over the sea of southern Japan is positive; however, a low-level anti-cyclone is found there (see Fig.4.4a). It denotes that the atmospheric driving force is stronger than the SST forcing. The APCC models can generally capture El Niño Modoki warming correctly. However, they fail to capture the low-level anti-cyclone. It is seen that the APCC models (MME, Model C and Model D) have similar behavior to predict the sinking branch over East Asia. The strongest sinking motion of the models is found over the tropical western Pacific along the equator. Such a difference between the observations and model simulation is that the observed significant Indian Ocean warming is located on the southeastern sea of Madagascar (south of the equator), while the modeled Indian Ocean warming extends in the whole tropical Indian Ocean (along the equator). Such a difference can be attributed to a mechanism that the modeled Indian Ocean warming along the equator tends to thicken the local atmosphere and induce sinking motion in the tropical western Pacific via equatorial atmospheric Kelvin wave; by which, the existence of the observed low-level anti-cyclone cannot be explained. Therefore, the induced anti-cyclone in models is trapped under 20ºN, while the observed anti-cyclone is above 20ºN. However, it is still uncertain that whether canonical El Niño, Indian Ocean warming to the southeastern sea of Madagascar or the local monsoon circulation dominates to induce the low-level anti-cyclone. Therefore, there should be other factors affecting East Asian climate during the decaying summer of *El Niño* which is going to be shown in the next section.

4.3. The relationship between ENSO and East Asian monsoon state

The relationship between predictability of East Asian summer rainfall and predictability of El Niño can be shown by scatter plots of the pattern correlation of East Asian precipitation against the pattern correlation of El Niño SSTA (see Fig.4.5). Pattern correlation coefficient is a tool to reveal the prediction skills of models. With that in mind, the relationship between the prediction skills of two variables can be shown by plotting them on a scatter plot (correlation coefficients). For example, if the correlation between pattern correlation of canonical *El Niño* SST and the EA rainfall is high, then it can be interpreted that canonical *El Niño* SST can be a cause of EA rainfall.

Fig.4.5a shows the scatter plot of pattern correlation between observed and predicted precipitation over East Asia [10°S-40°N; 90°E-150°E] against pattern correlation between observed and predicted SSTA over tropical Pacific [20°S-20°N; 120°E-70°W] for decaying summer (JJA) during canonical El Niño. The correlation coefficient between the prediction skills of canonical El Niño rainfall and canonical El Niño prediction skills is 0.318; the models show a degree of relationship between the rainfall and El Niño predictability in both 1 to 3 and 4 to 6 month lead predictions in decaying summer. Fig.4.5b shows the scatter plot of pattern correlation between observed and predicted precipitation over East Asia [10°S-40°N; 90°E-150°E] against pattern correlation between observed and predicted mean stream function in the same region for decaying summer (JJA) during canonical El Niño. The correlation coefficient of the graph is 0.424. It is interpreted that both prediction skills of El Niño and mean monsoon over East Asia are important to the El Niño rainfall over East Asian region during decaying summer of canonical El Niño. Fig.4.5c shows the scatter plot same as Fig.4.5a but for decaying summer during El Niño Modoki. It is seen that the relationship between the prediction skills of Modoki rainfall over East Asia and El Niño Modoki is not significant (correlation coefficient = 0.078). However, if the relationship between the

prediction skills of Modoki rainfall over East Asia and the mean stream function is accessed, one can find that the correlation coefficients increase rapidly to 0.366 in the decaying summer (see Fig.4.5d). This shows that good predictions of the mean circulation over the EA are statistically related to the good prediction of ENSO Modoki precipitation during the decaying summer.

It is also important to take a look at the error structures of Fig.4.5. Fig.4.6 shows the Taylor diagrams of the pattern correlation coefficients of the variables used in Fig.4.5. The correlation ranges from about 0.6 to 0.95, which shows that the models generally give good predictions to the EA monsoon pattern. It can be seen that Model E and the MME average show the best pattern correlatiaon of the mean 850hPa streamfuction over the East Asian region (Fig.4.6a). However, for the 1^{st}-3^{rd} leadtime predictions of Model D (a good model to predict *El Niño* persistence), the root mean square error is relatively higher than the expectation.

Model D and the MME average show good predictions to the two types of *El Niño* SST (see Fig.4.6a and 4.6b). Nevertheless, it is not the case in predicting *El Niño* precipitation over the EA region (Fig.4.6c and 4.6d). It can also be seen that the pattern correlation coefficients of Modoki precipitation is lower than that of the canonical *El Niño*. This is relevant to the finding in the previous section that the climate impacts over the EA is hard to be captured during the decaying summer of *El Niño* Modoki.

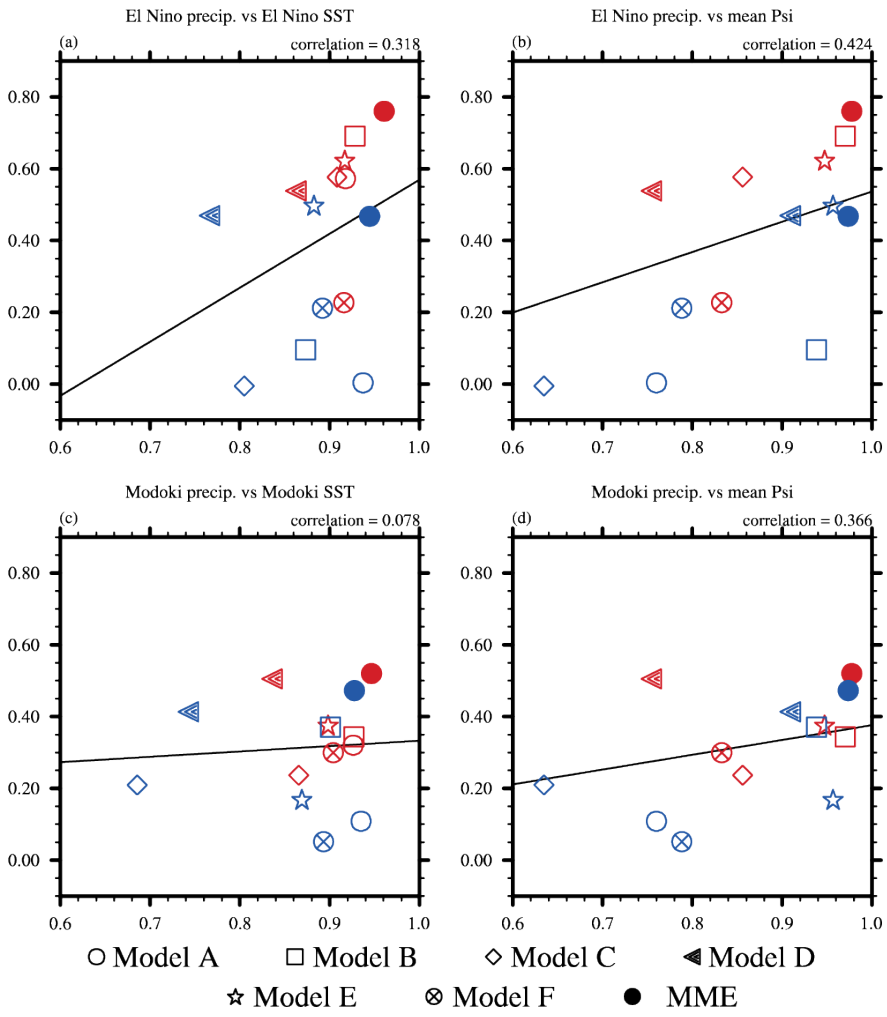

Fig. 4.5 Pattern correlation between observed and model-predicted anomalous rainfall in JJA over East Asia [10°S-40°N; 90°E-150°E] vs. pattern correlation for (a, c) SSTA in JJA over the equatorial Pacific [20°S-20°N; 120°E-70°W] and (b, d) the 850hPa mean stream function over the same East Asian region computed based on observations and model outputs. East Asian rainfall was predicted with leadtime of 1 to 3 (red markers) and 4 to 6 (blue markers) months, after the peak of (a, b) canonical El Niño events in 1983, 1988 and 1998, and (c, d) El Niño Modoki events in 1987, 1991, 1992, 1995, 2003 and 2005, for the JJA season. See legend at bottom.

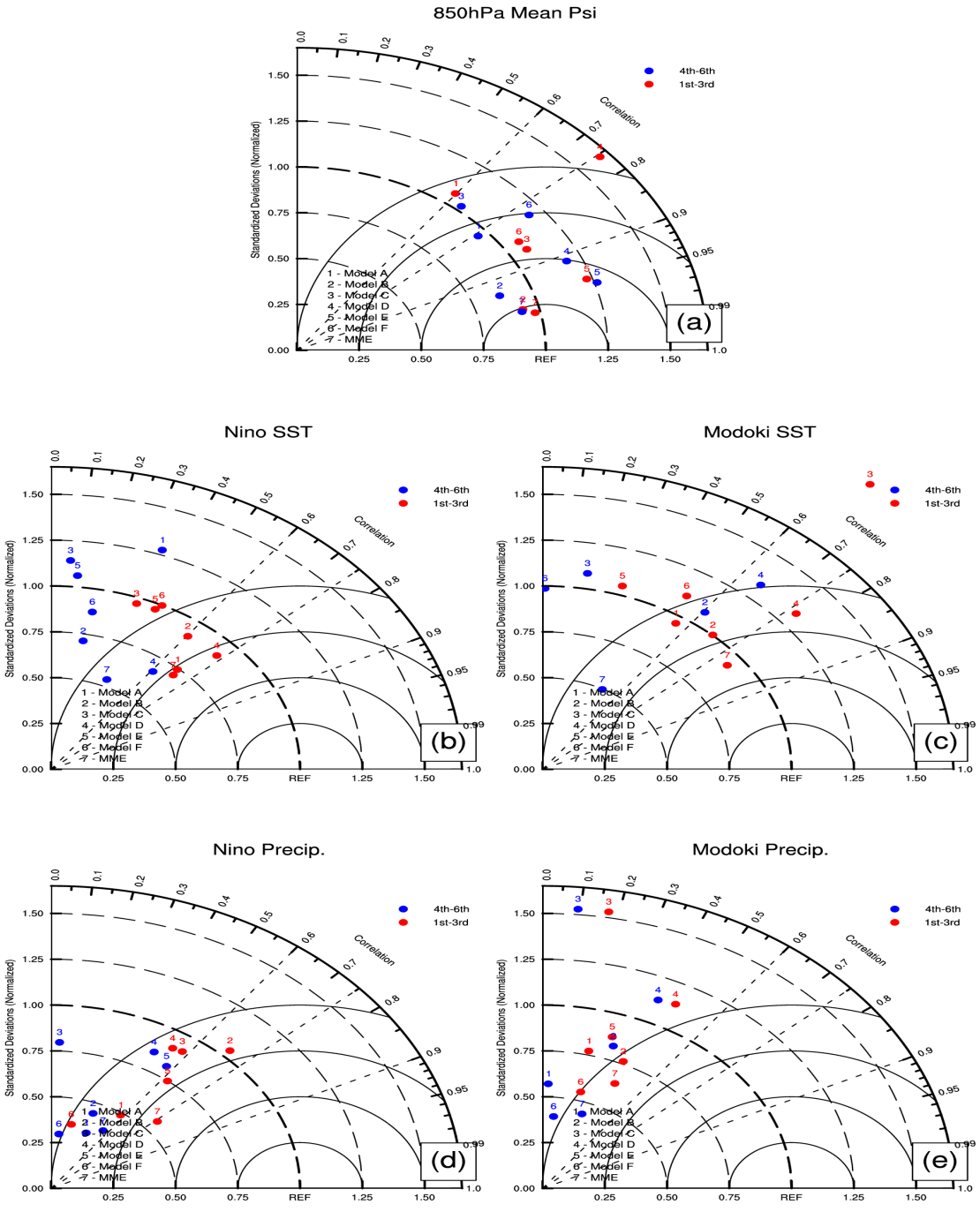

Fig. 4.6 Taylor diagrams of pattern correlation coefficients of a) mean streamfunction over EA, b) canonical *El Niño* SST, c) Modoki SST, d) *El Niño* precipitation over EA and e) Modoki precipitation over EA with observed standard deviations as referenece point.

To investigate how the prediction skill of the East Asian rainfall might be affected by the realism of the mean climate state in models, the monsoon circulation during the summer is shown in Fig.4.6. For the mean climate in summer, the models generally show similar pattern of monsoon at 850hPa and mean stream function with the observations. However, this is not the case for the Model D. The westerly is too strong over the Indo-China region for Model D resulting in the over warming of predicted SST there. This makes the mean monsoon circulation in Model D shift to the east; hence, the low-level anti-cyclone is also shifted eastwards compared with the observations during the decaying summer of canonical El Niño.

It can be summarized that, for the decaying summer of the canonical ENSO, both predictions of the El Niño SST and predictions of mean circulation over East Asia are crucial factors to predictions of El Niño precipitation over East Asia. However, for the decaying summer of the ENSO Modoki, predictions of the *El Niño* Modoki SST seem not an important factor to affect the predictions of ENSO Modoki precipitation, while the predictions of the mean circulation is still crucial during this phase.

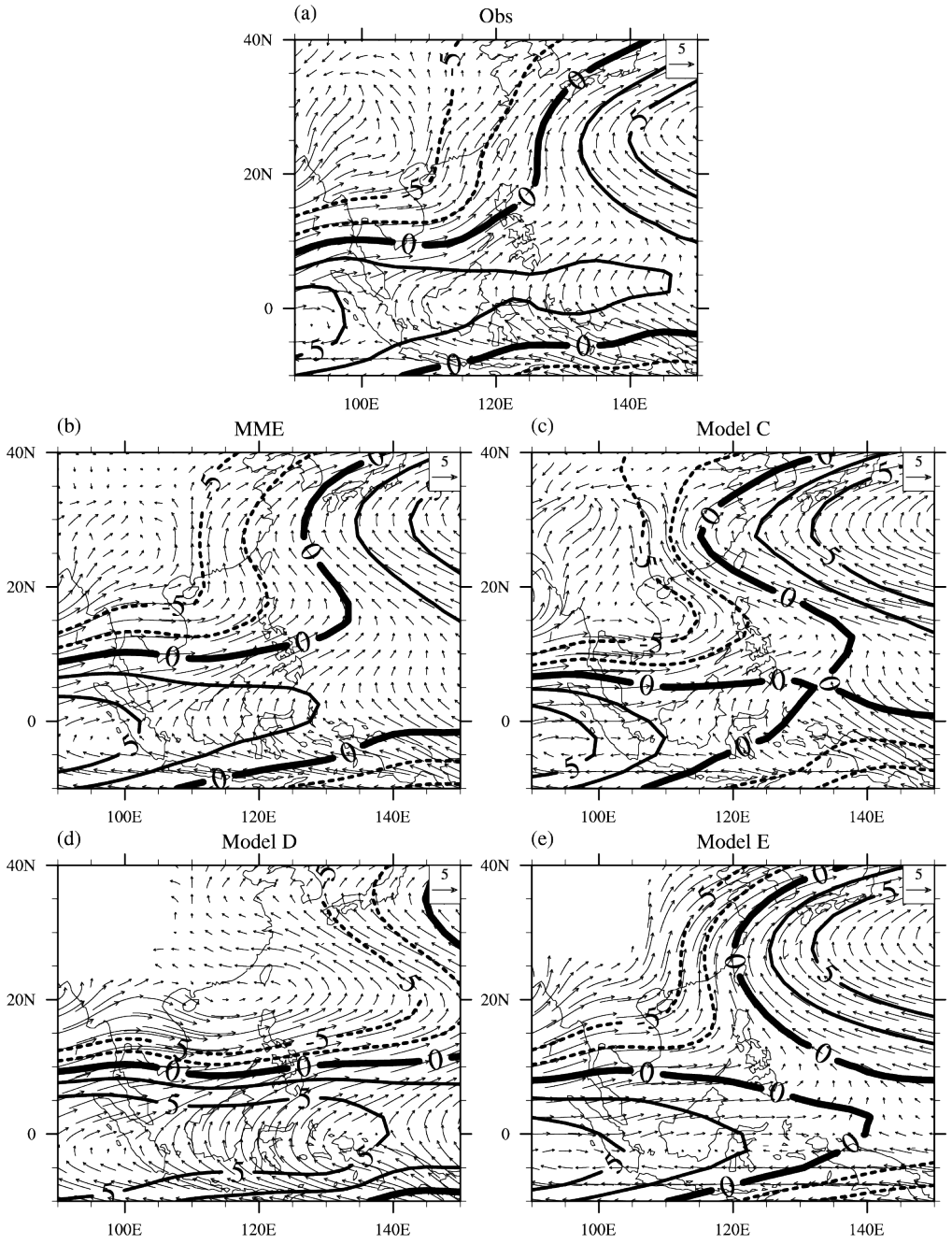

Fig. 4.7 Climatological mean 850hPa stream function (contour; in intervals of $2.5\times10^{6}m^{2}s^{-1}$) and 850hPa wind (vector; see scale arrow at top right of each panel, units: ms^{-1}) during the JJA season from (a) observations, (b) MME average, (c) Model C, (d) Model D and (e) Model E.

4.4. Summary of Chapter 4

It is found that there is an anomalous wet (dry) condition over the south China coast during the decaying spring (summer) of the canonical ENSO. The reason is that the Indian Ocean warming becomes increasingly important from the decaying spring to summer. Therefore, a westward shift of the dry band over the Tropical Pacific happens along the decay.

For climate impacts of ENSO Modoki during its decaying phases, the low level anti-cyclone and dry band are mainly driven by the atmospheric forcing. Although the models give good predictions to the SSTA distribution, the position of the anti-cyclone could not be shown. The possible reason is that the rainfall response by the SST of the models is too strong.

The climate over the southern China becomes regional during the decaying summer of ENSO Modoki. Moreover, the large-scale circulation does not have much effect on the climate there. Therefore, it is interpreted that the climate is driven by other climatic factors like monsoon during the period.

It can be concluded that, for the decaying summer of the canonical ENSO, both the predictions of the El Niño SST and the predictions of mean circulation of EA are the crucial factors to the predictions of El Niño precipitation. However, for the decaying summer of the ENSO Modoki, the predictions of the ENSO Modoki SST seem not an important factor to affect the predictions of ENSO Modoki precipitation, while the predictions of the mean circulation is still crucial at this point.

In addition to this, models which can reproduce good patterns and cycle of the canonical ENSO or ENSO Modoki do not ensure good predictions to the East Asian precipitation, while the models which cannot reproduce accurate patterns and cycle of the two flavors of ENSO can still predict the East Asian precipitation well during the decaying summer of ENSO.

Chapter 5

The Indian Ocean SST Modes, Associated Climate Impacts and their Relationship to ENSO

This chapter examines different Sea Surface Temperature (SST) modes in Indian Ocean. The Empirical Orthogonal Function (EOF) analysis is applied to the whole Indian Ocean Basin to obtain different modes of Indian Ocean. The relationship between the IO modes and the two flavors of ENSO are investigated by calculating the lead-lag correlation coefficients between the IO SSTA mode principle components (PCs) and the PCs of Pacific SSTA.

5.1. Introduction

5.1.1. Previous studies on IO SST modes

There are three known SST modes in the Indian Ocean. The first one is the Indian Ocean Basin Mode (IOBM). The second one is the Indian Ocean Dipole (IOD) and the last one is the Subtropical Indian Ocean Dipole (SIOD). Many studies have supported the existence of the Indian Ocean Basin Mode (IOBM) and its associated mechanism with the canonical ENSO [e.g. Klein *et al*. (1999); Xie *et al*. (2002)]. IOBM is referred to the large warming over the tropical IO and some studies believe that it is an ENSO-induced event. That is, the IO could act as a "capacitor" to store the heat energy of the Pacific during the canonical ENSO events [Xie *et al* (2009)].

In the 1990s, some researchers pointed out that there may be a new SST mode occurring in the tropical Indian Ocean [Saji *et al*. (1999), Webster *et al*. (1999); Yu and Rienecker (1999)]. The studies found that a warm and cold SSTA appear over the western tropical IO and southeastern IO forming a dipole structure in the late boreal fall named Indian Ocean Dipole (IOD). Since then, many studies are carried out against the IOD and the possible impacts of it [Vinayachandran *et al*. (1999), Behera *et al*. (1999), Murtugudde *et al*. (2000)].

5.1.2. Modeling studies on IO SST modes and their Relationship to ENSO

Iizuka *et al*. (2000) tried to simulate the Indian Ocean SST dipole (i.e. IOD) in a coupled general circulation model. There are two main findings in the study. The first one is that the IOD is generally independent of the canonical ENSO. Another finding is that the occurrence of IOD may be due to the ocean dynamics is a key to generate the IOD events by tropical air-sea interaction.

For the model study of IO SST climate impacts during the canonical ENSO, Watanabe and Jin (2002) purposed a set of linear baroclinic model experiments suggesting the Indian Ocean SST plays important role to the development of the Philippine Sea Anticyclone during the canonical ENSO. The model was a newly developed version using the interactive moist processes of the cumulus convection and surface heat fluxes instead of forcing the local convection by the prescribed heating. Although the study did not cover the two flavors of ENSO, this gives hints that the formation of the Philippine Sea Anticyclone is not purely a product from local SSTA forcing. It is also affected by the remote forcing from Indian Ocean SST signals or other atmospheric factors. Another model study on the IO SST climate impacts during the canonical ENSO was carried out by Kug *et al.* (2006).

The relationship between IO warming and ENSO is described by Lau and Nath (1996). They suggested the "Atmospheric Bridge effect" to explain the anomalous warming of the Indian Ocean during canonical ENSO. Klein *et al*. (1999) further proved the study by Lau and Nath (1996) using observational data from ship and satellite data. One critical point was that the SST warming over tropical Pacific could not affect the SST of IO direct, since the two oceans are not connected. With this point in mind, those authors found that the Pacific SSTA affects the IO SST through a series of atmospheric response.

5.1.3. The focus of the present chapter

After reviewing the previous studies about the IO SST modes and their impacts during ENSO, there are two questions to be asked. The first one is that can the IO SST modes be classified? Previous studies concern the tropical regions of the Indian Ocean. However, many recent studies show that great variability can be found in the southern part of the Indian Ocean. It denotes that considering the whole Indian Ocean can change the whole picture of the IO SST modes. Additionally, it is found that the variance of IOD found in Saji *et al.* (1999) is 12% during the studied period. This also makes a concern on how significant of the IO SST modes are. The second question is that if those SST modes exist, what is the relationship between them and the two flavors of ENSO and how do those modes affect the EA climate? Addressing those questions is the objective of the present chapter.

5.2. Indian Ocean SST modes

Fig.5.1 displays the 1st EOF patterns for the observed and modeled SSTA over the whole Indian Ocean domain [40S-20N; 30E-120E] with the variance in the top right of each figure. It is found that the 1st EOF pattern is generally the Indian Ocean Basin Mode (IOBM). The IOBM is a great warming region over the central western Indian Ocean. Unlike the canonical ENSO, the warmest region of the IOBM is located on the western boundary of the Indian Ocean, while the warming is weaker over the eastern IO. It can be seen that the 1st EOF of the observed IO SSTA (Fig.5.1a) contains 31.3% of variance. This indicates that this pattern is significant in the IO.

Generally, the models can capture the IOBM well. For the MME average (Fig.5.1b and c), the EOF pattern is actually close to the observed EOF pattern. The variance for the MME average is even higher than that of the observations (42% and 46% for the 1st -3rd leadtime respectively). The rest of the models can simulate clear pattern of IOBM (Fig.5.1d to Fig.5.1o); however, there are still some poor patterns. For example, Model A shows the wrong warming region over the subtropical region. The 4th-6th leadtime predictions of Model C shows a IOD pattern with a cooling region over the eastern Pacific. The warmest signal of 4th-6th leadtime for Model E shifts to the eastern IO instead of western IO.

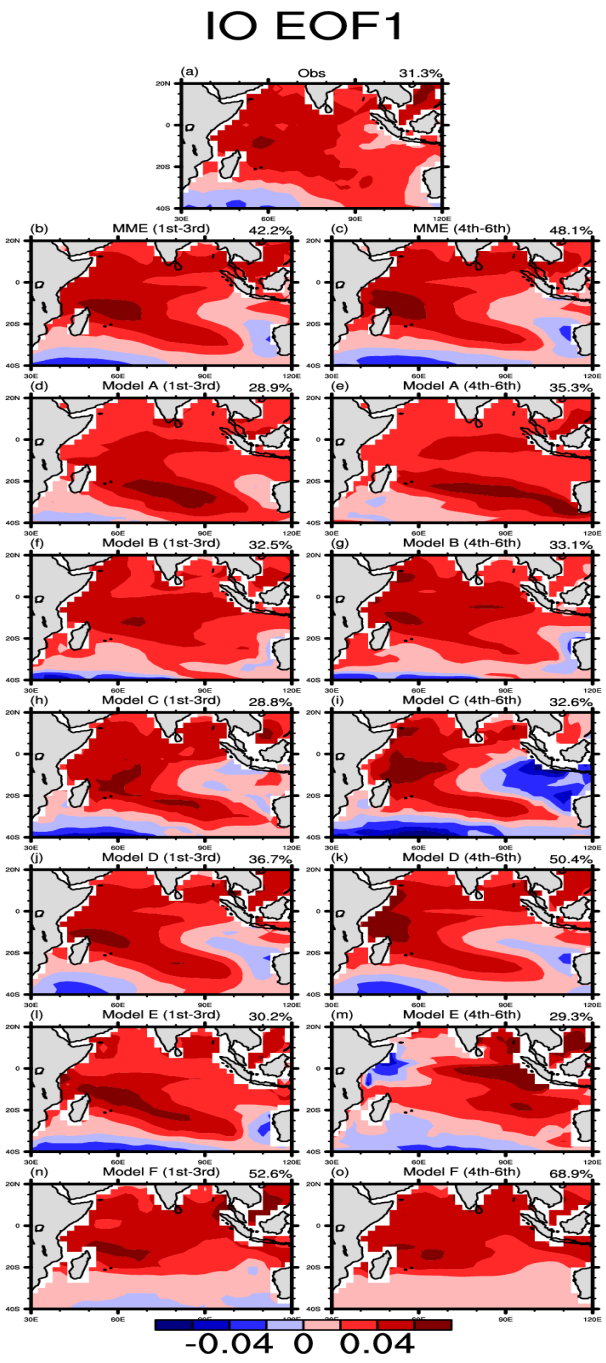

Fig. 5.1 1st EOF of the Indian Ocean SSTA [40S-20N; 30E-120E]

For the second EOF of the IO SSTA (Fig.5.2), a pattern locates over the southern Indian Ocean and has a dipole structure with the warming region over a subtropical western IO and a cooling region over the eastern IO. The variance contains for the 2nd EOF is 13%. It is originally expected the 2nd EOF of the IO SSTA is the IOD. Nevertheless, the IOD is located over the relatively equatorial regions. It is noticed that the IOD pattern does not exist during the studied period.

The interesting thing is that the models tend to show IOD pattern for their 2nd EOF patterns (Fig.5.1b to Fig.5.1o) with a comparable variance with the observed EOF. The east-west gradient of the modeled EOF pattern is obvious for most of the models. It shows that the response of models outsides the tropics over the IO is weaker than the observations.

It is believed that the third EOF (Fig.5.3) is the Subtropical Indian Ocean Dipole. The SIOD is characterized by the anomalous warming at the southern sea of Madagascar and the cooling on the western coast of Australia. The models cannot capture the right pattern of SIOD. However, there are still a few models capturing signals like the 4th-6th leadtime predictions of Model C; the 1st -3rd and 4th-6th leadtime of Model D.

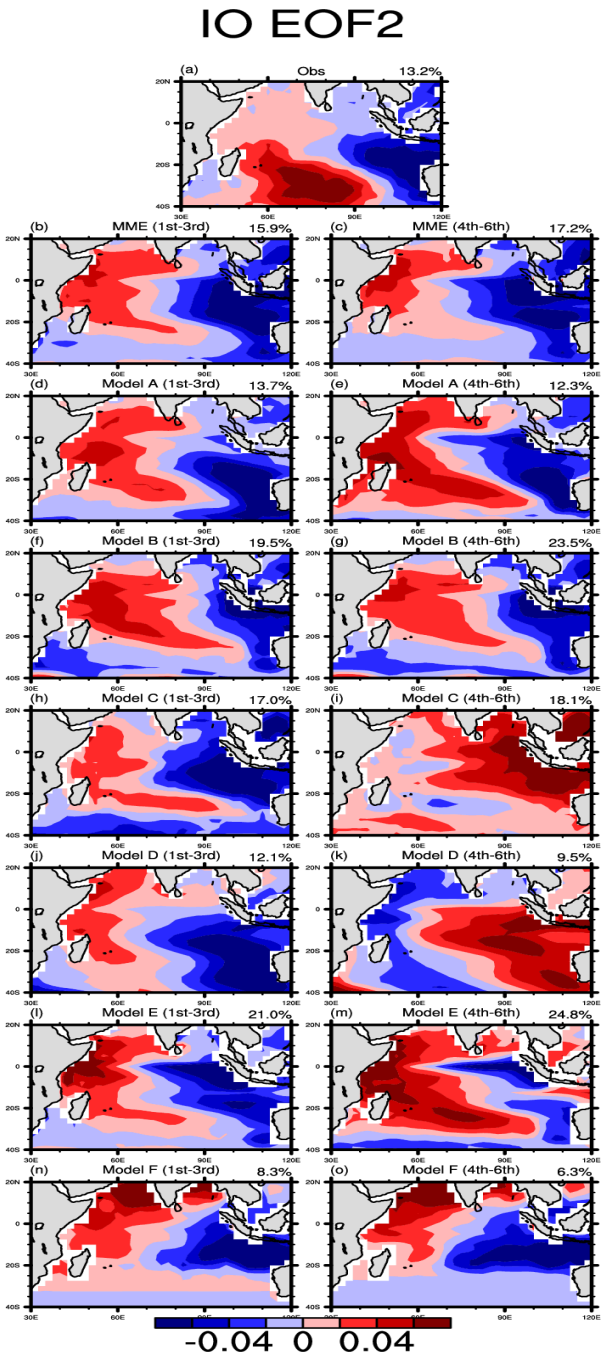

Fig. 5.2 2nd EOF of the Indian Ocean SSTA [40S-20N; 30E-120E]

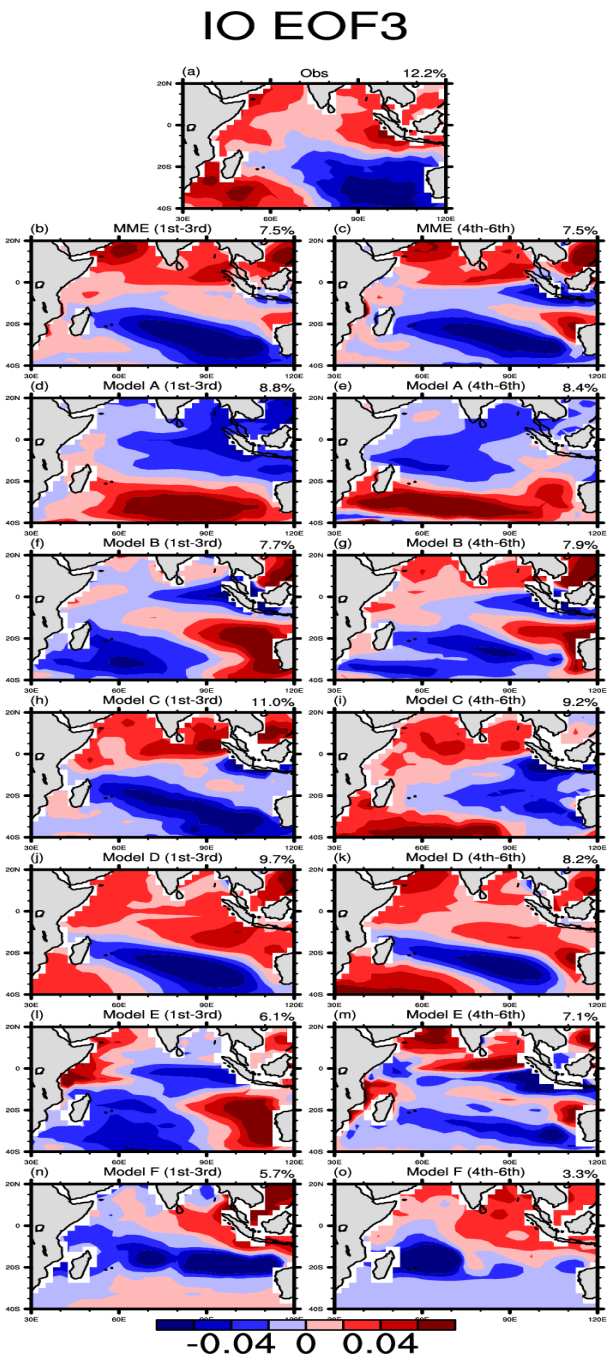

Fig. 5.3 3rd EOF of the Indian Ocean SSTA [40S-20N; 30E-120E]

The EOF4 is a newly discovered mode of the IO SST (Fig.5.4). The feature of it is the horse's hoof like warming pattern over the northeastern coast of Madagascar. It is seen that the variance of the 4th EOF containing in the models is diverse. Only the 1st -3rd leadtime predictions of Model D and Model F have response like the observations. Instead, the SIOD mode is found for the MME average predictions (Fig.5.4b and c).

Table.5.1 summarizes the different modes by showing the correlation coefficients between the IO SST indices and IO SST Principle Component (PCs). It is found that the correlation between the 1st principle component and the IOBM index is 0.966; therefore, it is quite safe to claim that the 1st EOF represents the IOBM. For the IOD, it is found that the correlation between the DMI and PC2 is 0.46. However, the correlation between the DMI and PC1 is 0.4. This denotes that there is projection between the IOD and the first and second modes of IO SSTA EOF. For the SIOD, the SIOD index has the highest correlation coefficient 0.7 with PC3; nevertheless, the index has a significant correlation 0.4 with PC2.

It is seen that the variance among the different IO SST modes are very close and the mixings of them in models are also very high. Therefore, the projection coefficient method is employed to unify the different EOF patterns form models.

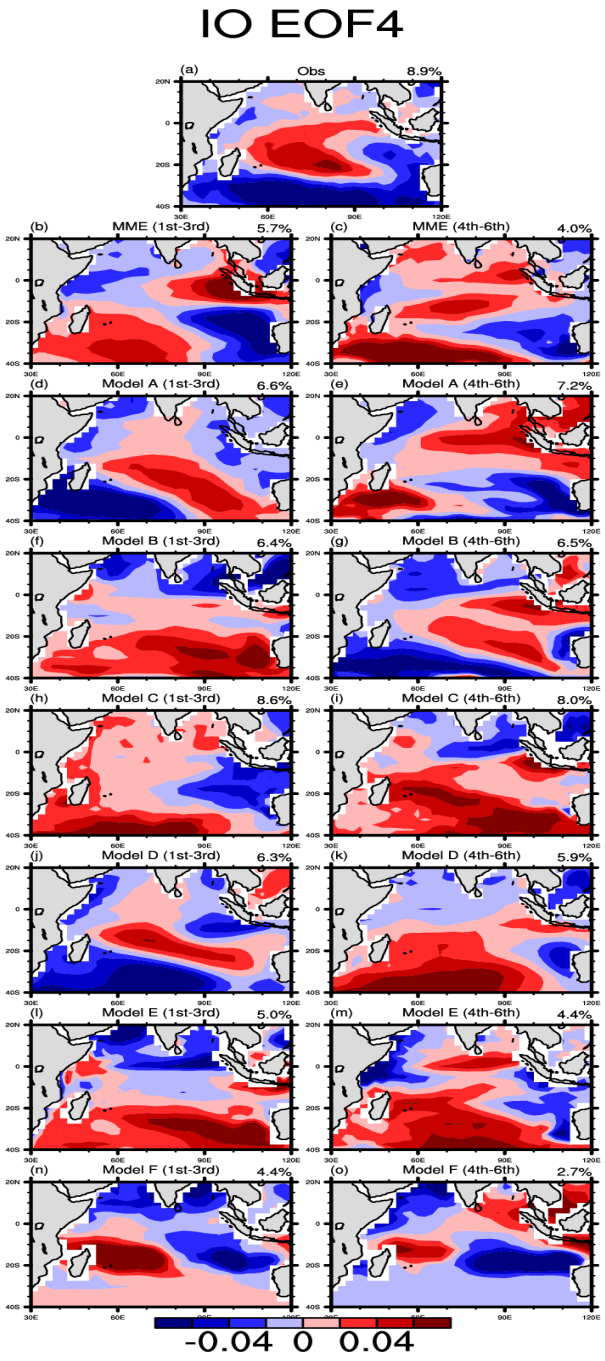

Fig. 5.4 4th EOF of the Indian Ocean SSTA [40S-20N; 30E-120E]

Table.5.1 Correlation Coefficients between the IO SST indices and IO SST Principle Component

	IOBM index	DMI	SIOD index
PC1	0.96623	0.40721	-0.36514
PC2	-0.0259816	0.465886	0.400933
PC3	0.161787	-0.171417	0.717158
PC4	0.133422	0.0541143	-0.294335

5.3 Relationship between the IO SST modes and the two types of ENSO

Fig.5.5 shows the lead-lag correlation functions between the PjC1 of the tropical Pacific SSTA versus the PjC four IO SSTA EOF modes found above. For the canonical ENSO and IOBM, the lead-lag correlation (Fig5.5a) shows the strong relation between the two phenomena from the peak of the canonical ENSO until 6 months after the peak of ENSO. It means that the IOBM tends to occur at the peak of ENSO and intensify after in the coming six months after the peak of the canonical ENSO. This observation is relevant to the findings of Xie *et al*. (2009). The models' results support the findings. For the IOD like pattern (Fig.5.5), there is a strong negative signal found before the peak of the canonical ENSO. The models also have the similar behaviors. For the SIOD and the EOF4 of the Indian Ocean, there is no obvious relationship to the canonical ENSO. The correlation coefficients for the observations and the models are stay in low value below the 95% significance level during the whole period.

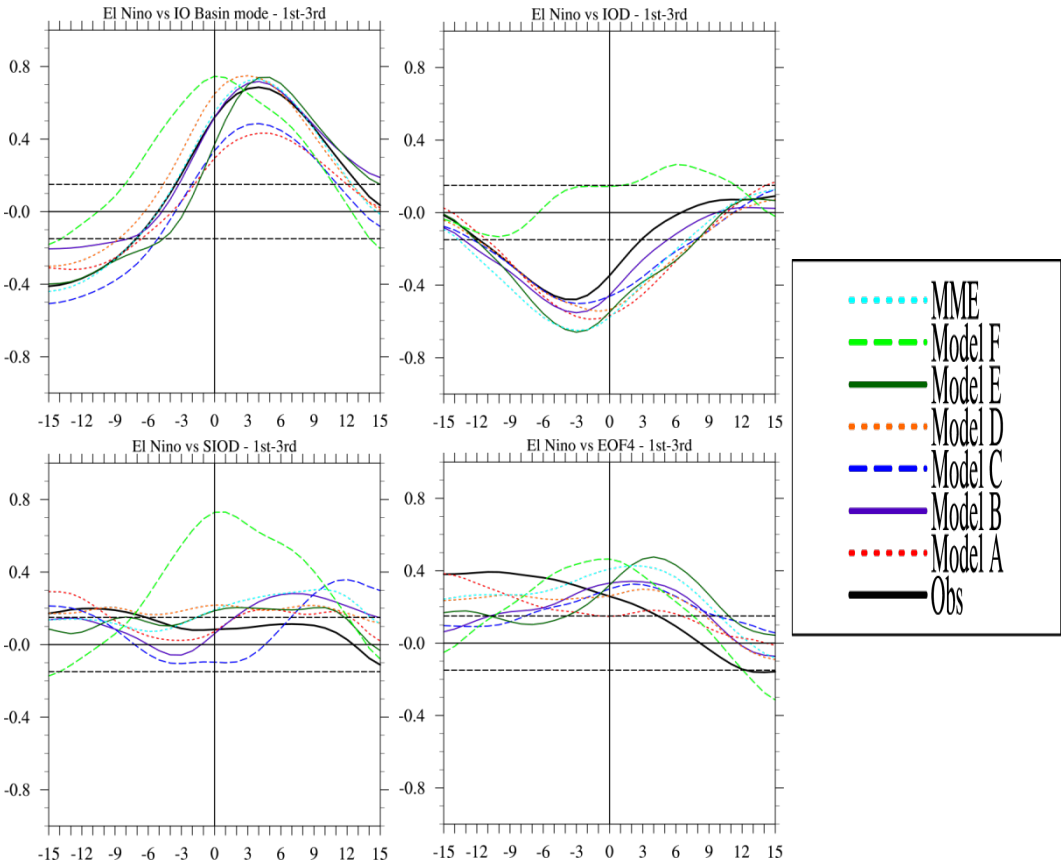

Fig. 5.5 Lead-lag correlation functions between the PjC1 of the tropical Pacific SSTA (canonical ENSO) vs IOBM (top left), IOD (top right), SIOD (bottom left) and the EOF4 (bottom right). Dash lines indicate 95% significance level using R-test.

For the ENSO Modoki and the IOBM and the SIOD, there is no significant relationship between the ENSO Modoki and the two phenomena. However, when accessing the Modoki and the IOD like correlations, there is a strong negative signal for the IOD like pattern along with the ENSO Modoki. The EOF4 for the IO SSTA also gives significant signal during the cycle of ENSO Modoki

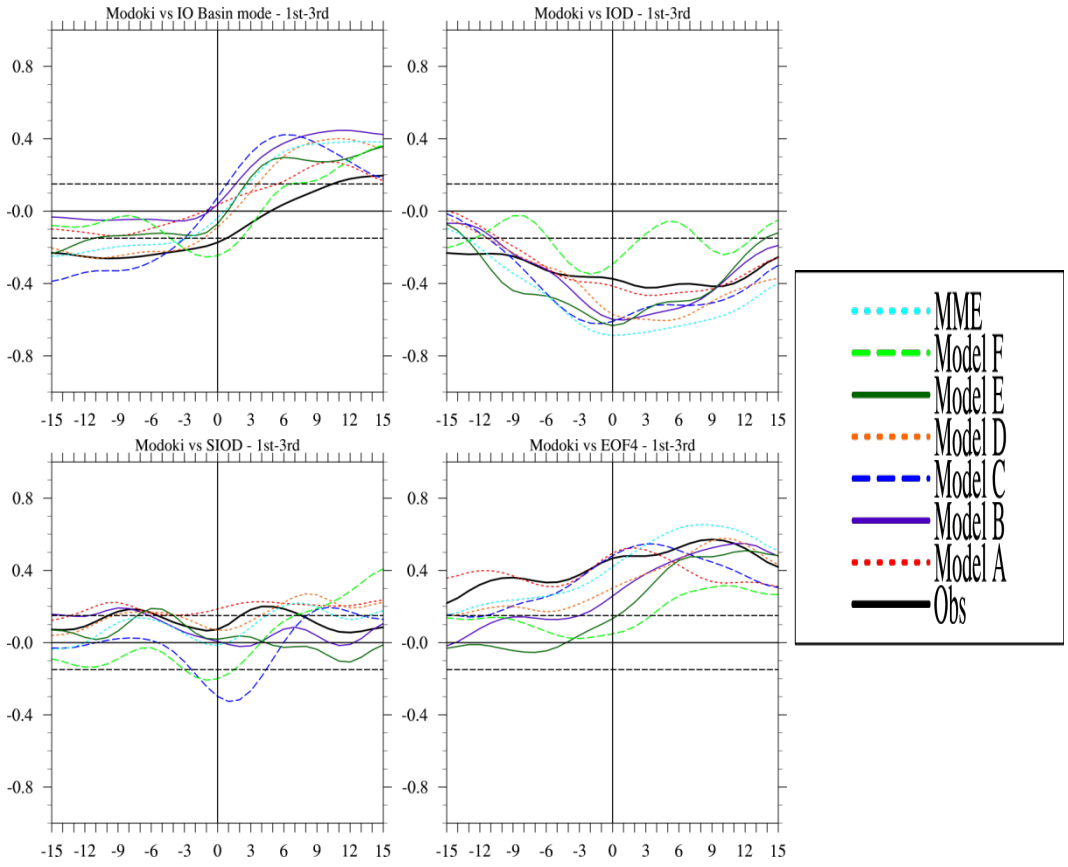

Fig. 5.6 Lead-lag correlation functions between the PjC2 of the tropical Pacific SSTA (Modoki) vs IOBM (top left), IOD (top right), SIOD (bottom left) and the PjC of the EOF4 of the Indian Ocean SSTA (bottom right). Dash lines indicate 95% significance level using R-test.

5.4 Summary of Chapter 5

It is found that the SST modes over the whole Indian Ocean are different from expectation during the studied period. The models tend to give different EOF patterns for the IO SST like the case for Pacific Ocean. Therefore, the projection coefficient method is employed again to investigate how the models behave in predicting IO SST modes according to the 4 observed IO SST modes.

It is found that the EOF1 to EOF4 are IOBM, an IOD-like pattern, Subtropical Indian Ocean Dipole (SIOD) and a newly discovered SST mode. The IOBM is well captured in observations and models. However, there are some mixings between the IOD-like pattern, SIOD and EOF4. Therefore, other tools are required to do further analysis using the other modes of IO SST.

Chapter 6

Discussion and Summary

There are two reasons to employ the six models of the Asia-Pacific Climate Center (APCC) hindcast (instead of using all models from the APCC). The first one is due to the limitation of data. Only a few sources of data can be obtained when doing the present study. Another reason is to emphases how the multi-model ensemble (MME) can enhance the predictability of a set of climate models. Previous studies suggest that the skill of the MME prediction is higher than the individual component of the ensemble members [Kug *et al*. (2008a); Wang *et al*. (2008)]. They also find that, by increasing the ensemble members, the skill is saturated when the number of ensemble member is larger than 5. Therefore, using the six models in the present study is a fair choice.

The three-month running mean method is applied to the monthly data (except the precipitation data) to smooth the data in the present study. The method, however, reduces the data signal in a certain degree. For the data which does not change rapidly, the degree of signal reduction is not large. However, the method is not suitable to precipitation data because monthly precipitation data is rather fluctuated. In order to smooth the precipitation data without losing clear signal, the 1-2-1

weighting filter method is employed to the data instead of the three-month running mean. Using the 1-2-1 filter makes signal of a target month in a certain time series sharper before averaging, which retains the original shape of the data. For example, applying the three-month running mean to the second element of a fluctuation time series -1, 1.5, -1 obtains a negative number -0.167. Nevertheless, if 1-2-1 filter is applied to the same time series, a positive number 0.25 is generated.

Kug *et al*. (2008a) compare four different methods to perform the MME. The first one is equal weighting MME (MME-EW; the method used in the present study) which calculates the average value over all included models with the same weighting. The second one is singular variable decomposition (SVD) weighting MME (MME-SVD). This method calculates the MME average using the weighting coefficients obtained from the SVD analysis (one can see Yun *et al*. [2003] for the detail to obtain those coefficients). The rest two MME methods calculate the MME based on a statistical model. The detail of these two methods will not be mentioned here, as it seems to deviate from the focus of the present study (however, one can see the detail of the methods in the studies of Kug *et al*. [2008a] and [2008b]; Yun *et al*. [2003]). Kug *et al*. (2008a), however, concludes that the MME-EW can defeat the rest of the sophisticated MME methods in most regions (especially the tropical Oceans). Indeed, the MME-SVD method experiences the over-fitting problem. That is, the weighting coefficients are not statistically stable, if the size of prediction sample (prediction period; in Kug *et al*. [2008b], the size is 20 years) is not large. This is also the reason why MME-EW is employed in the present study.

When doing the EOF analysis against the SST of the tropical Pacific and Indian Ocean, the CGCMs can generally reproduce the canonical ENSO patterns well. However, the predicted canonical ENSO patterns still have different features to each other. The similar case happens for the ENSO Modoki case and the Indian Ocean SST. Therefore, it is suggested projecting the modeled SSTA to the observed EOF pattern. Using the generated projection coefficients to replace the principle component to do further analysis is a good way to unify the ENSO patterns. Moreover, the method of the degree of mixings helps access the ability of the models to differentiate the two ENSO types. It is seen that the model who has low value of degree of mixings tend to give good differentiation of the pattern of ENSO.

It was found that the peak month of the canonical ENSO is in December. An obvious annual cycle can be observed for the canonical ENSO that it develops in summer, peaks in winter and decays in the following summer. Most of the models could capture the canonical ENSO cycle. However, there is a tendency that some models decay the canonical ENSO earlier for 1 to 2 months. For the ENSO Modoki, the peak month is in January. Unlike the canonical ENSO, ENSO Modoki tends to persist through the whole evolution. Nonetheless, some models cannot capture this feature well. This leads us to access how the prediction skill of the models can affect the EA climate predictions next step. Additionally, it is also suggested that the projection coefficient is a better representative to the ENSO Modoki.

The persistence of the two types of ENSO is revealed by the auto-correlation coefficients of the ENSO indices. The overall predictions of the APCC models for the canonical ENSO are better than that of the ENSO Modoki. However, a significant drop of persistence can be found 3-6 months after the peak of the two indices. This situation becomes more significant for longer leadtime or *El Niño* Modoki predictions. At the same time, it is found that almost all APCC models predict the amplitude of *El Niño* Modoki lower than the observations, especially for the boreal spring and

summer season (see Fig.3.22). Therefore, it is interpreted that spring persistence barrier of Modoki can be attributed to poor persistence in models, because the models cannot persist the *El Niño* Modoki well.

It is found that there is an anomalous wet (dry) condition over the south China coast during the decaying spring (summer) of the canonical ENSO. One of the reasons is that the Indian Ocean warming becomes increasingly important from the decaying spring to summer. Therefore, a westward shift of the dry band over the Tropical Pacific happens along the decay. For climate impacts of ENSO Modoki during its decaying phases, the low level anti-cyclone and dry band are mainly driven by the atmospheric forcing. Although the models give good predictions to the SSTA distribution, a good prediction of the position of the anti-cyclone could not be shown. This raises the attention to the factors other than the two types of ENSO over the tropical Pacific.

The climate over the southern China becomes regional during the decaying summer of ENSO Modoki. Moreover, the large-scale circulation does not have much effect on the climate there. Therefore, it is interpreted that the climate is driven by the other factors like monsoon during the period. It can be concluded that, for the decaying summer of the canonical ENSO, both the predictions of the El Niño SST and the predictions of mean circulation of EA are the crucial factors to the predictions of El Niño precipitation. However, for the decaying summer of the ENSO Modoki, the predictions of the ENSO Modoki SST seem not an important factor to affect the predictions of ENSO Modoki precipitation, while the predictions of the mean circulation is still crucial at this point.

For the Indian Ocean EOF analysis, it is found that the IOBM has great lag relationship to the canonical ENSO, while the new discovered EOF4 of the Indian Ocean SSTA has some degree of

relationship to the ENSO Modoki. The Subtropical Indian Ocean Dipole (SIOD) seems not to have too much relationship with the two flavors of ENSO.

Bibliography

Alves O, Wang G, Zhong A, Smith N, Tseitkin F, Warren G, Schiller A, Godfrey S, Meyers G (2003) 'POAMA: Bureau of Meteorology operational coupled model seasonal forecast system'. Proc. National Drought Forum, Brisbane, April 2003, pp 49-56. Available from DPI Publications, Department of Primary Industries, GPO Box 46, Brisbane, Qld 4001, Australia

Ashok K, Behera SK, Rao SA, Weng H and Yamagata T (2007) El Niño Modoki and its possible teleconnection. J Geophys Res, 112: C11007, doi: 10.1029/2006JC003798.

Behera SK, Krishnan S and Yamagata T (1999) Unusual Ocean-Atmosphere conditions in the tropica Indian Ocean during 1994, Geophy Res Lett, 26, 3001-3004.

Chan JCL and Zhou W (2005) PDO, ENSO and the early summer monsoon rainfall over South China. Geophysical Research Letters, 32, L08810, DOI: 10.1029/2004GL022015.

Chang C, Zhang Y and Li T. (2000) Interannual and interdecadal variations of the East Asian summer monsoon and tropical Pacific SSTs. Part I: roles of the subtropical ridge. Journal of Climate, 13, 4310–4325.

Chou C, Huang LF, Tu JY, Tseng L and Hsueh YC (2009) El Niño impacts on precipitation in the western Pacific East Asian sector. J Clim, 22, 2039-2057.

Deser C, Alexander MA, Xie SP, and Phillips AS (2010) Seasurface temperature variability: Patterns and mechanisms. Ann Rev Marine Sci, 2, 115–143, doi:10.1146/annurev-marine-120408-151453.

Du Y, Xie SP, Huang G and Hu K (2009) Role of air–sea interaction in the long persistence of *El Niño*–induced North Indian Ocean warming. J. Climate, 22, 2023–2038.

Feng J, Chen W, Tam CY and Zhou W (2010) Different Impacts of El Niño and El Niño Modoki on China Rainfall in the Decaying Phases. Int J Climatol, doi: 10.1002/joc.2217

Feng J and Chen W (2013) Influence of the IOD on the relationship between *El Niño* Modoki and the East Asian-western North Pacific summer monsoon. International Journal of Climatology, 34, 1729-1736.

Feng J and Li J (2011) Influence of El Niño Modoki on spring rainfall over south China. J of geophy res., 116, doi:101029/2010JD015160.

Fu X and Wang B (2004) The boreal-summer intraseasonal oscillations simulated in a hybrid coupled atmosphere-ocean model. Mon Wea Rev, 1322628-2649. DOI: 10.1175/MWR2811.1.

Huang R, Chen W, Yan B and Zhang R (2004) Recent advances in studies of the interaction between the East Asian winter and summer monsoon and ENSO cycle. Advances in Atmospheric Sciences, 6, 21-32.

Iizuka S, Matsuura T and Yamagata T (2000) The Indian Ocean SST dipole simulated in a coupled general circulation model. Geophy Res Lett, 0, 0-0.

Jeong HY, Ashok K, Song BG, Min YM (2008) Experimental 6-month hindcast and forecast simulation using CCSM3, APCC 2008 Tech Rep, APEC Clim Cent, Pusan, South Korea

Ji L, Sun S and Arpe K (1997) Model study on the interannual variability of Asian winter monsoon and its influence. Adv. Atmos. Sci., 14, 1-22.

Jin FF (1997) An equatorial ocean recharge paradigm for ENSO. Part I: conceptual model. AMS, 54, 811-829.

Joong BA and Hwang TJ (2005) A Study of Predictability of CME/PNU CGCM for East Asia Winter Temperature. Asia Pac J Atmo Sci, 41, 943 – 954

Kalnay E, Kanamitsu M, Kistler R, Collins W, Deaven D, Gandin L, Iredell M, Saha S, White G, Woollen J, Zhu Y, Chelliah M, Ebisuzaki W, Higgins W, Janowiak J, Mo KC, Ropelewski C, Wang J, Leetmaa A, Reynolds R, Jenne R, and Joseph D (1996) The NCEP/NCAR 40-Year Reanalysis Project. J Clim, 77, 437-471

Kang I and Jeong Y (1996) Association of interannual variations of temperature and precipitation and precipitation in Seoul with principal modes of Pacific SST. J Korean Meteor Soc, 32, 339-345.

Kao HY and Yu JY (2009) Contrasting Eastern-Pacific and Central-Pacific types of ENSO. J Clim, 22, 615 – 632.

Kim HM, Webster PJ and Curry JA (2012) Evaluation of short-term climate change prediction in multi-model CMIP5 decadal hindcasts, Geophysical Research Letters, 39, L10701, doi:10.1029/2012GL051644.

Kirtman BP, Shukla J, Balmanseda M, Graham N, Penland C, Xue Y and Zebiak S (2002) Current status of ENSO forecast skill: A report to the Climate Variability and Predictability (CLIVAR) Numerical Experimentation Group (NEG), CLIVAR Working Group on Seasonal to Interannual Prediction, Clim. Variability and Predictability, Southampton Oceanogr. Cent., Southampton, UK.

Klein S and Lau NC (1999) Remote Sea Surface Temperature Variations during ENSO: Evidence for a Tropical Atmosperic Bridge. J Clim, 12, 917-932

Klein S, Soden BJ and Lau NC (1999) Remote sea surface temperature variations during ENSO: Evidence for a Tropical Atmospheric Bridge. J Clim, 12, 917-932.

Kug JS, Lee T, An SI, Kang IS, Luo JJ, Masson S and Yamagata T (2006) Role of the ENSO-Indian Ocean coupling on ENSO variability in a coupled GCM. Geophy let, 33, L09710, doi:10.1029/2005GL024916.

Kug JS, Kang IS and Choi DH (2007) Seasonal Climate Predictability with Tier-one and Tier-two prediction system. Clim Dyn, Doi: 10.1007/s00382-007-0264-7

Kug JS, Lee JY, Kang IS, Wang B and Park CK (2008a) Optimal Multi-model Ensemble Method in Seasonal Climate Prediction, Asia-Pacific Journal of Atmo. Sci., 44, 3, 2008, p259-267.

Kug JS, Kang IS and Lee JY (2008b) Systematic bias correction of dynamical seasonal prediction using a step-wise pattern projection method, Mon. Wea. Rev., in press.

Kug JS, Jin FF and An SI (2009) Two types of El Niño events: cold tongue El Niño and warm pool El Niño. J Clim, 22, 1499-1515.

Kug JS and Ham YG (2011) Are there two types of La Nina? Geophy Res Lett, 38, L16704, doi:10.1029/2011GL048237.

Larkin NK and Harrison DE (2005) Global seasonal temperature and precipitation anomalies during El Niño autumn and winter. Geophys Res Lett, 32, L16705, doi: 10.1029/2005GL022860.

Lau KM (1992) The East Asian summer monsoon rainfall variability and climate teleconnection. J. Meteor. Soc. Japan, 70, 211-241.

Lau KM and Li M (1984) The monsoon of East Asia and its global association-A survey. Bull Amer. Meteor. Soc., 65, 114-125.

Lau KM and Yang S (1996) The Asian monsoon and predictability of the tropical ocean-atmosphere system. Quarterly Journal of Royal Meteorological Society, 122, 945-957.

Lau NC and Nath MJ (1996) The Role of the "Atmospheric Bridge" in Linking Tropical Pacific ENSO Events to Extratropical SST Anomalies, Journal of Climate, 9, 2036-2057.

Lau NC and Nath MJ (2006) ENSO modulation of the interannual and intraseasonal variability of the East Asian monsoon-A model study. J Clim, 19, 4508-4530.

Lin JL (2007) The Double-ITCZ problem in IPCC AR4 coupled GCMs: Ocean-Atmosphere Feedback Analysis. AMS, 20, 4497-4525.

MaPhaden MJ (2003) Tropical Pacific ocean heat content variations and ENSO persistence barriers. Geophysical Research Letters, 30, 1480, doi: 10.1029/2003GL016872.

Mo KC (2010) Interdecadal Modulation of the Impact of ENSO on Precipitation and Temperature over the United States, J Clim, 23, 3639-3656. doi: 01175/2010JCLI3553.1.

Murtugudde R, McCreary JP and Busalacchi AJ (2000) Oceanic processes associated with anomalous events in the Indian Ocean with relevance to 1997-1998. J Clim, 105, 3295-3306.

Nicholls N, Lavery B, Frederiksen C, Drosdowsky W and Torok S (1996) Recent changes in elationships between the El Niño–Southern Oscillation and Australian rainfall and temperature. Geophys. Res. Lett., 23, 3357–3360.

Philander G (1990) El Niño, La Nina and the Southern Oscillation. Academic Press, Page 293

Power S, Casey T, Folland C, Colman A and Mehta V (1999) Interdecadal modulation of the impact of ENSO on Australia. Clim Dyn, 15, 319-324.

Rayner NA, Parker DE, Horton EB, Folland CK, Alenxander LV, Rowell DP, Kent EC, Kaplan A (2003) Global analyses of sea surface temperature, sea ice, and night marine air temperature since the latenineteenth century. J Geophys Res, 108, 4407–4443

Rasmusson, Wang X, and Ropelewski CF, (1990) The biennial component of ENSO variability. J Marine Syst, 1, 71–96

Roeckner E, and Coauthors (2003) Atmospheric general circulation model ECHAM5: Part I. Max-Planck-Institut fur Meteorlogie Rep 349, 140 pp

Ross CJ (2000) El Niño: The Weather Phenomenon that Changed the World, London: Hodder & Stoughton.

Saji NH, Goswami BN, Vinayachandran PN and Yamagata T (1999) A dipole mode in the tropical Indian Ocean. Nature, 401, 360-363.

Saji NH, Xie SP and Yamagata T (2006) Tropical Indian Ocean variability in the IPCC 20th-century climate simulations. J Climate, 19, 4397–4417.

Saha S, Nadiga C, Thiaw J, Wang W, Wang Q, Zhang HM, van den Dool HL, Pan S, Moorthi D, Behringer D, Stokes G, White S, Lord W, Ebisuzaki P, Xie PP (2006) The NCEP Climate Forecast System. J Clim, 19, 3483 – 3517

Sohn SJ, Tam CY and Jeong HI (2016) How do the strength and type of ENSO affect SST predictability in coupled models. Sci. Rep. 6, 33790; doi: 10.1038/srep33790.

Suppiah R (2004) Trends in the Southern Oscillation phenome-non and Australian rainfall and changes in their relationship. Int. J. Climatol., 24, 269–290.

Tao S and Zhang Q (1998) Response of the East Asian summer monsoon to ENSO events (in Chinese). Sci. Atmos. Sinica, 22, 399-407.

Taschetto AS and England MH (2008) An analysis of late 20th Century trends in Australian rainfall. Int. J. Climatol., 29, 791–807, doi:10.1002/joc.1736.

Tippett MK, Barnston AG and Li S (2012) Performance of Recent Multimodel ENSO Forecasts. AMS, 51, 637-654.

Tomita T and Yasunari T (1996) Role of the northeast winter monsoon on the biennial oscillation of the ENSO/monsoon system. J. Meteor Soc. Japan. 41, 399-413.

Vinayachandran PN, Saji NH and Yamagata T (1999) Response of the equatorial Indian Ocean to an unusual wind event during 1994. Geophy Res Lett, 26, 1613-1615.

Wang B, Lee JY, Kang IS, Shukla J, Park CK, Kumar A, Schemm J, Cocke S, Kug JS, Luo JJ, Zhou T, Wang B, Fu X, Yun WT, Alves O, Jin EK, Kinter J, Kirtman B, Krishnamurti T, Lau NC, Lau W, Liu P, Pegion P, Rosati T, Schubert S, Stern W, Suarez M and Yamagata T (2008) Advance and prospectus of seasonal prediction: assessment of the APCC/CliPAS

14-model ensemble retrospective seasonal prediction (1980-2004), Clim. Dyn., doi 10.1007/s00382-008-0460-0.

Wang B, Wu R and Fu X (1999a) Pacific-East Asian Teleconnection: How does ENSO affect East Asian Climate? AMS, 13, 1517-1536.

Wang B, Wu R and Lukas R (1999b) Roles of the western North Pacific wind variation in the thermocline adjustment and ENSO phase transition. J Meteor Soc Japan, 77, 1-16.

Wang B, Wu R and Fu X (2000) Pacific-East Asian Teleconnection: How does ENSO affect East Asian Climate? J Clim, 13, 1517-1536

Wang C (2001) A unified oscillator model for the *El Niño*-Southern Oscillation. J Climate, 14, 98-115.

Wang C, Deser C, Yu JY, DiNezio P and Clement A (2016) *El Niño* and Southern Oscillation (ENSO): A review. Springer, DOI 10.1007/978-94-017-7499-4_4.

Watanabe M and Jin FF (2002) Role of Indian Ocean warming in the development of Philippine Sea anticyclone during ENSO. Geo phy let, 29, 116-119.

Weng H, Ashok K, Behera SK, Rao SA and Yamagata T (2007) Impacts of recent El Niño Modoki on dry/wet conditions in the Pacific rim during boreal summer. Climate Dyn., 29, 113–129.

Weng H, Behera SK and Yamagata T (2009) Anomalous winter climate conditions in the Pacific rim during boreal summer. Clim Dyn, 29, 113-129.

Webster PJ and Yang S (1992) Monsoon and ENSO: Selectively interactive systems. Quarterly Journal of Royal Meteorology Society, 118, 877-926.

Webster PJ, Moore AM, Loschnigg JP and Leben RR (1999) Coupled oceanic-atmospheric dynamics in the Indian Ocean during 1997-98, Nature, 401, 356-360.

Wu R, Kirtman BP and Dool HVD (2009) An Analysis of ENSO Prediction Skill in the CFS Retrospective Forecasts, AMS, 22, 1801-1818.

Wu R, Hu ZZ and Kirtman BP (2003) Evolution of ENSO-related rainfall anomalies in East Asia. J Clim, 16, 3742-3758.

Xie SP, and Arkin PA (1997) Global Precipitation: A 17-year monthly analysis based on gauge observations, satellite estimates, and numerical model outputs. J Clim, 78, 2539 – 2558

Xie SP, Annamalai H, Schott FA and McCreary JP (2002) Structure and mechanisms of south Indian Ocean climate variability. J Clim, 15, 864-878.

Xie SP, Hu K, Hafner J, Tokinaga H, Du Y, Huang G and Sampe T (2009) Indian Ocean Capacitor Effect on Indo–Western Pacific Climate during the summer following El Niño. J Clim, 22, 730 – 747.

Yang J, Liu Q, Xie SP, Liu Z, and Wu L (2007) Impact of the Indian Ocean SST basin mode on the Asian summer monsoon. Geophys Res Lett, 34, L02708, doi:10.1029/2006GL028571

Yasunari T (1991) The monsoon year-A new concept of the climatic year in the Tropics. Bull Amer Meteor Soc, 78, 2539-2588.

Yu L and Rienecker MM (1999) Mechanism for the Indian Ocean warming during the 1997-98 El Niño. Geophy Res Lett, 26, 735-738.

Yu JY and Kao HY (2007) Decadal changes of ENSO persistence barrier in SST and ocean heat content indices: 1958-2001. J Geophys Res, 112, D13106, doi:10.1029/2006JD007654.

Yu JY and Kim ST (2010) Identification of Central-Pacific and Eastern-Pacific types of ENSO in CMIP3 models, Geophy Res Lett, 37, L15705, doi:10.1029/2010GL044082.

Yun WT, Stefanova L and Krishnamurti TN (2003) Improvement of the superensemble technique for seasonal forecasts. J Climate, 16, 3834-3840.

Zhang R, Sumi A and Kimoto M (1996) Impact of El Niño on the East Asian monsoon: A diagnostic study of the 86/87 and 91/92 events. J Meteor Soc Japan, 74, 49-62.

Zhou W and Chan JCL (2007) ENSO and the South China Sea summer monsoon onset. International Journal of Climatology, 27, 157–167.

Zhou LT, Tam CY, Zhou W and Chan JCL (2009) Influence of South China Sea SST and the ENSO on winter rainfall over South China, Advances in Atmospheric Sciences, 27, 832–844, DOI: 10.1007/s00376-009-9102-7.